

CONSTRAINING MANTLE PROPERTIES BY INVERTING FOR OBSERVATIONS OF DYANAMIC TOPOGRAPHY

A DISSERTATION

Submitted in partial fulfillment of the requirements
of the degree of

Integrated Master of Technology

in

Geophysical Technology

by

Prahlada Varada Mittal

Enrol. No. 20411023

Supervisors:

Prof. Pitambar Pati

and

Dr. Sia Ghelichkhan



Department of Earth Sciences
INDIAN INSTITUTE OF TECHNOLOGY ROORKEE
2025

© INDIAN INSTITUTE OF TECHNOLOGY ROORKEE, 2025

ALL RIGHTS RESERVED

Dedicated to my beloved parents:

Prof. Ankush Mittal

Adv. Garima Mittal

Candidate's Declaration

I hereby declare that the work presented in this dissertation, titled **Constraining Mantle Properties by Inverting for Observations of Dynamic Topography**, submitted in partial fulfilment of the requirements for the award of the degree of Integrated Master of Technology in Geophysical Technology, in the Department of Earth Sciences, Indian Institute of Technology Roorkee, has been carried out by me during the period May 2024 to May 2025 under the supervision of Dr. Sia Ghelichkhan (Australian National University) and Prof. Pitambar Pati (IIT Roorkee). This work is the outcome of my own research and effort. Wherever the ideas or work of others have been used, they have been properly acknowledged. I have followed the principles of academic honesty and integrity throughout the preparation of this thesis. No part of it has been copied or fabricated, and it has not been submitted for any other degree or diploma at any institution.

Date: 19/05/2025



Prahлада Varada Mittal

Certificate by Supervisors

This is to certify that the above statement made by the candidate is correct to the best of our knowledge. The work reported in this dissertation was carried out under our joint supervision.



Prof. Pitambar Pati

Internal Supervisor

Professor

Department of Earth Sciences

Indian Institute of Technology Roorkee

Roorkee, India



Dr. Sia Ghelichkhan

External Supervisor

Lecturer

Research School of Earth Sciences

Australian National University

Canberra, Australia

Abstract

Keywords: Adjoint-based Inversion, Mantle Rheology, Dynamic Topography, Sensitivity Analysis, Activation Energy, Mantle Convection, G-ADOPT, Surface Velocity, Finite Element

Dynamic topography, driven by stresses from mantle convection, offers a valuable constraint on Earth's internal structure. However, its use in constraining mantle rheology is hindered by uncertainties in material parameters, inversion non-uniqueness, and sensitivity trade-offs with other observables. This thesis introduces a novel, high-resolution adjoint-based inversion framework that jointly exploits dynamic topography and surface velocity to recover spatial variations in viscosity and activation energy under a fully non-linear visco-plastic rheology. Prior studies have typically relied on forward models or simplified radial profiles, without systematically assessing dynamic topography sensitivity or performing joint inversion with realistic rheologies. Our primary contribution is the development of an automated inversion workflow using the G-ADOPT platform in a 2D annular domain approximating spherical shell curvature. The model solves coupled incompressible Stokes and thermal energy equations with temperature, depth, and stress-dependent viscosity including yielding. Sensitivities are computed via the discrete adjoint method, enabling scalable optimization in log-viscosity space. A key novelty lies in performing a series of controlled modeling frameworks, spanning inversion for viscosity, temperature, and depth and temperature dependent activation energy, to systematically evaluate the sensitivity of surface observables and the recoverability of mantle properties. The results demonstrate that dynamic topography is particularly sensitive to long-wavelength, deep-seated flow, while surface velocity offers stronger constraints on shallow and high-frequency variations. We show that dynamic topography alone does not uniquely constrain rheology, but when jointly inverted with velocity data and suitable regularization, it enables recovery of complex spatial variations in mantle properties. This work is one of the first implementations of joint adjoint-based inversion under a fully non-linear rheology with both radial and lateral heterogeneity, and provides a foundation for future studies linking mantle structure to surface processes such as glacial isostatic adjustment and basin evolution.

Acknowledgments

I would like to sincerely thank Dr. Sia Ghelichkhan and Prof. Rhodri Davies from the Research School of Earth Sciences, Australian National University, for their guidance and continuous support throughout my Master's research. I am also deeply grateful to Dr. William Scott, Dr. Mark Hoggard, and everyone in the G-ADOPT group at ANU for being so welcoming during my time there. Their patience, encouragement, and willingness to help whenever I had questions made a big difference. Working with them has been one of the highlights of this journey, and I truly appreciate the trust they placed in me.

At IIT Roorkee, I am especially grateful to Prof. Pitambar Pati for his guidance and steady support as my supervisor. As my thesis supervisor and coordinator, he has not only helped in my academic progress but also mentored me through personal challenges with empathy and understanding, for which I am deeply grateful. I extend my sincere thanks to Prof. Sandeep Singh, Head of the Department of Earth Sciences, IIT Roorkee, and the entire faculty for their constant encouragement, support, and foundational teachings that have empowered me with the confidence and knowledge to move forward in my career. I am especially thankful to Prof. Sagarika Mukhopadhyay, Chairperson of Dissertations, and the respected committee members for their motivation and constructive feedback. I am also grateful to Prof. Anand Joshi, former Head of Department, and Prof. R. Krishnamurti, former DAPC Chairman, for their support during my research exchange, and to Prof. Ravi Sharma for his valuable guidance during the early phase of this work.

I'm also thankful to the technical staff at the ESD, IIT Roorkee, and RSES, ANU. Their help and support at different stages of this work made things a lot smoother and are truly appreciated. Being part of IIT Roorkee has been a true privilege, and I'm grateful for all the opportunities it gave me. I especially thank the IR Cells at IIT Roorkee and the Australian National University for their support through the Future Research Talent (FRT) program. I would like to particularly acknowledge Jay Poria from the FRT team for his kind assistance and co-ordination throughout the exchange process. The FRT award I received in 2024 enabled me to take part in this exchange, which made my research visit possible and helped me grow both academically and personally.

I am thankful to my friends, especially Paritosh, Shivika, Akshat, Nikhil, Niranjana, Mridul, Kaustubh, and all others who were there through it all. For the laughs, the trips, the late night conversations, the honest advice, and the quiet support when I needed it most. This

journey would not have been the same without them.

I'm deeply thankful to my parents for always being there for me through every high and low. My father, Dr. Ankush Mittal, whose teachings, encouragement, corrections, and steady presence have been the guiding light, and my mother, Mrs. Garima Mittal, whose love, support, and motivation have been my constant strength. I truly couldn't have done this without them.

Above all, I am extremely grateful to Lord Krishna for the motivation, strength, and clarity bestowed upon me to see this work through to completion.

A handwritten signature in black ink, appearing to read "Ankush Mittal".

Table of Contents

Abstract	i
List of Tables	ix
List of Figures	x
List of Listings	xi
List of Abbreviations	xiii
List of Symbols	xiv
1 Introduction	1
1.1 Background and Motivation	1
1.2 Dynamic Topography and Its Significance	2
1.2.1 Early Evidence and Observational Examples	3
1.2.2 Significance and Importance of Sensitivity Analysis	4
1.2.3 Surface Processes Affected by Dynamic Topography	5
1.2.4 Calculation of Dynamic Topography	7
1.3 Literature Review	8
1.3.1 Research Gaps	11
1.4 Research Objectives	12
1.5 Methodology Overview	13
1.6 Thesis Organization	14
2 Theoretical and Computational Framework for Forward Modeling	17
2.1 Governing Equations of Mantle flow	17

2.2	Rheological Model	20
2.3	Finite Element Method	22
2.4	Solution Procedure	24
2.4.1	Finite Element Discretization	24
2.4.2	Boundary Conditions	26
2.4.3	Solution process for temperature, velocity and pressure	27
2.5	Calculation of Dynamic Topography and Surface Velocity	29
3	Adjoint-Based Geodynamic Inversion Framework	31
3.1	Calculation of Objective functional	32
3.1.1	Regularization Terms	33
3.1.2	Normalization Terms	35
3.1.3	Defining a reduced functional	35
3.2	Adjoint-Based Gradient Calculation	36
3.2.1	Gradient Calculation	37
3.2.2	Continuous vs Discrete Adjoint	38
3.2.3	Sensitivity Kernel	40
3.3	Gradient Verification	41
3.4	Gradient-based Optimization	42
3.4.1	Lin–Moré Optimization Algorithm	43
4	Numerical Implementation and Results: Inversion Using Field-Based Controls	45
4.1	Software Framework	46
4.2	Model Configuration 1: Inversion Using Viscosity as the Control Parameter . .	48
4.2.1	Synthetic Data Generation	48
4.2.2	Forward Model and Initial Misfit Calculation	52
4.2.3	Calculation and Verification of Adjoint Gradients	54
4.2.4	Optimization and Inversion	57
4.2.5	Results	58
4.3	Model Configuration 2: Inversion Using Temperature as the Control Parameter	61
4.3.1	Forward Model and Gradient Calculation	61
4.3.2	Optimization and Inversion	63
4.3.3	Results	64

5 Numerical Implementation and Results: Inversion of Rheological Parameters	69
5.1 Model Configuration 3: Inversion Using Activation Energy as the Control Parameter	69
5.1.1 Forward Model and Gradient Calculation	70
5.1.2 Optimization and Inversion	73
5.1.3 Results	75
5.2 Model Configuration 4: Inversion Using Activation Energy with Depth-Dependent Rheology	77
5.2.1 Synthetic Data Generation	78
5.2.2 Forward Model and Gradient Calculation	81
5.2.3 Optimization and Inversion	84
5.2.4 Results	85
5.3 Model Configuration 5: Inversion Using Activation Energy with Fully Complex Mantle Rheology	88
5.3.1 Synthetic Data Generation	89
5.3.2 Forward Model and Gradient Calculation	90
5.3.3 Optimization and Inversion	93
5.3.4 Results	95
6 Conclusion and Future Work	99
6.1 Summary	99
6.2 Contributions and Key Findings	100
6.3 Limitations of the Study	103
6.4 Future Directions	104
Code Availability	105
References	109

List of Tables

2.1	List of symbols used in Eqs. (2.1)–(2.7).	19
2.2	Definition of symbols used in Eqs. (2.8)–(2.9)	21
3.1	Symbols used in the misfit and objective functional calculation. (Eqs (3.1)-(3.7))	34
3.2	List of Symbols used in the adjoint-based gradient calculation section (Eqs (3.9)-(3.24).	37
5.1	Initial and observed values of activation energy and corresponding gradient sensitivities of the objective function components.	72
5.2	Observed and initial guess values of activation energy, along with the initial gradients of the misfit terms with respect to each control parameter.	83
5.3	Initial guesses, observed values, and gradients of the dynamic topography and surface velocity misfit terms with respect to each activation energy parameter. .	93
6.1	Summary of model configurations, assumptions, and main findings.	101

List of Figures

1.1	Conceptual illustration of dynamic topography	3
1.2	Surface processes influenced by dynamic topography	6
1.3	Estimation strategies and inverse geodynamics	10
1.4	Schematic workflow of the framework	13
2.1	Annular FEM mesh in 2D model	23
3.1	Flowchart describing the iterative optimization procedure for inversion.	43
4.1	Core software libraries used for this study.	46
4.2	Reference temperature evolution for inversion	50
4.3	Viscosity evolution to a steady state	50
4.4	Observed temperature and viscosity fields	51
4.5	Observed dynamic topography and surface velocity (Model Configuration 1) . .	52
4.6	Initial viscosity guess and misfit (Model Configuration 1)	52
4.7	Initial dynamic topography and velocity misfits (Model Configuration 1) . . .	55
4.8	Gradients of objective terms with respect to viscosity	55
4.9	Taylor test for viscosity gradient verification	56
4.10	Evolution of misfits and objective functional	58
4.11	Viscosity reconstruction during optimization	59
4.12	Final fit of dynamic topography and velocity (Model Configuration 1) . . .	59
4.13	Final reconstructed viscosity field after inversion.	60
4.14	Initial temperature and viscosity fields (Model Configuration 2)	62
4.15	Initial misfit in topography and velocity (Model Configuration 2)	62
4.16	Gradients of misfits with respect to temperature	63
4.17	Inversion metrics for temperature control	65

4.18	Final fit using temperature as control	66
4.19	Reconstructed fields from temperature inversion	66
5.1	Observed vs. initial guessed fields for $E_a = 2.0$	70
5.2	Initial misfit fields for guessed activation energy	72
5.3	Taylor test for activation energy inversion (Model Configuration 3)	73
5.4	Inversion metrics for different α_u values	74
5.5	Activation energy reconstruction vs. iterations (Model Configuration 3)	75
5.6	Final fit of topography and velocity for varying α_u	76
5.7	Reconstructed viscosity for $\alpha_u = 1.0$	77
5.8	Viscosity components for depth-dependent rheology	80
5.9	Observed temperature and viscosity fields	80
5.10	Initial guess and viscosity misfit for layered E_a	82
5.11	Initial misfit fields for layered E_a guess	82
5.12	Taylor test for layered E_a inversion	83
5.13	Convergence metrics for layered E_a inversion	85
5.14	Activation energy evolution (Model Configuration 4)	86
5.15	Final fit of observables for layered E_a inversion	87
5.16	Reconstructed viscosity for layered E_a case	87
5.17	Observed temperature and viscosity for complex model	90
5.18	Viscosity components in the fully complex model	91
5.19	Initial guess vs. observed viscosity and misfit (Model Configuration 5)	92
5.20	Initial misfits in topography and velocity (Model Configuration 5)	92
5.21	Inversion metrics for different α_u values (Model Configuration 5)	94
5.22	Activation energy inversion history (6 parameters)	95
5.23	Final fit of topography and velocity (Model Configuration 5)	96
5.24	Reconstructed viscosity in fully complex model	97

List of Listings

1	Synthetic data generation using a time-dependent mantle simulation.	49
2	Inversion setup and gradient check (Model Configuration 1)	53
3	Bounded non-linear inversion using Lin-More optimizer	57
4	Bounded nonlinear optimization with temperature control	64
5	Inversion setup using activation energy control	71
6	Bounded non-linear optimization with activation energy control	73
7	Synthetic data generation with layered E_a in Gadopt	79
8	Control and gradient setup for layered E_a inversion	81
9	Bounded nonlinear optimization for layered E_a inversion	84
10	Selected implementation lines for computing the synthetic viscosity field with full rheology (Model Configuration 5).	89
11	Selected lines from the updated Gadopt script showing the initial guess and control setup.	91
12	Optimization setup with six E_a parameters	93

List of Abbreviations

CG	Continuous Galerkin
CMB	Core–Mantle Boundary
DG	Discontinuous Galerkin
DT	Dynamic Topography
FEM	Finite Element Method
G-ADOPT	Geoscientific ADjoint Optimisation PlaTform
GIA	Glacial Isostatic Adjustment
GIS	Geographic Information System
GPS	Global Positioning System
IC	Initial Condition
L2 norm	Second-order (Euclidean) norm
PDE	Partial Differential Equation
Paraview	Parallel Visualization Application
Q1	Bilinear Lagrange Element
Q2	Bi-quadratic Lagrange Element
Q2Q1	Taylor–Hood Element (velocity–pressure pair)
RMS	Root Mean Square
ROL	Rapid Optimization Library
RT	Residual Topography
UFL	Unified Form Language
VTK	Visualization Toolkit

List of Symbols

u	Velocity vector (m/s)
p	Dynamic pressure (Pa)
T	Temperature field (K)
μ	Viscosity (Pa·s)
μ_{avg}	Average viscosity field
$\dot{\varepsilon}$	Strain-rate tensor (s^{-1})
ρ_0	Reference density (kg/m ³)
g	Gravitational acceleration (m/s ²)
α	Thermal expansion coefficient (K ⁻¹)
κ	Thermal diffusivity (m ² /s)
ΔT	Temperature contrast across domain (K)
L	Characteristic length scale (m)
Ra	Rayleigh number
z	Depth (m)
Ω	Computational domain
Γ_t	Top boundary of domain
μ_{lin}	Linear (temperature- and depth-dependent) viscosity component
μ_{plast}	Plastic viscosity component
μ^*	Limiting effective viscosity
σ_y	Yield stress (Pa)
$\Delta\mu_T$	Viscosity contrast due to temperature

$\Delta\mu_z$	Viscosity contrast due to depth
E_{aT}	Activation energy (temperature-dependent)
E_{az}	Activation energy (depth-dependent)
h_{res}	Residual topography (m)
h_{obs}	Observed surface elevation or bathymetry (m)
h_{iso}	Isostatic topography (m)
h_{dyn}	Dynamic topography (m)
σ_{zz}	Vertical normal stress at surface (Pa)
σ_{nn}	Normal stress in direction n (Pa)
u_{surf}	Surface velocity (m/s)
u_{obs}	Observed surface velocity (m/s)
Δt	Time step (s)
\hat{J}	Reduced objective functional
$\nabla \hat{J}$	Gradient of the reduced functional
J	Full objective functional
F	Forward model (PDE system)
λ	Adjoint variable
$K(x)$	Sensitivity kernel at location x
α_{dt}	Weight for DT misfit term
α_u	Weight for velocity misfit term
α_s	Weight for smoothing regularization
α_d	Weight for damping regularization
N_{dt}, N_u, N_s, N_d	Normalization constants for misfit and regularization terms
θ	Time-stepping parameter in Crank–Nicolson method
ϕ_i	Finite element basis functions
$z = z_s$	Surface depth level

Chapter 1

Introduction

1.1 Background and Motivation

Understanding the Earth's internal dynamics remains a fundamental challenge in geophysics, primarily due to the mantle's inaccessibility. Mantle convection acts as the driving force behind the Earth's dynamic behavior (Davies and Richards, 1992; Ricard, 2007; Jarvis and Peltier, 1982). It plays an important role in regulating the planet's thermal and chemical evolution (Coltice et al., 2017), and is the key mechanism that governs surface tectonics and geological processes. Plate movements, surface deformation, topography, and gravity anomalies are measured directly at the Earth's surface, while additional constraints on internal structure are inferred from seismic imaging (Romanowicz, 2008; Chu et al., 2012). These datasets have been effective in improving our understanding of present-day plate tectonics and mantle convection processes (Worthen et al., 2014). As mantle flow interacts with the overlying lithosphere, it transports heat and fluids that can play a key role in forming and concentrating ore deposits (Pirajno, 2004; Robb, 2020). It also causes vertical movements of the Earth's surface, a phenomenon known as dynamic topography (Hager and Richards, 1989; Davies et al., 2019). Among the various indirect methods used to probe mantle rheology, dynamic topography has become a particularly useful observable (Davies et al., 2023; Hoggard et al., 2016). It provides a link between measurable surface signals and deeper mantle processes, helping to constrain internal structure and the forces driving mantle flow (Moucha et al., 2008; Gurnis, 1993; Colli et al., 2016).

Constraining mantle properties such as viscosity, activation energy, and density is crucial for interpreting a wide range of Earth system processes, including long-term sea-level change, sedimentary basin development, and glacial isostatic adjustment (GIA) (Peltier and Jiang, 1997; Kaufmann and Lambeck, 2002). GIA, in particular, is highly sensitive to the mantle's rheological structure, which governs both the spatial and temporal evolution of post-glacial rebound

(Steffen and Kaufmann, 2005; Mitrovica and Forte, 2004; Davies et al., 2023). Although forward geodynamic simulations have improved, they cannot uniquely determine mantle parameters due to the inherent initial condition problem (Müller et al., 2018; Colli et al., 2015). Since the present-day mantle state reflects a complex geological history, forward models alone cannot fully reconstruct that evolution (Davies and Davies, 2009; Bunge et al., 2003; Stadler et al., 2010). The challenge is further compounded by ambiguities in translating seismic velocities to temperature and composition (Worthen et al., 2014), and by oversimplified viscosity models, such as purely radial profiles that neglect important lateral variations (Steffen and Kaufmann, 2005; Kaufmann and Lambeck, 2002; Lau et al., 2018). Adjoint-based inverse methods provide a powerful alternative by allowing efficient computation of sensitivities with respect to model parameters (Bunge et al., 2003; Ismail-Zadeh et al., 2004). These approaches enable present-day surface data to be used for adjusting internal properties in a physically consistent framework (Reuber et al., 2020). Open-source frameworks such as G-ADOPT (Ghelichkhan et al., 2024) now make it computationally feasible to implement such workflows in realistic geometries using finite element methods. This creates new opportunities to test how well surface observables, such as dynamic topography and surface velocity can jointly constrain the internal structure of the mantle.

The goal of this study is to build on these advances and investigate how surface signals can be used to infer spatial variations in mantle viscosity and activation energy. Using a set of synthetic inversion experiments, we examine sensitivity patterns, explore trade-offs between parameters, and develop a robust framework for high-resolution adjoint-based inversion. With this background, we now examine dynamic topography in greater detail, focusing on its calculation and its role as a constraint on mantle flow.

1.2 Dynamic Topography and Its Significance

Dynamic topography refers to the deflection of the Earth's surface caused by flow in the underlying mantle (Hager and Richards, 1989). As the mantle moves, it applies vertical stresses to the base of the lithosphere, and the resulting surface deformation is balanced by gravitational forces (Davies et al., 2023). This topography is not static; it evolves over time and varies across space depending on the structure and movement of the mantle. It differs from isostatic topography,

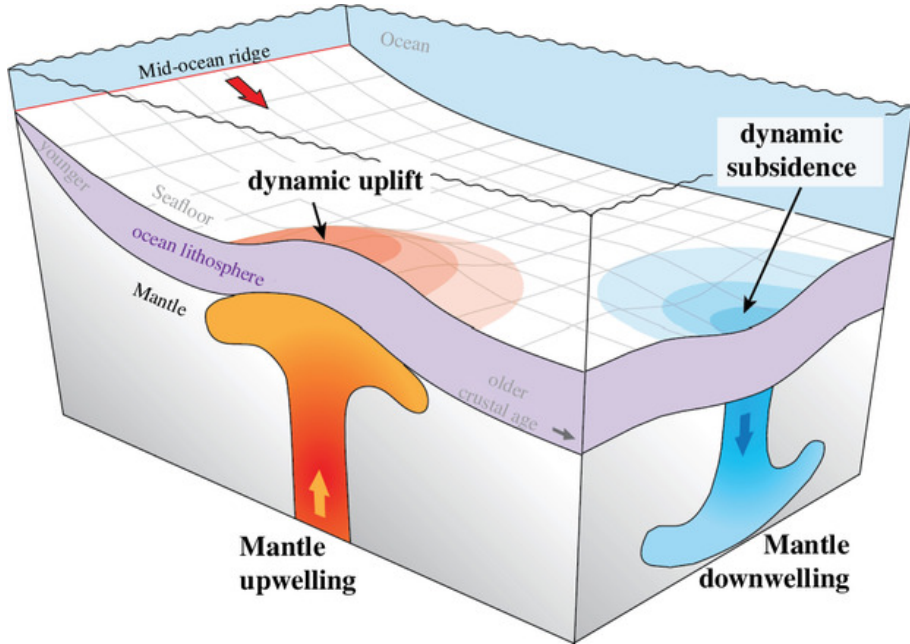


Figure 1.1: Conceptual illustration of dynamic topography driven by mantle flow. Buoyant upwellings in the mantle generate positive surface deflections, whereas dense downwellings induce negative topography through vertical normal stresses. Image taken from Calvelage et al. (2024).

which is driven by static density and thickness variations in the crust and lithosphere. Because dynamic topography is influenced by mantle flow, it can change on million-year timescales and is harder to isolate from observations. It typically produces broad, low-amplitude surface deflections but can reach amplitudes of over a kilometre in some regions (Hoggard et al., 2016). Dynamic topography can be estimated by subtracting all isostatic contributions (due to crustal thickness, density, sediment and ice loading, etc.) from the observed topography, resulting in what is termed *residual topography* (Section 1.2.4). This residual is often taken to represent dynamic topography, although its accuracy depends on the assumptions made during the removal of isostatic and loading contributions (Hoggard et al., 2017).

1.2.1 Early Evidence and Observational Examples

There is strong geological evidence that mantle flow causes vertical movements of the surface over regional to continental scales. One of the earliest examples comes from the sedimentary record of western North America (Liu et al., 2008). Marine sediments from the Late Cretaceous are now found at elevations of around 1 km, which cannot be explained by sea-level change alone. Since global sea level varied between 70–250 m during that time, the region must have

Chapter 1. Introduction

experienced large-scale vertical motion. The distribution of sediment, and the absence of corresponding deposits in the east, suggests that the continent was tilted about a north-south axis, possibly in response to subduction-related mantle flow. Similar interpretations have been made in other regions. In eastern Australia, the sedimentary records of the Eromanga and Carpentaria basins show tilting and flooding that match predictions of flow above shallow subduction zones (DiCaprio et al., 2009). The Russian Platform and southern Africa show comparable patterns in their stratigraphy (Mitrovica et al., 1996). Uplift and subsidence events that are not linked to local tectonics, but occur over areas larger than 1000 km, are interpreted as resulting from mantle-driven flow (Gurnis et al., 2000). The timing of these events is difficult to constrain precisely, but their geologic effects are visible. Cooling ages from thermochronology, or sediment volumes in adjacent basins, can be used to estimate the timing and magnitude of uplift (Gallagher and Brown, 1997). Well-known examples of dynamic topography include (Davies et al., 2023):

- Cenozoic uplift of southern Africa (Gurnis et al., 2000; Pysklywec and Mitrovica, 1999)
- Cretaceous subsidence and later uplift of the North American interior (Mitrovica et al., 1989; Liu et al., 2008)
- Late Cenozoic uplift of the Colorado Plateau (Moucha et al., 2009)
- Miocene tilting of northern South America (Shephard et al., 2010)
- Late Cretaceous to present tilting of Australia (DiCaprio et al., 2009)
- Paleozoic vertical motions of the Slave and Kaapvaal cratons (Zhang et al., 2012)

1.2.2 Significance and Importance of Sensitivity Analysis

Dynamic topography plays an important role in reconstructions of sea level, sedimentary environments, and paleogeography. Since dynamic uplift or subsidence changes the elevation of the land relative to sea level, it affects how we interpret sea-level data (Davies et al., 2023). This is especially important in regions that were previously assumed to be stable. For instance, marine flooding histories and sediment records from passive margins may reflect dynamic subsidence rather than eustatic sea-level rise. As a result, reconstructions of global sea level that are

based on local stratigraphic data can be significantly biased (Czarnota et al., 2013). Dynamic topography also influences how ice-sheet evolution is interpreted. Local sea-level records, often used to infer past ice volume, are affected by vertical land movements. These movements may be caused by tectonics, glacial isostatic adjustment, sediment loading, or dynamic topography. Separating these effects is essential for understanding past climate and sea-level changes (Rovere et al., 2014).

Temporal rates of change are particularly important. Present-day amplitude of dynamic topography does not indicate whether a location is rising or subsiding (Flament et al., 2013). Geological records provide some constraints. On the Northwest Shelf of Australia, dynamic subsidence of up to 75 m/Myr has been inferred (Czarnota et al., 2013), while uplift rates of up to 20 m/Myr are recorded along paleo shorelines (Rovere et al., 2014). Geodynamic models predict a wide range of values (from a few to over 100 m/Myr), depending on mantle viscosity, density structure, and flow geometry. Australia offers a well-documented case study. Dynamic topography across the continent varies by nearly 1 km. Regions such as the Great Australian Bight and North West Shelf show significant subsidence, while areas like the Perth Abyssal Plain are uplifted. These variations have influenced stratigraphy and resource systems, including hydrocarbon migration in the Browse Basin and uplift-driven landscape evolution in southern Australia (Czarnota et al., 2014).

In this context, dynamic topography is not only a surface response to mantle flow but also a critical diagnostic for probing Earth’s interior. The present study builds on this concept by applying adjoint-based sensitivity analysis to quantify how dynamic topography responds to different components of mantle rheology. By systematically evaluating this sensitivity, the work aims to improve the accuracy of rheological parameter estimation and enhance reconstructions of mantle dynamics from surface observations. This is particularly relevant for refining inverse models of mantle structure and for improving geodynamic interpretations of surface features such as basin tilting, continental uplift, and vertical land motion associated with glacial isostatic adjustment.

1.2.3 Surface Processes Affected by Dynamic Topography

Dynamic topography affects many Earth surface systems. It influences sea-level records, sedimentary basin development, erosion, and landscape evolution (Rovere et al., 2014). For exam-

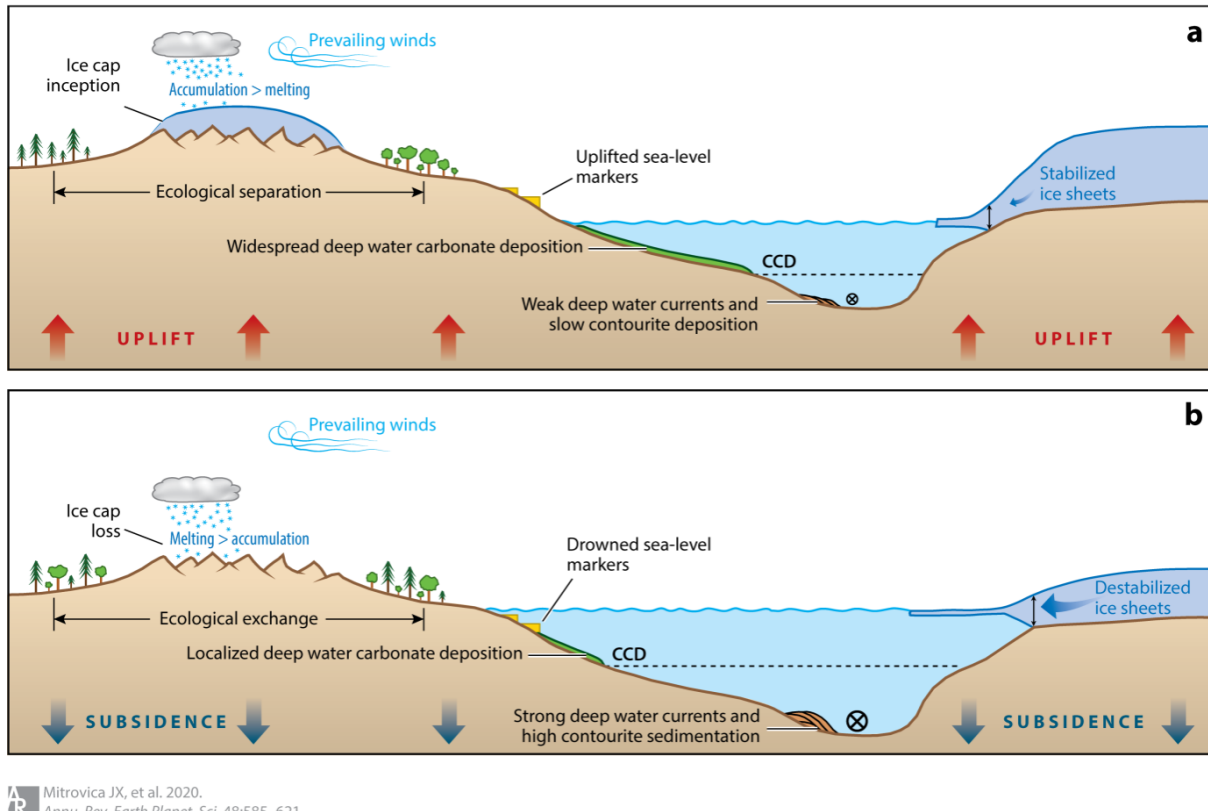


Figure 1.2: Surface processes affected by dynamic topography, including glacial isostatic adjustment, sea-level change, and basin formation (Mitrovica et al., 2020).

ple, dynamic drawdown in the Wilkes Basin in East Antarctica may have made the ice sheet more vulnerable to retreat during the Pliocene (Austermann et al., 2017). Elsewhere, upwelling associated with mantle plumes has been linked to changes in ocean circulation, with potential climate feedbacks. Uplift rates of more than 300 m/Myr have been reported in some plume-influenced regions (Gurnis et al., 2000). Processes affected by dynamic topography include (Davies et al., 2023):

- Local and global sea-level changes
- Ocean current patterns and climate
- Continental flooding and basin formation
- Erosion, landscape, and river system evolution
- Stratigraphy and sediment transport
- Ice-sheet behaviour and glacial isostatic adjustment

- Hydrocarbon generation and migration
- Mineral system development
- Earth's gravity field expression

Overall, dynamic topography acts as a bridge between deep Earth processes and surface environments. Understanding its spatial and temporal evolution is essential for improving reconstructions of past landscapes, sea level, and climate. It also helps constrain key parameters in mantle convection models, especially when used alongside sensitivity analysis and adjoint-based inversion frameworks.

1.2.4 Calculation of Dynamic Topography

There are two main approaches to estimate dynamic topography: measurement of residual topography and prediction using mantle flow models (Davies et al., 2023). Residual topography is calculated by removing the isostatic contributions of sediments, ice, crust, and lithosphere from observed topography. This can be expressed as:

$$h_{\text{res}} = h_{\text{obs}} - h_{\text{iso}} \quad (1.1)$$

where h_{res} is the residual topography, h_{obs} is the observed surface elevation or bathymetry, and h_{iso} is the total isostatic correction accounting for crustal, sedimentary, and lithospheric loads (Guerri et al., 2016; Kaban et al., 2003). This method is most reliable in oceanic regions, where seafloor depth follows a well-understood age-depth relationship due to lithospheric cooling. Deviations from this trend, after correction for sediment and crustal effects, reflect the residual signal. However, global coverage is limited, and corrections are uncertain in regions with thick sediments or complex basement structure (Hoggard et al., 2016, 2017).

The second approach involves predicting surface deflections from mantle flow models, where density anomalies within the mantle generate dynamic stresses at the base of the lithosphere (Ricard et al., 1993; Conrad and Husson, 2009; Colli et al., 2018). The dynamic topography h_{dyn} can be estimated from the normal stress σ_{zz} at the surface via local isostasy:

$$h_{\text{dyn}} = \frac{\sigma_{zz}}{\Delta\rho g} \quad (1.2)$$

where $\Delta\rho$ is the density contrast across the interface (typically between lithosphere and asthenosphere), and g is gravitational acceleration (Davies et al., 2023). These stresses are derived from solving the Stokes flow equations with specified internal density heterogeneities. Sensitivity studies show that the resulting dynamic topography is strongly influenced by shallow mantle structure, particularly in the lithosphere and asthenosphere, while deeper mantle flow contributes primarily to longer-wavelength components of the signal (Valentine and Davies, 2020). Key differences in amplitude and pattern between measured residual topography and predicted dynamic topography emphasize the need for sensitivity analysis and inversion to better constrain mantle properties (Bodur and Rey, 2019).

1.3 Literature Review

Dynamic topography (DT), the surface expression of vertical deformation induced by viscous mantle flow, has emerged as a critical constraint on the structure and evolution of Earth's interior (Yang and Gurnis, 2016; Hoggard et al., 2021; Forte and Rowley, 2022). Numerous studies have used geological records, sedimentary basin architecture, and marine flooding events to reconstruct DT and infer patterns of mantle flow (Lithgow-Bertelloni and Silver, 1998; Guerri et al., 2016; Husson and Conrad, 2006). Examples such as the Cretaceous tilting of North America, Late Cenozoic uplift of the Colorado Plateau, and dynamic drawdown in northwestern Australia illustrate DT's sensitivity to long-wavelength convective processes (Liu et al., 2008; Moucha et al., 2009; DiCaprio et al., 2009). These reconstructions, often supported by geodynamic modelling, highlight DT as a diagnostic signal of density-driven flow in the mantle. Several efforts have leveraged DT to constrain mantle viscosity, with early adjoint-based studies by Spasojevic et al. (2009) and Liu and Gurnis (2008) using subduction-driven flow models to infer surface uplift and viscosity contrasts. Subsequent studies, including those by Colli et al. (2016) and Ghelichkhan et al. (2021), applied similar methods on global scales, recovering viscosity structures using residual topography observations and testing lower mantle dynamics.

While forward models, typically formulated in spherical shell or 2D annular domains, solve the governing equations of mantle flow and incorporate plate reconstructions, they often assume radially symmetric viscosity profiles (Spasojevic et al., 2009; Steinberger et al., 2010; Monnereau and Quéré, 2001; Euen et al., 2023). This simplification neglects lateral viscosity variations that play a significant role in shaping observed DT. Despite reproducing large-scale patterns, these models commonly overestimate DT amplitudes, primarily due to uncertainties in seismic-to-thermal conversions and poorly constrained viscosity structure, particularly at depth (Molnar et al., 2015; Davies et al., 2019; Hoggard et al., 2021, 2016). Interpretation of seismic tomography remains complicated by trade-offs between thermal and compositional effects, non-linear sensitivities, and limited resolution, especially in the deep mantle (Rawlinson et al., 2014; Liu and Gu, 2012). Complementary datasets such as gravity anomalies, the geoid, global plate reconstructions, and geochemical signals provide valuable constraints, yet integrating them consistently within a unified modelling framework remains a complex challenge (Lieb et al., 2016; Mao and Zhong, 2021). Furthermore, the reliance on assumed initial conditions limits forward models' ability to reconstruct the time-dependent evolution of mantle flow (Müller et al., 2018; Colli et al., 2015).

To address these shortcomings, inverse geodynamic methods have been developed to directly recover internal Earth properties from surface observables . In particular, adjoint-based approaches offer computationally efficient gradient calculations with respect to model parameters, enabling systematic sensitivity analyses and iterative refinement of physical fields (Ghelichkhan and Bunge, 2016; Horbach et al., 2014; Worthen et al., 2014). These methods reverse the traditional forward modelling paradigm by allowing observational data to inform and constrain mantle structure (Carrassi et al., 2018). Applications range from recovering initial temperature conditions and inferring rheological profiles to evaluating the sensitivity of DT and surface velocities to internal variations (Li et al., 2017; Reuber et al., 2020; Crawford et al., 2018; Colli et al., 2015). While early implementations were limited by simplified rheologies, idealized domains, and restrictive codebases, recent advancements such as the G-ADOPT (Geoscientific ADjoint Optimisation PlaTform) framework given by Ghelichkhan et al. (2024) have significantly expanded the scope of inverse modelling.

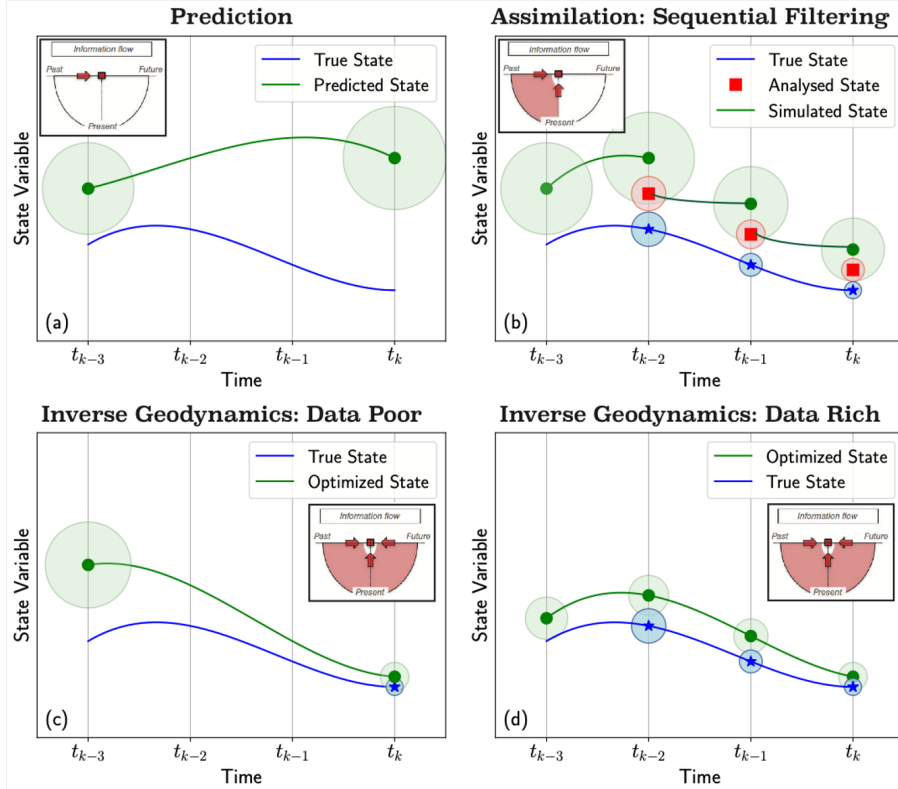


Figure 1.3: Illustration of estimation strategies: (a) forward prediction; (b) sequential filtering with past and present data. Inverse geodynamics (c) enables recovery of past mantle states using present-day surface data, with improved accuracy when data coverage is rich (d). This highlights the strength of adjoint-based inversion in extracting deep Earth information from surface observables. Adapted from Carrassi et al. (2018); Davies et al. (2023).

Built on the Firedrake finite element system (Rathgeber et al., 2016) and utilizing UFL-based automatic differentiation (Alnæs et al., 2014), G-ADOPT allows derivation of adjoint equations for nonlinear, coupled PDEs on unstructured meshes, enabling inversion over variables such as viscosity, activation energy, and initial thermal states. It also supports modular workflows and integration of diverse surface observables. While DT alone may not uniquely constrain mantle structure due to trade-offs with density and rheology, combining it with surface velocity data improves resolution and helps disentangle lithospheric and deeper mantle contributions. Surface velocities derived from GPS and plate reconstructions provide lateral strain information that complements DT's vertical stress signature (Haines et al., 2015; Bastos et al., 2010; Osei Tutu et al., 2018). Additional observables, such as gravity and the geoid, provide density constraints, although their interpretation remains nontrivial (Mao and Zhong, 2021). Joint inversion frameworks that incorporate multiple datasets, as implemented within G-ADOPT, re-

duce non-uniqueness and enhance robustness, offering a more reliable path toward constraining Earth's mantle dynamics.

1.3.1 Research Gaps

Based on the findings from previous studies, some important limitations remain in current geodynamic modelling and inversion approaches:

- **Initial Condition Problem:** Most studies rely on forward modelling approaches, which require assumptions about the mantle's past thermo-chemical state. Since this state cannot be uniquely inferred from present-day observations, forward models cannot reliably reconstruct mantle evolution through geological time.
- **Limitations of Mantle Circulation Models:** Even advanced models that incorporate global plate reconstructions and present-day seismic tomography are constrained by the same initial condition uncertainty. These models also rely on tomographic inputs that suffer from limited resolution, particularly in the lower mantle, and are affected by trade-offs between thermal and compositional effects.
- **Simplified Rheologies:** Many previous studies assume radially symmetric viscosity profiles, neglecting lateral variations that play a crucial role in generating and shaping the surface expression of dynamic topography.
- **Sparse Residual Topography Data:** Residual topography which is an important observable for constraining mantle flow is sparsely distributed and particularly uncertain over continental interiors. Inaccuracies in sediment, crustal, and lithospheric corrections further reduce its effectiveness as a robust constraint.
- **Computational Challenges:** Fully time-dependent global mantle convection models are computationally intensive and often infeasible for detailed sensitivity analyses or large-scale inverse problems. While more simplified instantaneous flow models are computationally tractable, they must be carefully validated and interpreted.

Thus, a need remains for inverse geodynamic methods that (i) efficiently propagate surface constraints backward in time, (ii) resolve lateral viscosity variations, and (iii) combine multiple

surface observables. This thesis attempts to address these issues using a fully adjoint-based inversion framework within G-ADOPT, applied to synthetic 2D annular models with realistic rheological assumptions and joint constraints from dynamic topography and surface velocity.

1.4 Research Objectives

This study is motivated by the need to better understand the connection between mantle flow and its surface expression, particularly dynamic topography. The main objectives which guide the work are:

- **To investigate the sensitivity of dynamic topography to different components of mantle flow.** This includes assessing how variations in viscosity, density, and rheological parameters influence the amplitude and spatial pattern of dynamic topography, and identifying which regions of the mantle exert the strongest control on surface signals.
- **To recover the rheological structure of the mantle using adjoint-based inversion.** The goal is to constrain spatial variations in viscosity or activation energy by using surface observables, primarily dynamic topography and surface velocity, through the computation of sensitivity fields and solution of the resulting inverse problem.
- **To evaluate how joint inversion of dynamic topography and surface velocity improves constraints on mantle rheology,** addressing trade-offs and reducing nonuniqueness in parameter recovery.
- **To explore the impact of regularization strategies and model design choices,** including control variable selection and the imposition of physical bounds, on the stability and accuracy of inversion results.
- **To assess the capabilities of the G-ADOPT framework** for high-resolution, nonlinear adjoint-based geodynamic inversion, including its treatment of sensitivity coupling and resolution limits.
- **To provide a foundation for future extensions,** including visco-plastic rheologies, uncertainty quantification, time-dependent GIA modeling, and joint inversion with additional datasets such as gravity, geoid, and sedimentary records.

Together, these objectives establish a framework to advance quantitative inference of mantle structure from surface observations.

1.5 Methodology Overview

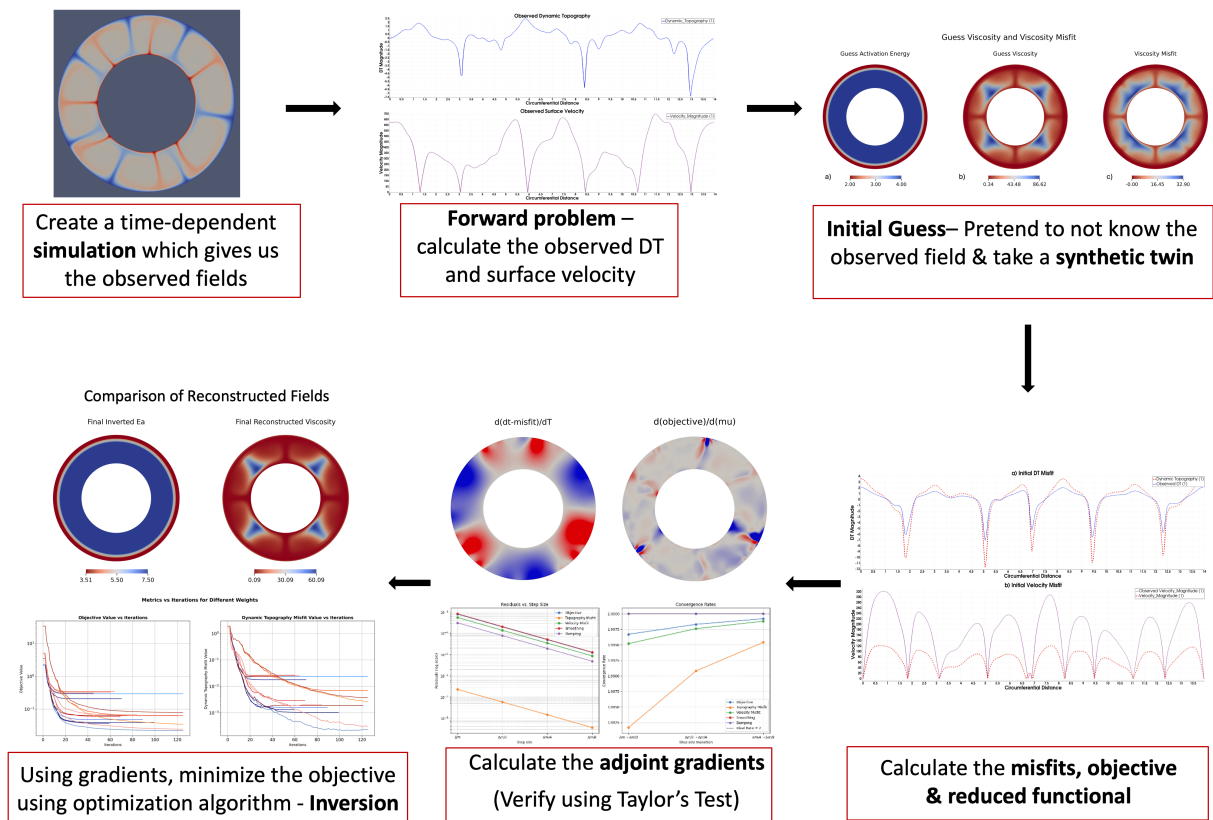


Figure 1.4: Schematic workflow of the inversion framework used in this study. Starting from synthetic data generation, the process proceeds through misfit evaluation, gradient computation using the Gadopt, and optimization.

To achieve these objectives, we develop and implement a fully adjoint-based geodynamic inversion workflow using the G-ADOPT framework as shown in Figure 1.4. The approach involves a synthetic 2D annular mantle convection model with a temperature-dependent viscosity field. We use surface observations, namely dynamic topography and surface velocity, to constrain the spatial distribution of mantle viscosity and activation energy, depending on the inversion setup (described in detail in Chapters 4, 5). By formulating the inverse problem in log-viscosity space and computing adjoint-based sensitivity fields, we quantify how changes

in rheological parameters influence observable surface signals. This workflow enables high-resolution inversion frameworks under a range of assumptions, and provides a controlled setting to evaluate sensitivity, regularization strategies, and the effectiveness of joint constraints.

1.6 Thesis Organization

This thesis is organized into six chapters, as outlined below:

- **Chapter 1** introduces the motivation behind this work and outlines the role of dynamic topography in understanding mantle dynamics. It discusses observational evidence, the significance of surface observables, and the challenges associated with interpreting dynamic topography. A detailed literature review is provided, highlighting the limitations of existing forward and inverse models. The chapter concludes by stating the research objectives and giving an overview of the inversion framework.
- **Chapter 2** presents the theoretical and computational formulation of the forward problem. It outlines the governing equations for incompressible Stokes flow and thermal energy conservation, describes the visco-plastic rheology model, and details the finite element discretization. The chapter also covers the procedure for computing surface observables such as dynamic topography and velocity from the numerical model.
- **Chapter 3** develops the inverse modeling framework based on adjoint methods. It introduces the objective functional used to quantify misfit, outlines regularization and normalization strategies, and derives the discrete adjoint equations. The chapter further discusses gradient verification via Taylor remainder tests and describes the gradient-based optimization algorithm employed in the inversion.
- **Chapter 4** presents the numerical implementation and inversion results using field-based control parameters, specifically viscosity and temperature. It describes the software framework (G-ADOPT), the setup for generating synthetic data, and the sequence of inversion configurations. Results from these studies highlight the sensitivity of surface observables and the role of regularization.
- **Chapter 5** extends the inversion framework by focusing on activation energy as the

control parameter. Starting with a single uniform value, the analysis moves to depth-dependent profiles and finally to fully varying fields within a non-linear visco-plastic mantle model. These cases test how well activation energy can be recovered under increasingly realistic and complex rheological conditions.

- **Chapter 4** summarizes the key findings of the study and discusses the broader implications. It highlights the main contributions, outlines current limitations, and suggests directions for future work, including uncertainty quantification and the incorporation of additional data constraints.

Chapter 2

Theoretical and Computational Framework for Forward Modeling

This chapter presents the theoretical and computational framework used to simulate mantle flow governed by temperature-dependent, visco-plastic rheology. We outline the governing equations for incompressible Stokes flow and thermal energy conservation, followed by their finite element discretization in a 2D annular domain. The numerical setup incorporates nonlinear viscosity, internal heating, and free-slip boundary conditions, enabling realistic modeling of mantle convection and the resulting surface signals, such as dynamic topography and velocity. We begin by generating synthetic dynamic topography and surface velocity data through time-dependent forward modeling. A reference model is obtained by spinning up a mantle convection simulation from a prescribed initial condition. Since mantle evolution is governed by its past thermal state, the present-day structure can be predicted by solving the coupled conservation equations for mass, momentum, and energy. The synthetic solution serves as a baseline against which inversion results are compared. This forward setup provides a controlled environment to assess how variations in rheological parameters influence surface observables. The formulation of the inverse modeling framework, including the adjoint-based gradient computation and optimization strategy, are discussed in the next chapter (Chapter 3).

2.1 Governing Equations of Mantle flow

Mantle flow is governed by the conservation equations for mass, momentum, and energy. In this study, we solve the non-dimensional form of these equations under the assumptions of incompressibility and the Boussinesq approximation (McKenzie et al., 1973). The system of

equations is given by: The conservation of mass (incompressibility condition) is given by:

$$\nabla \cdot \mathbf{u} = 0 \quad (2.1)$$

The conservation of momentum is expressed as:

$$-\nabla p + \nabla \cdot (2\mu \dot{\epsilon}) + Ra T \hat{\mathbf{z}} = 0 \quad (2.2)$$

The energy equation governs the flow of temperature and is given by:

$$\frac{\partial T}{\partial t} + \mathbf{u} \cdot \nabla T - \nabla^2 T = 0 \quad (2.3)$$

The Rayleigh number Ra is defined as:

$$Ra = \frac{\rho_0 g \alpha \Delta T L^3}{\kappa \mu_0} \quad (2.4)$$

The strain-rate tensor used in Eq. (2.2) is given by:

$$\dot{\epsilon} = \frac{1}{2} (\nabla \mathbf{u} + \nabla \mathbf{u}^T) \quad (2.5)$$

Free-slip boundary conditions are applied on all mechanical boundaries. Thermally, we impose fixed temperatures at the top and bottom boundaries, while the sidewalls are treated as insulating (zero normal heat flux). We define the time interval of interest as $I = [t_I, t_F]$, with the computational domain V bounded by ∂V . The top and bottom boundaries are denoted by S and C , respectively. For all simulations, we apply free-slip and impermeable velocity boundary conditions on all domain boundaries. Temperature boundary conditions are prescribed as constant values: T_S at the surface (top boundary) and T_C at the base (bottom boundary), representing the crust–mantle and core–mantle boundaries, respectively.

Symbol	Description	Symbol	Description
\mathbf{u}	Velocity vector	p	Dynamic pressure
T	Temperature	μ	Dynamic viscosity
$\dot{\epsilon}$	Strain-rate tensor	Ra	Rayleigh number
ρ_0	Reference density	g	Gravitational acceleration
α	Thermal expansion coefficient	κ	Thermal diffusivity
ΔT	Temperature difference across domain	L	Characteristic length scale
μ_0	Reference viscosity	\mathbf{n}	Outward normal vector
\mathbf{s}	Tangential vector	t_I, t_F	Initial and final time
V	Computational domain	∂V	Domain boundary
S	Top boundary (Surface)	C	Bottom boundary (CMB)
T_S	Temperature at top boundary	T_C	Temperature at bottom boundary
$T_{IC}(\mathbf{x})$	Initial temperature distribution	$\hat{\mathbf{z}}$	Unit vector in gravity direction

Table 2.1: List of symbols used in Eqs. (2.1)–(2.7).

Specifically, we assume the following boundary conditions:

$$\mathbf{u}(\mathbf{x}, t) \cdot \mathbf{n} = 0, \quad \mathbf{x} \in \partial V, t \in I \quad (2.6a)$$

$$[\mu \dot{\epsilon}(\mathbf{u}(\mathbf{x}, t)) \cdot \mathbf{n}] \cdot \mathbf{s} = 0, \quad \mathbf{x} \in \partial V, t \in I \quad (2.6b)$$

$$T(\mathbf{x}, t) = T_S, \quad \mathbf{x} \in S, t \in I \quad (2.6c)$$

$$T(\mathbf{x}, t) = T_C, \quad \mathbf{x} \in C, t \in I \quad (2.6d)$$

In Eqs. (2.6), \mathbf{n} is the outward-pointing normal vector, and \mathbf{s} represents any tangential direction.

For our setup, we heat the bottom boundary to represent the core–mantle boundary, setting $T_C = 1.0$. The top boundary, approximating Earth’s surface (crust–mantle boundary), is cooled and maintained at $T_S = 0.0$.

Since mantle convection is an initial value problem, we prescribe an initial temperature distribution at time t_I as:

$$T(\mathbf{x}, t_I) = T_{IC}(\mathbf{x}), \quad \mathbf{x} \in V \quad (2.7)$$

Thus, the viscous flow problem can be formulated in terms of three primary variables: pressure (p), velocity (\mathbf{u}), and temperature (T). The governing equations, combined with the appropriate boundary and initial conditions, provide a complete system that can be solved to obtain all three unknowns simultaneously. These equations are solved using the finite element method, which offers a computationally efficient and accurate framework. The details of the formulation and implementation are presented in the subsequent sections.

2.2 Rheological Model

Previous studies have established that the mantle exhibits a viscoplastic rheology (Cathles, 2015). The viscosity of the mantle is not uniform but depends on factors such as depth, temperature, and strain-rate (Tosi et al., 2015). While the variations with depth and temperature are typically considered linear (especially in a log-viscosity sense), the non-linear behavior arises from the strain-rate dependence. The linear part of the viscosity is commonly modeled using the Arrhenius law, which captures the thermally activated nature of mantle deformation. The linear viscosity component depends on temperature and depth as:

$$\mu_{\text{lin}}(T, z) = \exp(-E_{aT}T + E_{az}z) \quad (2.8)$$

where the parameters E_{aT} and E_{az} control the overall viscosity contrast due to temperature and depth, respectively, and are defined as:

$$E_{aT} = \ln(\Delta\mu_T), \quad E_{az} = \ln(\Delta\mu_z)$$

The non-linear (plastic) component of viscosity is described by:

$$\mu_{\text{plast}}(\dot{\epsilon}) = \mu^* + \frac{\sigma_y}{\sqrt{\dot{\epsilon} : \dot{\epsilon}}} \quad (2.9)$$

The total viscosity field μ is then calculated by combining the linear and non-linear components using a harmonic mean:

$$\mu = \left(\frac{1}{\mu_{\text{lin}}} + \frac{1}{\mu_{\text{plast}}} \right)^{-1} \quad (2.10)$$

This approach ensures that the effective viscosity is always controlled by the weaker of the two mechanisms, allowing the model to transition smoothly between fluid-like and plastic behavior depending on local stress conditions.

Symbol	Meaning	Symbol	Meaning
T	Temperature	z	Depth
μ_{lin}	Linear viscosity component	μ_{plast}	Plastic viscosity component
μ^*	Effective viscosity at high stress	σ_y	Yield stress
$\dot{\varepsilon}$	Strain-rate tensor	$\dot{\varepsilon} : \dot{\varepsilon}$	Second invariant of strain-rate tensor
$\Delta\mu_T$	Viscosity contrast due to temperature	$\Delta\mu_z$	Viscosity contrast due to depth
E_{aT}	Temperature activation parameter	E_{az}	Depth activation parameter

Table 2.2: Definition of symbols used in Eqs. (2.8)–(2.9)

This formulation describes a stress-dependent viscosity, with μ^* denoting the limiting (minimum) viscosity attained under high-stress conditions. σ_y is the yield stress, and $\sqrt{\dot{\varepsilon} : \dot{\varepsilon}}$ is the second invariant of the strain-rate tensor. At low stresses, the material behaves as a linear viscous fluid. However, when stresses exceed the yield threshold σ_y , plastic deformation becomes dominant, resulting in a rapid decrease in viscosity. This decrease is limited by the lower bound μ^* .

In this research, we investigate the sensitivity of dynamic topography to different rheological formulations and assess its effectiveness in recovering the initial mantle state under varying levels of model complexity. Our approach is structured progressively to evaluate the influence of different physical controls on viscosity. We begin with a simplified rheological model in which viscosity depends solely on temperature. This allows us to isolate the effects of thermal variations on mantle flow and surface topography in a fully smooth and differentiable setting, suitable for adjoint-based sensitivity analysis. Next, we explore a linear rheological model with depth-dependent viscosity. This formulation introduces depth-dependent variations

in viscosity, which reflect abrupt changes or gradients associated with phase transitions and pressure-induced effects. This addition allows us to examine how vertical structure influences the expression of dynamic topography. Building on this, we perform a series of synthetic inversion experiments using a fully viscoplastic rheology. This model accounts for both temperature and depth dependence, as well as strain-rate weakening arising from plastic deformation.

2.3 Finite Element Method

The finite element method (FEM) is a widely used numerical technique for solving partial differential equations (PDEs) in problems involving complex geometries and boundary conditions, such as those encountered in geodynamic modeling (May et al., 2013; Gerya, 2019). In FEM, the domain is divided into smaller subdomains (elements), over which the solution is approximated using piecewise continuous basis functions. The governing equations are recast in a weak (variational) form and solved numerically based on these approximations (Elman et al., 2014).

In this work, FEM is used to discretize and solve the equations governing mantle convection. The approach includes selecting suitable function spaces for the solution variables, deriving the weak forms of the governing equations, assembling the global system, and solving it using appropriate numerical solvers. This process broadens the class of admissible solutions and facilitates the incorporation of boundary conditions. The computational domain is discretized into smaller elements (e.g., triangles or quadrilaterals in 2D), and the solution and test functions are approximated using basis functions defined on finite-dimensional function spaces over these elements.

Solving the resulting system involves the following key steps:

- Choosing appropriate function spaces for each physical variable (e.g., velocity, pressure, temperature),
- Deriving the weak forms of the governing equations,
- Assembling the global system matrix and vectors from local element contributions, and
- Solving the resulting algebraic system using suitable linear or nonlinear solvers.

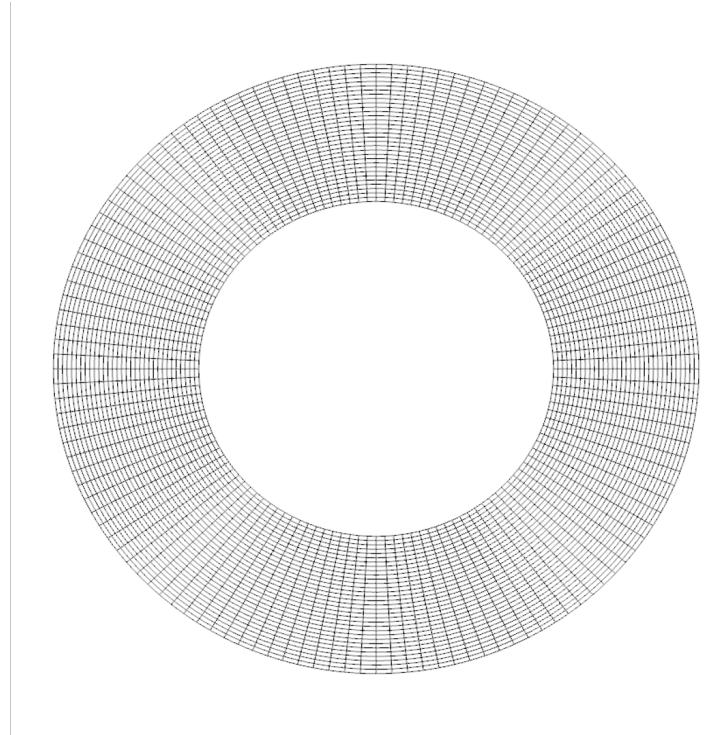


Figure 2.1: Annular mesh used in the 2D cylindrical mantle convection model. The mesh is extruded in the azimuthal direction to create structured layers.

For our model, the computational domain is an annular region, representing a 2D cylindrical shell. We use an *extruded mesh* to construct this geometry, which allows us to define a structured grid in the radial and azimuthal directions. A representative mesh used in our simulations is shown in Figure 2.1. In our finite element formulation, the velocity field \mathbf{u} is a vector-valued function, pressure p is scalar-valued, and temperature T is also scalar-valued. These are discretized in appropriate function spaces:

- **Vector function space:** used for velocity \mathbf{u} (e.g., `VectorFunctionSpace`),
- **Scalar function space:** used for pressure p and temperature T (e.g., `FunctionSpace`),
- **Mixed function space:** used to couple velocity and pressure in a unified variational formulation,
- **Real function space:** used for global scalar quantities such as integrated constraints or Lagrange multipliers.

FEM provides flexibility in choosing different discretizations (e.g., continuous Galerkin, discontinuous Galerkin) and supports a wide range of element types and polynomial orders. In

this work, we employ the FEM framework provided by Firedrake (Rathgeber et al., 2016; Gibson et al., 2019), a high-level finite element library that automates the assembly and solution process using symbolic representations of PDEs. In the following sections, we describe how the Stokes equations (mass and momentum conservation) and the energy equation are discretized and solved in an annular domain using Firedrake (Rathgeber et al., 2016).

2.4 Solution Procedure

2.4.1 Finite Element Discretization

To derive the finite element discretization of Eqs. (2.1), (2.2), and (2.3), which represent the conservation of mass, momentum, and energy, we begin by expressing these equations in their weak form (see Davies et al. (2022) for more detailed explanation). This requires selecting appropriate function spaces V , W , and Q that contain the solution fields for velocity \mathbf{u} , pressure p , and temperature T , respectively. These spaces also define the corresponding test functions $\mathbf{v} \in V$, $w \in W$, and $q \in Q$, which are used in the variational formulation of the problem. To derive the weak form, each governing equation is multiplied by a suitable test function and integrated over the domain Ω .

$$\int_{\Omega} (\nabla \mathbf{v}) : \mu (\nabla \mathbf{u} + \nabla \mathbf{u}^T) dx - \int_{\Omega} (\nabla \cdot \mathbf{v}) p dx - \int_{\Omega} Ra T \mathbf{v} \cdot \hat{\mathbf{k}} dx = 0 \quad \text{for all } \mathbf{v} \in V, \quad (2.11)$$

$$\int_{\Omega} w (\nabla \cdot \mathbf{u}) dx = 0 \quad \text{for all } w \in W, \quad (2.12)$$

$$\int_{\Omega} q \frac{\partial T}{\partial t} dx + \int_{\Omega} q \mathbf{u} \cdot \nabla T dx + \int_{\Omega} (\nabla q) \cdot (\kappa \nabla T) dx = 0 \quad \text{for all } q \in Q. \quad (2.13)$$

Equations (2.11), (2.12), and (2.13) represent the weak form of the continuous PDEs given in the strong form Eqs. (2.2), (2.1), and (2.3). To solve these equations numerically using the finite element method, we restrict the continuous function spaces to finite-dimensional subspaces. This is achieved by discretizing the computational domain Ω into a finite number of elements or cells (typically quadrilateral or triangular in 2D), over which the solution fields are approximated using polynomial basis functions. Within each element, the solution is represented using piecewise polynomial functions of a specified degree. The global solution is then assembled

by ensuring a certain degree of continuity across element boundaries. For instance, continuous Galerkin (CG) elements impose continuity of the solution across cell interfaces, making them suitable for problems requiring differentiable fields like velocity and temperature.

Firedrake provides a wide range of function space options, including scalar, vector, tensor, and mixed spaces, with varying polynomial degrees (Kirby and Mitchell, 2019). The choice of function spaces is problem-dependent and must satisfy certain numerical stability conditions. For the Stokes system, comprising the momentum and mass conservation equations, stability is governed by the Ladyzhenskaya–Babuška–Brezzi (LBB) condition (Thieulot and Bangerth, 2022). To satisfy this, we use a mixed function space with Q_2 elements for velocity and Q_1 elements for pressure (commonly referred to as the Q_2 – Q_1 Taylor–Hood element pair).

For the energy equation, we discretize the temperature field using Q_2 elements when solving the forward thermal problem. However, when temperature is treated as a control variable in the inversion analysis, we use a Q_1 discretization. This choice facilitates the application of regularization techniques (e.g., Tikhonov regularization), which help stabilize the inversion and ensure smoothness of the recovered temperature field. These discretization choices ensure both numerical stability and physical fidelity of the solution, while allowing flexibility in implementing inverse problems and sensitivity analyses. In practice, implementing these discretization choices requires that we have a well-defined basis for each function space. This allows us to express any solution as a combination of known basis functions. For example, let ϕ_i be the basis functions for the finite-dimensional temperature space Q_h . Then, the temperature field $T(\mathbf{x})$ can be written as:

$$T(\mathbf{x}) = \sum_i T_i \phi_i(\mathbf{x}) \quad (2.14)$$

Here, T_i are the unknown coefficients (or degrees of freedom), and the solution is constructed by summing their contributions weighted by the basis functions ϕ_i . Once the solution is expressed in terms of basis functions, the finite element method proceeds by substituting these into the weak form of the governing equations. This converts the continuous variational problem into a discrete algebraic system, where the goal is to solve for the unknown coefficients T_i , u_i , and p_i associated with the temperature, velocity, and pressure fields. In geometries such as our 2D annular domain, the mesh consists of quadrilateral elements that conform to the cylindrical structure. In Firedrake, we use an *extruded mesh*, where a structured mesh in the radial direction

is extended azimuthally to construct the full domain. Each mesh element maps a reference cell (e.g., a unit square) to its physical location, typically using bilinear shape functions for low-order elements. Each element contributes local stiffness and mass matrices, which are combined into a global system using the connectivity of the basis functions. Continuity across elements is maintained by the function space choice; for example, continuous Galerkin (CG) elements ensure that field variables are continuous across element boundaries.

2.4.2 Boundary Conditions

Boundary conditions are incorporated in the finite element framework either strongly or weakly, depending on the nature of the constraint. In our model, we apply:

- **Strong Dirichlet conditions** on temperature, fixing it to $T_C = 1.0$ at the inner boundary (core–mantle) and $T_S = 0.0$ at the outer boundary (surface).
- **Free-slip conditions** on velocity at both boundaries, allowing tangential flow but preventing normal flow through the boundaries.

The free-slip condition for velocity, as given in Eqs. (2.11), (2.12), requires:

$$\mathbf{u} \cdot \mathbf{n} = 0 \quad \text{on } \partial\Omega, \tag{2.15}$$

which ensures impermeability. This is enforced by restricting the test function space $\mathbf{v} \in V_0$ such that $\mathbf{v} \cdot \mathbf{n} = 0$ on $\partial\Omega$. The zero shear stress condition is imposed weakly by omitting the viscous boundary term in Eq. (2.11):

$$\int_{\partial\Omega} \mathbf{v} \cdot [\mu (\nabla \mathbf{u} + \nabla \mathbf{u}^T) \cdot \mathbf{n}] ds, \tag{2.16}$$

effectively setting the tangential component of surface traction to zero. Likewise, the surface integral arising from the pressure gradient term in Eq. (2.1),

$$\int_{\partial\Omega} \mathbf{v} \cdot p \mathbf{n} ds, \tag{2.17}$$

vanishes under the free-slip condition since $\mathbf{v} \cdot \mathbf{n} = 0$.

For temperature, since we use strong Dirichlet conditions, the test functions $q \in Q_0$ vanish on the boundary. As a result, the surface integral associated with the diffusive heat flux in Eq. (2.13) also vanishes:

$$\int_{\partial\Omega} q \kappa \nabla T \cdot \mathbf{n} ds = 0. \quad (2.18)$$

In Chapter 4, we describe how this discretization framework is implemented for Stokes and energy equations using Firedrake, and how appropriate boundary conditions and solver configurations are applied.

2.4.3 Solution process for temperature, velocity and pressure

In our mantle convection simulations, the energy equation is time-dependent and must be integrated forward in time (Davies et al., 2022; Ghelichkhan et al., 2024). To do this, we use a standard θ -scheme, a time-stepping method that linearly interpolates between fully explicit and fully implicit approaches. Specifically, we use the Crank–Nicolson method (Kramer et al., 2012), which corresponds to $\theta = 0.5$, providing second-order accuracy in time. The weak form of the energy equation at time step $n + 1$ is given by:

$$\int_{\Omega} q \frac{T^{n+1} - T^n}{\Delta t} dx + \int_{\Omega} q \mathbf{u} \cdot \nabla T^{n+\theta} dx + \int_{\Omega} \nabla q \cdot \kappa \nabla T^{n+\theta} dx = 0, \quad (2.19)$$

for all test functions $q \in Q$, where

$$T^{n+\theta} = \theta T^{n+1} + (1 - \theta) T^n. \quad (2.20)$$

is interpolated between the temperature solutions T^n and T^{n+1} at the beginning and end of the $(n + 1)$ -th time step using a parameter $0 \leq \theta \leq 1$.

This formulation couples the temperature field with the velocity field \mathbf{u} via the advection term. In our approach, the Stokes equations (mass and momentum conservation) and the energy equation are solved in a time-splitting fashion in which the Stokes system is solved for velocity and pressure using the current temperature field to compute buoyancy forces; then, the updated

velocity is used to advance the temperature field in time. This procedure is repeated at each time step. The single residual weak form of the Stokes system derived from equations Eqs. (2.11), (2.12) and the B.C.s is given by:

$$\begin{aligned} \int_{\Omega} (\nabla \mathbf{v}) : \mu (\nabla \mathbf{u} + \nabla \mathbf{u}^T) dx - \int_{\Omega} (\nabla \cdot \mathbf{v}) p dx - \int_{\Omega} Ra T \mathbf{v} \cdot \hat{\mathbf{z}} dx \\ - \int_{\Omega} w \nabla \cdot \mathbf{u} dx = 0, \end{aligned} \quad (2.21)$$

for all test functions $\mathbf{v} \in V$ and $w \in W$. This system is linear when the viscosity is constant (isoviscous), and is solved using standard linear solvers provided by Firedrake. In our simulations, we use mixed finite element spaces with Q_2 elements for velocity and Q_1 elements for pressure (Taylor–Hood elements), which satisfy the LBB condition for stability. For 2D cases, a direct solver is generally sufficient, thus we have used direct solvers for our simulations (Davies et al., 2022).

In our 2D cylindrical model with free slip boundary conditions, the velocity solution may contain certain non-physical modes that still satisfy the governing equations. One of the most common of these is a rotational mode, where the entire velocity field rotates as a rigid body. Since free-slip boundaries do not constrain motion along the boundary, the equations allow this kind of rotation without any restoring force. Although this rotation is mathematically valid, it does not represent any meaningful physical motion in the mantle and must be treated carefully during numerical solution. The pressure field also includes a similar issue. The equations we solve determine only the gradient of the pressure, not its absolute value. This means that we can add any constant to the pressure field, and the velocity solution will remain the same. As a result, the pressure is only defined up to a constant, and this needs to be accounted for when solving the system numerically. Both of these are examples of what are called *null modes* (May and Moresi, 2008). They are not errors, but rather degrees of freedom that do not affect the physical solution. If left untreated, they can cause the numerical solver to become unstable or unable to converge. In practice, they are typically handled by constraining the pressure at a single point and by removing the rotational component from the velocity field during the solution process. These null spaces are handled in Firedrake by supplying the solver with appropriate null space vectors (Davies et al., 2022). Overall, the time-stepping scheme and the splitting approach allow us to simulate mantle convection efficiently, coupling the Stokes and thermal fields while maintaining numerical stability and physical accuracy.

2.5 Calculation of Dynamic Topography and Surface Velocity

Once the Stokes system is solved for the velocity \mathbf{u} and pressure p , we can compute derived surface observables i.e. dynamic topography and surface velocity, which serve as the observables in our inversion framework. Dynamic topography arises from vertical normal stresses exerted at the surface due to mantle flow (Hager and Richards, 1989). Under the assumption of local isostasy and ignoring elastic lithospheric response, dynamic topography can be estimated by the vertical stress balance at the surface (Davies et al., 2023):

$$h_{\text{dyn}} = \frac{1}{\Delta\rho g} \sigma_{zz} \Big|_{z=z_s}, \quad (2.22)$$

where σ_{zz} is the vertical normal stress at the surface $z = z_s$, g is the gravitational acceleration, and $\Delta\rho$ is the density contrast between the mantle and overlying material (lithosphere or water). The normal stress is extracted from the Cauchy stress tensor:

$$\sigma_{ij} = -p\delta_{ij} + 2\mu \dot{\varepsilon}_{ij}, \quad (2.23)$$

and projected along the outward normal direction \mathbf{n} :

$$\sigma_{nn} = \mathbf{n} \cdot \boldsymbol{\sigma} \cdot \mathbf{n}. \quad (2.24)$$

Similarly, the surface velocity is directly extracted from the computed velocity field \mathbf{u} by evaluating it at the upper boundary of the domain:

$$\mathbf{u}_{\text{surf}} = \mathbf{u} \Big|_{z=z_s}. \quad (2.25)$$

In our cylindrical geometry, this corresponds to evaluating \mathbf{u} along the outer circle (Earth's surface). These surface velocities can be compared against geodetic or plate motion data and are also used in the inversion framework as observational constraints, complementing the dynamic

topography.

In addition, we solve the Stokes' equations using an initial or incorrect set of parameters (viscosity, temperature, activation energy, etc.) to obtain model predictions for dynamic topography and surface velocity. These predicted fields, which we refer to as the synthetic twins, typically differ from the observed data due to inaccuracies in the assumed model parameters. The resulting discrepancies, referred to as misfits, are quantitatively evaluated and form the basis of the inversion process. By minimizing this misfit through optimization, we iteratively adjust the model parameters to bring the simulated outputs closer to the observations. The implementation of this would be shown in Chapter 4 and 5. In this chapter, we presented the governing equations and numerical formulations used to model mantle flow, incorporating realistic temperature- and stress-dependent viscosity. The inverse problem setup, including adjoint-based gradient computation and optimization strategy, is introduced in the next chapter.

Chapter 3

Adjoint-Based Geodynamic Inversion Framework

In this chapter, the mathematical framework used to solve the inverse problem associated with our mantle convection model described in Chapter 2 is explained. The goal of the inversion is to infer unknown model parameters, such as temperature, viscosity, or activation energy, from observable data including dynamic topography and surface velocities. The inverse problem is posed as a PDE-constrained optimization problem, where the objective is to minimize a misfit functional that quantifies the discrepancy between simulated and observed data. The optimization is subject to the constraint that the solution must satisfy the governing equations of mantle flow, which are typically non-linear partial differential equations (Hinze et al., 2008). Gradient-based methods are well suited for solving such problems efficiently (Plessix, 2006; Ghelichkhan et al., 2024). For example, in one case considered in this study, the aim is to recover a spatially varying viscosity field μ by minimizing the misfit between predicted and observed surface dynamic topography and surface velocity. Since μ is defined throughout the computational domain, it consists of a large number of unknowns, often of the order of thousands or more. This makes brute-force or derivative-free approaches (e.g., random search or genetic algorithms) impractical. Gradient-based methods, on the other hand, use the local sensitivity information to efficiently explore the parameter space (Martinec et al., 2014; Crawford et al., 2018). Once the gradient of the reduced objective functional $\hat{\mathcal{J}}(\mu)$ is computed, using the adjoint method, the optimization algorithm determines a descent direction to update the viscosity field. These methods converge more rapidly and require fewer forward model evaluations, especially when the objective functional is smooth and the problem is moderately well-posed (Plessix, 2006). In this work, we use a non-linear optimization algorithm given by Lin and Moré (1999) to iteratively update μ and minimize the misfit functional. The gradient is computed using the *adjoint method* (Ghelichkhan and Bunge, 2016; Horbach et al., 2014),

which allows for efficient evaluation of the gradient with respect to a large number of control parameters. Importantly, the computational cost of the adjoint method is independent of the number of control parameters. We adopt a reduced functional formulation, where viscosity is treated as the independent variable and all other state variables (e.g., velocity, pressure, temperature) are implicitly dependent on it through the governing equations (Ghelichkhan et al., 2024).

In the sections that follow, we define the objective functional, derive its gradient using the adjoint method, formulate the sensitivity equations, verify the computed gradients, and perform non-linear optimization to solve the inverse problem. While this theoretical discussion focuses on using viscosity μ as the control parameter, the numerical inversion framework itself is general. Depending on the specific physical property of interest, the same methodology can be applied to other controls such as temperature, activation energy, or boundary conditions. The key requirement is that the chosen control must influence the forward model and therefore affect the misfit between model predictions and observations. Once this dependency is established, the objective functional and its gradient can be redefined accordingly within the same inversion setup.

3.1 Calculation of Objective functional

To estimate mantle properties, we pose the inversion as an optimization problem (Ghelichkhan et al., 2024). The goal is to adjust a spatially varying field, such as viscosity, so that the model predictions of dynamic topography and surface velocity at the surface match observed data as closely as possible. To ensure that the recovered solution is physically realistic and numerically stable, we incorporate regularization terms that penalize unrealistic variations and promote smoothness (Fichtner, 2010). We define the objective functional as the sum of four components:

- 1. Dynamic Topography Misfit:** This term quantifies the squared difference between the modelled and observed dynamic topography:

$$\text{DT}_{\text{misfit}} = \frac{N_{\text{dt}}}{N_{\text{obs}}} \int \Gamma_t (h_{\text{dyn}} - h_{\text{obs}})^2 ds \quad (3.1)$$

where dynamic topography h_{dyn} is calculated from the boundary normal stress as shown

in Eq. (2.22). It reflects how well the model reproduces observed surface deflections driven by mantle flow.

2. Surface Velocity Misfit: This term captures the misfit in horizontal surface velocity:

$$u_{\text{misfit}} = \frac{N_{\text{dt}}}{N_u} \int_{\Gamma_t} (\mathbf{u}_{\text{surf}} - \mathbf{u}_{\text{obs}})^2 ds \quad (3.2)$$

where the surface velocity is calculated as shown in Eq. (2.25). It helps constrain the flow field near the surface and complements the dynamic topography misfit.

3. Smoothing Term: This regularization term penalizes high spatial gradients in the viscosity field:

$$\text{Smoothing} = \frac{N_{\text{dt}}}{N_s} \int_{\Omega} |\nabla(\mu - \mu_{\text{avg}})|^2 dx \quad (3.3)$$

4. Damping Term: This term penalizes large deviations from a prior viscosity estimate:

$$\text{Damping} = \frac{N_{\text{dt}}}{N_d} \int_{\Omega} (\mu - \mu_{\text{avg}})^2 dx \quad (3.4)$$

The complete objective functional is then expressed as:

$$\begin{aligned} \mathcal{J}(\mu, \mathbf{u}, p, T, h_{\text{dyn}}) = & \alpha_{\text{dt}} \cdot \text{DT}_{\text{misfit}}(h_{\text{dyn}}, h_{\text{obs}}) \\ & + \alpha_u \cdot u_{\text{misfit}}(\mathbf{u}_{\text{surf}}, \mathbf{u}_{\text{obs}}) \\ & + \alpha_s \cdot \text{Smoothing}(\mu, \mu_{\text{avg}}) \\ & + \alpha_d \cdot \text{Damping}(\mu, \mu_{\text{avg}}) \end{aligned} \quad (3.5)$$

where the user-defined weights control the relative importance of each term.

3.1.1 Regularization Terms

Inverse problems in geophysics are typically ill-posed, meaning that small perturbations in the input data can result in large variations in the recovered solution. Moreover, the data available to

Table 3.1: Symbols used in the misfit and objective functional calculation. (Eqs (3.1)-(3.7))

Symbol	Description
μ	Viscosity (control parameter)
μ_{avg}	Reference or average viscosity field
\mathbf{u}, p, T	Velocity, pressure, and temperature fields
\mathbf{u}_{surf}	Surface velocity
\mathbf{u}_{obs}	Observed surface velocity
h_{dyn}	Dynamic topography computed from forward model
h_{obs}	Observed dynamic topography
Ω	Computational domain
Γ_t	Top boundary of the domain
\mathcal{J}	Full objective functional (depends on control and state)
$\hat{\mathcal{J}}(\mu)$	Reduced objective functional (depends only on control (μ))
$\mathcal{F}(\mu, \mathbf{u}, p, T)$	Forward Model (Stokes and energy equations)
$\alpha_{\text{dt}}, \alpha_u, \alpha_s, \alpha_d$	Weighting coefficients for misfit and regularization terms
$\text{DT}_{\text{misfit}}$	Dynamic topography misfit term
u_{misfit}	Surface velocity misfit term
Smoothing	Regularization term penalizing high gradients
Damping	Regularization term penalizing deviation from average viscosity
$N_{\text{dt}}, N_u, N_d, N_s$	Normalization constants for each misfit or regularization term

constrain mantle properties, such as dynamic topography, are often sparse and indirect, leading to non-uniqueness and instability in the inversion. To mitigate these issues, regularization terms are incorporated into the objective functional (Tikhonov, 1963; Fichtner, 2010). The damping term penalizes large deviations from a reference viscosity field μ_{avg} , typically selected based on prior physical knowledge or initial estimates. This constrains the solution to remain within a physically plausible range and reduces sensitivity to noise or limited data. The smoothing term penalizes sharp spatial gradients in the viscosity field, promoting solutions that are both geologically plausible and numerically stable. Together, these regularization terms stabilize the inversion, promote meaningful structures in the solution, and balance data fidelity with model complexity. The weights α_d and α_s control the influence of the damping and smoothing terms, respectively, and are critical in managing the trade-off between fitting the data and

enforcing prior assumptions. In practice, these parameters are chosen through trial-and-error, cross-validation, or methods such as L-curve analysis (Hansen, 1992). Their role and tuning in this study are discussed in Chapter 4.

3.1.2 Normalization Terms

To ensure that the objective functional is scale-independent, we normalize the velocity, damping, and smoothing terms with respect to the dynamic topography term using appropriate norms:

$$\begin{aligned} N_{dt} &:= \int_{\Gamma_t} h_{obs}^2 ds \\ N_u &:= \int_{\Gamma_t} |\mathbf{u}_{obs}|^2 ds \\ N_d &:= \int_{\Omega} \mu_{avg}^2 dx \\ N_s &:= \int_{\Omega} |\nabla h_{obs}|^2 dx \end{aligned}$$

These terms help ensure that the misfit and regularization components are weighted fairly relative to the scale of the input data.

3.1.3 Defining a reduced functional

The objective functional defined Eq. (3.5) depends not only on the control parameter μ (viscosity), but also on the model outputs: velocity \mathbf{u} , pressure p , temperature T , and dynamic topography h_{dyn} . All of these fields are determined by solving the Stokes and energy equations for a given viscosity distribution as described in Section 2.4.3. Therefore, they are not independent variables. The complete objective functional can be written as $\mathcal{J}(\mu, \mathbf{u}, p, T, h_{dyn})$ where the state variables \mathbf{u}, p, T depend implicitly on μ .

To simplify our optimization problem, we define a reduced version of the functional by substituting the solution of the forward problem into \mathcal{J} (see Ghelichkhan et al. (2024) for more details). This gives the reduced functional:

$$\hat{\mathcal{J}}(\mu) = \mathcal{J}(\mu, \mathbf{u}(\mu), p(\mu), T(\mu), h_{dyn}(\mu)) \quad (3.6)$$

which depends only on the control parameter μ .

In this form, the optimization problem becomes:

$$\min_{\mu} \mathcal{J}(\mu, \mathbf{u}, p, T) \quad \text{subject to: } \mathcal{F}(\mu, \mathbf{u}, p, T) = 0 \quad (3.7)$$

Here, $\mathcal{F}(\mu, \mathbf{u}, p, T) = 0$ represents the forward model, which includes the mass conservation equation (2.1), momentum conservation equation (2.2), and energy conservation equation (2.3). These equations must be solved for each value of the viscosity field μ to obtain the state variables \mathbf{u}, p, T , which are then used to evaluate the misfit in the objective functional.

The reduced functional $\hat{\mathcal{J}}(\mu)$ plays a central role in making the optimization computationally tractable. By eliminating the explicit dependence on the state variables, it allows the inversion to be posed entirely in terms of the control parameter μ . This reduction lowers the dimensionality of the problem and enables the use of efficient gradient-based optimization methods via adjoint techniques.

3.2 Adjoint-Based Gradient Calculation

To solve the inversion problem efficiently, we compute the gradient of the reduced functional $\hat{\mathcal{J}}(\mu)$ with respect to the control variable μ , representing the spatially varying viscosity field (Plessix, 2006). The derivation follows the adjoint methodology outlined by Marchuk (1995), Plessix (2006), and Ghelichkhan et al. (2024). Since the forward model is governed by the Stokes and energy equations, the gradient must capture how variations in μ influence the state variables \mathbf{u}, p, T , and thereby affect the objective functional. The functional is expressed as $\mathcal{J}(z, \mu)$, and the forward problem is formulated as:

$$\mathcal{F}(z, \mu) = 0, \quad (3.8)$$

where $z = \{\mathbf{u}, p, T\}$ denotes the state variables: velocity, pressure, and temperature, obtained by solving the governing equations for a given viscosity field μ . This dependency is non-linear and high-dimensional, making direct computation of gradients impractical in large-scale geodynamical models. To overcome this, we use the adjoint method. The adjoint method

provides an efficient way to compute the gradient of the reduced functional with respect to the control, regardless of the number of control parameters (Giles and Pierce, 2000; Gunzburger, 2000). In geodynamical problems, where the control (e.g., viscosity) is a spatial field with thousands of degrees of freedom, traditional finite-difference or direct sensitivity methods are not computationally feasible. The adjoint method avoids this by solving one additional PDE (the adjoint problem), from which the full gradient can be extracted at a computational cost similar to one forward solve. This makes gradient-based inversion in high-dimensional settings both tractable and scalable (Plessix, 2006).

Table 3.2: List of Symbols used in the adjoint-based gradient calculation section (Eqs (3.9)-(3.24)).

Symbol	Description	Symbol	Description
μ	Viscosity (control)	$\hat{\mathcal{J}}$	Reduced objective functional
\mathcal{J}	Full objective functional	\mathcal{F}	Forward PDE system
z	State variables (\mathbf{u}, p, T)	λ	Adjoint variable
\mathbf{u}	Velocity field	p	Pressure field
T	Temperature field	\mathcal{L}	Lagrangian (objective + constraints)
F_h	Discrete forward system	J_h	Discrete objective functional
z_h	Discretized state variables	\hat{J}_h	Reduced discrete functional
$K(\mathbf{x})$	Sensitivity kernel at location \mathbf{x}		

3.2.1 Gradient Calculation

As defined in Section 3.1.3, the reduced functional is given by:

$$\hat{\mathcal{J}}(\mu) = \mathcal{J}(z(\mu), \mu) \quad (3.9)$$

where $z = \{\mathbf{u}, p, T\}$ denotes the state variables that depend implicitly on the control parameter μ .

Using the chain rule, the total derivative of the reduced functional with respect to μ is:

$$\frac{d\hat{\mathcal{J}}}{d\mu} = \frac{\partial \mathcal{J}}{\partial \mu} + \frac{\partial \mathcal{J}}{\partial z} \cdot \frac{\partial z}{\partial \mu}. \quad (3.10)$$

Direct computation of $\partial z / \partial \mu$ is computationally infeasible due to the large number of degrees of freedom in μ . Instead, we introduce a Lagrangian to incorporate the PDE constraints into the optimization problem:

$$\mathcal{L}(z, \mu, \lambda) = \mathcal{J}(z, \mu) + \langle \lambda, \mathcal{F}(z, \mu) \rangle, \quad (3.11)$$

where λ denotes the adjoint variable. The adjoint variable is chosen such that the variation of the Lagrangian with respect to the state variables vanishes:

$$\left(\frac{\partial \mathcal{F}}{\partial z} \right)^T \lambda = \frac{\partial \mathcal{J}}{\partial z}. \quad (3.12)$$

Solving the above adjoint equation allows us to eliminate the need for computing $\partial z / \partial \mu$. The gradient of the reduced functional is then expressed as:

$$\frac{d \hat{\mathcal{J}}}{d \mu} = \frac{\partial \mathcal{J}}{\partial \mu} - \lambda^T \frac{\partial \mathcal{F}}{\partial \mu}. \quad (3.13)$$

The first term captures the explicit dependence of \mathcal{J} on μ , while the second accounts for the implicit dependence through the state variables. This adjoint-based formulation significantly reduces computational cost, especially in high-dimensional control spaces.

3.2.2 Continuous vs Discrete Adjoint

There are two primary approaches to derive the adjoint equations (Gunzburger, 2000, 2002):

1. **Continuous adjoint (differentiate-then-discretize):** The adjoint equations are derived from the continuous form of the PDEs:

$$\mathcal{F}(z, \mu) = 0, \quad \text{with } z = \{T, \mathbf{u}, p\}, \quad (3.14)$$

$$\mathcal{J}(z, \mu) = \int_{\Omega} \mathcal{L}(z, \mu) dx. \quad (3.15)$$

The Lagrangian is constructed as:

$$\mathcal{L}_{\text{total}} = \mathcal{J}(z, \mu) + \langle \lambda, \mathcal{F}(z, \mu) \rangle, \quad (3.16)$$

and the adjoint equations are obtained by requiring the variation of the Lagrangian with respect to the state variables to vanish:

$$\frac{\delta \mathcal{L}_{\text{total}}}{\delta z} = 0. \quad (3.17)$$

This approach provides insight into the structure of the adjoint system and the associated sensitivity kernels, and offers flexibility in discretization (Ismail-Zadeh et al., 2004). However, discrepancies between the discretizations of the forward and adjoint problems can lead to inconsistencies in the computed gradients.

2. **Discrete adjoint (discretize-then-differentiate):** Here, the forward model is discretized first:

$$F_h(z_h, \mu) = 0, \quad (3.18)$$

with the discrete objective:

$$J_h(z_h, \mu) = \sum_i \mathcal{L}_h(z_h^i, \mu). \quad (3.19)$$

The reduced functional is given by:

$$\hat{J}_h(\mu) = J_h(z_h(\mu), \mu), \quad (3.20)$$

and its total derivative is:

$$\frac{d\hat{J}_h}{d\mu} = \frac{\partial J_h}{\partial \mu} + \frac{\partial J_h}{\partial z_h} \cdot \frac{\partial z_h}{\partial \mu}. \quad (3.21)$$

Introducing a discrete adjoint variable λ , which satisfies:

$$\left(\frac{\partial F_h}{\partial z_h} \right)^T \lambda = \frac{\partial J_h}{\partial z_h}, \quad (3.22)$$

yields the final gradient expression:

$$\frac{d\hat{J}_h}{d\mu} = \frac{\partial J_h}{\partial \mu} - \lambda^T \frac{\partial F_h}{\partial \mu}. \quad (3.23)$$

This formulation ensures consistency between the forward and adjoint discretizations and yields exact gradients of the discrete objective functional (Giering and Kaminski, 1998). It also simplifies debugging and supports the use of automatic differentiation tools (Gunzburger, 2002). In this study, we adopt the discrete adjoint approach, which is particularly well suited for large-scale PDE-constrained optimization and is implemented using automated frameworks (Tijskens et al., 2002).

3.2.3 Sensitivity Kernel

The gradient of the reduced objective functional with respect to the control variable μ defines the *sensitivity kernel*, which quantifies how the misfit responds to local perturbations in viscosity (Al-Attar and Tromp, 2013). Mathematically, this is written as:

$$K(\mathbf{x}) := \frac{\delta \hat{\mathcal{J}}}{\delta \mu}(\mathbf{x}), \quad (3.24)$$

where $K(\mathbf{x})$ denotes the sensitivity kernel at location \mathbf{x} in the domain. This function captures the point-wise contribution to the gradient and guides the optimization process.

In our case, the kernel includes contributions from both dynamic topography and surface velocity misfit terms. High values of the kernel indicate regions where changes in viscosity strongly influence surface observables. For instance, regions with high sensitivity to dynamic topography suggest that variations in viscosity there significantly affect modeled topography. Similarly, velocity sensitivity highlights areas where surface velocities are most responsive to rheological changes. These fields not only inform the inversion but also provide physical insight into the connection between deep mantle structure and surface expressions. The interpretation

of these kernels is discussed in Chapter 4, where we visualize and analyze their spatial distribution.

The term $\frac{\partial \hat{\mathcal{J}}}{\partial \mu}$ reflects the explicit dependence of the objective on the control, while the term involving λ captures the implicit dependence via the PDE constraints. In practice, the discrete adjoint equations are generated automatically using symbolic differentiation within the numerical framework (Ghelichkhan et al., 2024). The resulting gradient is passed to a nonlinear optimization algorithm (e.g., Lin-More) to iteratively update the viscosity field and minimize the objective functional.

3.3 Gradient Verification

To verify the correctness of the computed gradients, we perform the *Taylor remainder convergence test* (Farrell et al., 2013; Ghelichkhan et al., 2024). This test evaluates whether the gradient accurately predicts the first-order change in the objective when the control parameter μ is perturbed.

Let $\delta\mu$ be a perturbation in the control space, and α a scalar step size. The Taylor expansion of the reduced functional evaluated at $\mu + \alpha\delta\mu$ is:

$$\hat{\mathcal{J}}(\mu + \alpha\delta\mu) = \hat{\mathcal{J}}(\mu) + \alpha \langle \nabla \hat{\mathcal{J}}, \delta\mu \rangle + \mathcal{O}(\alpha^2), \quad (3.25)$$

where:

- $\nabla \hat{\mathcal{J}}$ is the computed gradient,
- $\langle \nabla \hat{\mathcal{J}}, \delta\mu \rangle$ is the directional derivative,
- $\mathcal{O}(\alpha^2)$ denotes the second-order term in the expansion.

The Taylor remainder is given by:

$$R(\alpha) = \frac{\hat{\mathcal{J}}(\mu + \alpha\delta\mu) - \hat{\mathcal{J}}(\mu) - \alpha \langle \nabla \hat{\mathcal{J}}, \delta\mu \rangle}{\alpha^2}. \quad (3.26)$$

A correctly computed gradient yields $R(\alpha) \rightarrow \text{const}$ as $\alpha \rightarrow 0$, indicating second-order con-

vergence. We perform this test by applying random perturbations to μ , reducing the perturbation magnitude (e.g., by factors of $1/2, 1/4, 1/8$), and monitoring the convergence of $R(\alpha)$. A convergence rate of $\mathcal{O}(\alpha^2)$ corresponds to a slope of approximately 2.0 on a log-log plot, confirming the gradient's correctness.

3.4 Gradient-based Optimization

The inversion process is formulated as a PDE-constrained optimization problem, where the objective is to minimize the misfit between the model predictions and observations by adjusting the control parameter, in our case, the spatially varying viscosity field μ . This process is schematically illustrated in Figure 3.1, and consists of the following iterative steps:

1. Begin with an initial guess of the control parameter μ , along with observed data (dynamic topography and surface velocity).
2. Solve the forward problem to obtain the state variables \mathbf{u}, p, T .
3. Evaluate the objective functional $\hat{\mathcal{J}}(\mu)$.
4. Compute the gradient $\frac{d\hat{\mathcal{J}}}{d\mu}$ using the adjoint method.
5. Update the viscosity field based on this gradient.
6. Repeat the process until the objective functional is sufficiently small.

The optimization problem was discussed earlier in Section 3.1.3, and is given by:

$$\min_{\mu} \hat{\mathcal{J}}(\mu), \quad (3.27)$$

where $\hat{\mathcal{J}}(\mu)$ is the reduced objective functional, and μ is subject to bound constraints to ensure physical realism. Gradient-based optimization is particularly well-suited for high-dimensional inverse problems, where the control variable (e.g., viscosity) is defined as a spatial field with many degrees of freedom. These methods use sensitivity information obtained from the adjoint to guide updates to the control. Unlike brute-force or derivative-free approaches, gradient-based algorithms are computationally tractable and scalable (Hinze et al., 2008; Giles and Pierce, 2000; Plessix, 2006).

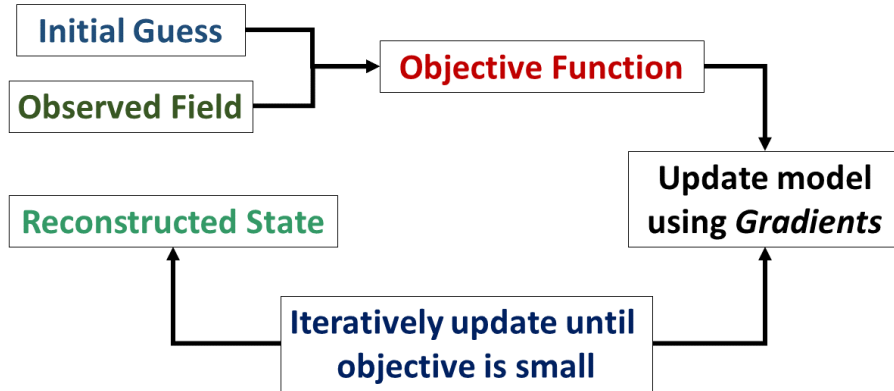


Figure 3.1: Flowchart describing the iterative optimization procedure for inversion.

Two widely used optimization strategies are the *line-search* and *trust-region* methods (Nocedal and Wright, 1999). In line-search methods, a descent direction is computed from the gradient, and a step size is selected along this direction to ensure sufficient decrease in the objective functional. In contrast, trust-region methods define a neighborhood around the current iterate, within which a local model, typically quadratic, is assumed to approximate the objective reliably (Nocedal and Wright, 2006). The optimization step is constrained to lie within this trust region, whose radius is adjusted at each iteration based on the agreement between predicted and actual reductions in the objective. Trust-region strategies are particularly effective for non-linear inverse problems due to their robustness and control over step size. They also naturally incorporate bound constraints, which are often necessary in physical problems such as viscosity inversion. At each iteration, control variables are divided into two sets: the *active set*, comprising variables on their bounds and fixed during the update, and the *inactive set*, which includes variables free to change. This ensures that updates respect the prescribed physical bounds and prevent unstable steps. Furthermore, when the model remains predictive, the trust-region radius can be expanded to accelerate convergence (Conn et al., 2000).

3.4.1 Lin–Moré Optimization Algorithm

In this study, we employ the trust-region method given by Lin and Moré (1999), implemented through the ROL (Rapid Optimization Library) package (Trilinos Team, 2024). This method is a *truncated Newton algorithm*, where the Newton system is solved approximately using iterative

methods (Dixon and Price, 1989). At each iteration, the algorithm solves a subproblem of the form:

$$\min_p \quad m_k(p) = \frac{1}{2} p^T B_k p + g_k^T p \quad \text{subject to } \|p\| \leq \Delta_k, \quad (3.28)$$

where g_k is the gradient of the objective functional at iteration k , B_k is an approximation of the Hessian, and Δ_k is the trust-region radius. The step p_k is accepted if it produces sufficient reduction in the actual objective. Otherwise, the trust-region is contracted to ensure the validity of the local approximation.

Standard optimization libraries often assume a Euclidean (sequence-space) inner product, which is not appropriate for function-based optimization over finite-element spaces (Schwedes et al., 2017). To ensure mesh-independent convergence, we use an L^2 inner product (Ghelichkhan et al., 2024). The ROL framework allows custom inner products, making it suitable for large-scale PDE-constrained optimization problems in finite-element settings.

This chapter introduced the theoretical framework for adjoint-based geodynamic inversion, outlining the objective functional, sensitivity analysis, and optimization formulation. The application of this framework to specific numerical configurations is detailed in the following chapters.

Chapter 4

Numerical Implementation and Results: Inversion Using Field-Based Controls

This chapter and the next present the numerical implementation of the forward and inverse frameworks developed in the previous two chapters. This chapter focuses on field based control parameters, specifically viscosity and temperature, and investigates their recoverability from synthetic observations of dynamic topography and surface velocity. We describe the computational setup, softwares used, mesh generation, solver configuration, and boundary condition specification. The chapter also details a suite of synthetic inversion analyses aimed at investigating the recovery of mantle properties from surface observations. These studies are designed to test different aspects of the inversion process, including sensitivity to data, regularization strategies, and the robustness of optimization. Selected code snippets and intermediate results are presented throughout this chapter, along with a complete analysis of the inversion outcomes.

Figure 1.4 illustrates the overall workflow for the series of modeling scenarios explored in this study. We begin by generating synthetic data through a forward time-dependent simulation, from which surface dynamic topography and velocity are extracted as observables. In the inversion setup, we assume no prior knowledge of the true fields (commonly referred to as an *inverse crime*) and instead define a synthetic twin with a perturbed initial guess (Ghelichkhan et al., 2024; Davies et al., 2022). The misfit between the simulated and observed fields is quantified through an objective functional, which is minimized using gradients obtained via the adjoint method. The validity of gradients is verified using Taylor remainder tests. Finally, the viscosity field is updated using a gradient-based non-linear optimization algorithm until convergence, and the reconstructed fields are compared against the synthetic observables. To explore the sensitivity and robustness of the inversion process, we design and implement a sequence of modeling scenarios with increasing complexity. These include:



Figure 4.1: Core software libraries used for this study.

- Inversion for viscosity as a direct control parameter,
- Inversion for temperature as the control parameter,
- Inversion for activation energy, given a known temperature field,
- Inversion for activation energy, given its depth dependence,
- Inversion for activation energy, using fully complex mantle rheology.

These cases assess the influence of control variables, the role of regularization, and the interplay between surface data and internal rheology. Intermediate outputs and visualizations are presented to support interpretation. The first two configurations are discussed in this chapter, while the subsequent three involving activation energy are presented in Chapter 5.

4.1 Software Framework

The numerical implementation developed in this study is built upon the **Geoscientific Adjoint Optimization Platform (G-ADOPT)** (Gibson et al., 2024), an extensible and automated framework for large-scale PDE-constrained inversion problems in geodynamics. A visual summary of the software framework is shown in Figure 4.1. G-ADOPT integrates three core libraries that work together to support high-performance forward and adjoint modeling (Ghelichkhan et al., 2024):

- **Firedrake** (Ham et al., 2023; Rathgeber et al., 2016) is an automated finite element system for solving partial differential equations. It employs the Unified Form Language (UFL) (Alnæs et al., 2014) for the symbolic specification of variational problems, enabling a close match between mathematical formulations and code. Firedrake supports a wide range of discretisations and is particularly suited for geophysical applications as shown by Davies et al. (2022) due to its efficient handling of structured and extruded meshes, various solvers, and parallel solving capabilities via PETSc (Balay et al., 2025).
- **Dolfin-Adjoint** (Mitusch et al., 2019) provides automatic differentiation capabilities by performing operator overloading within the high-level UFL representation. It tracks computational operations using a Tape structure, which records the sequence of forward operations, such as solves and interpolations which are required to compute the objective functional. This recorded tape is then used to derive the discrete adjoint equations and construct a Reduced Functional, enabling efficient and exact gradient computation with respect to control variables.
- **Rapid Optimization Library (ROL)** (Trilinos Team, 2024) is a Trilinos package for large-scale constrained optimization. ROL includes a wide range of gradient-based algorithms, including trust-region and Newton-type methods, and is particularly suited for high-performance computing environments. One of its key features is built-in support for checkpointing, which allows the optimization process to be paused and resumed without loss of progress.

These libraries are interfaced and controlled using Python, which serves as the primary scripting language for development of the inversion workflow. Visualization of model outputs, sensitivities, and inversion results is performed using ParaView (Ayachit, 2015) and the PyVista (Sullivan and Kaszynski, 2019) Python library. G-ADOPT supports output via the Visualization Toolkit (VTK), enabling seamless integration with these scientific visualization tools. The combined software stack allows for consistent and efficient forward–adjoint workflows tailored for mantle convection inversion problems. By using symbolic differentiation and a high-level abstraction of PDEs, G-ADOPT ensures that adjoint calculations remain accurate and robust, even in complex non-linear and high-dimensional settings. The framework accommodates a broad range of rheologies, boundary conditions, mesh configurations, and solver options, making it well-suited for modern geodynamical modeling tasks.

4.2 Model Configuration 1: Inversion Using Viscosity as the Control Parameter

In this section, we present our first numerical experiment, in which we aim to recover a spatially varying viscosity field from observations of surface dynamic topography and surface velocity. This setup corresponds directly to the inverse problem described in Chapter 3, where viscosity is treated as the control parameter. At this stage of model development, our aim was to understand how the inverse model responds to different observable constraints. To keep the analysis simple and interpretable, we excluded the non-linear and depth-dependent components of the viscosity formulation. This allowed us to avoid potential discontinuities and sharp gradients in the control field, which can complicate the interpretation of adjoint sensitivities. Instead, we considered only the temperature dependence of viscosity, resulting in a smoother rheological profile. The viscosity field used in this experiment is a truncated form of the full rheology described in Section 2.2, and is defined as:

$$\mu_{\text{lin}}(T, z) = \exp(-E_a T) \quad (4.1)$$

where E_a is the activation energy that governs the exponential dependence of viscosity on temperature.

4.2.1 Synthetic Data Generation

To generate synthetic dynamic topography datasets for inversion, we simulate the evolution of four mantle plumes in a two-dimensional annular domain (Ghelichkhan et al., 2024). The annulus is bounded between radii $r_{\min} = 1.22$ and $r_{\max} = 2.22$, establishing a non-dimensional mantle thickness of $z = r_{\max} - r_{\min} = 1$ and a radius ratio $f = r_{\min}/r_{\max} = 0.55$, approximating Earth's surface-to-core-mantle boundary ratio.

Listing 1 shows selected lines of the script used to generate this reference initial condition. In lines 1–4, the necessary dependencies are imported and the geometric parameters for the annular domain are defined. A circular one-dimensional manifold mesh is created at radius r_{\min} (Line 3) and is radially extruded to form the two-dimensional annular mesh (Line 4). The

```

1 from gadopt import * #import all the required dependencies (Gadopt, Firedrake)
2 rmin, rmax, ncells, nlayers = 1.22, 2.22, 256, 64 #set up the 2-D annular geometry
3 meshid = CircleManifoldMesh(ncells, radius=rmin, degree=2) # construct a circle mesh
4 mesh = ExtrudedMesh(meshid, layers=nlayers, extrusion_type='radial') # extrude into a cylinder
5 bottom_id, top_id = "bottom", "top"
6
7 #set up function spaces Q2Q1 pair for velocity and pressure and Q2 fot temperature
8 V = VectorFunctionSpace(mesh, "CG", 2) # Velocity function space (vector)
9 W = FunctionSpace(mesh, "CG", 1) # Pressure function space (scalar)
10 Q = FunctionSpace(mesh, "CG", 2) # Temperature function space (scalar)
11 Z = MixedFunctionSpace([V, W]) # Mixed function space for Stokes solving
12
13 z = Function(Z) # A field over the mixed function space Z.
14 u, p = split(z) # Returns symbolic UFL expression for u and p
15
16 # We next specify the important constants for this problem, and set up the approximation.
17 Ra = Constant(5e4) # Rayleigh number
18 approximation = BoussinesqApproximation(Ra) #incompressibility
19 delta_t = Constant(1e-7) # Initial time-step
20 timesteps = 20000 # Maximum number of timesteps for the time-loop
21
22 # We choose the initial temperature distribution to trigger upwelling of 4 equidistant plumes.
23 X = SpatialCoordinate(mesh)
24 r = sqrt(X[0]**2 + X[1]**2)
25 T = Function(Q, name="Temperature").interpolate(rmax - r + 0.02*cos(4*atan2(X[1], X[0])) * sin((r - rmin) * pi))
26
27 mu = exp(-ln(100) * T) # evaluate the viscosity, which depends on temperature
28
29 # null spaces to handle non-physical solutions
30 Z_nullspace = create_stokes_nullspace(Z, closed=True, rotational=True)
31 Z_near_nullspace = create_stokes_nullspace(Z, closed=False, rotational=True, translations=[0, 1])
32
33 # boundary conditions and setting up the solvers
34 stokes_bcs = { bottom_id: {'un': 0}, top_id: {'un': 0},}
35 temp_bcs = { bottom_id: {'T': 1.0}, top_id: {'T': 0.0},}
36 energy_solver = EnergySolver(T, u, approximation, delta_t, ImplicitMidpoint, bcs=temp_bcs)
37 stokes_solver = StokesSolver(z, T, approximation, bcs=stokes_bcs, mu=mu, nullspace=Z_nullspace,
    ↳ transpose_nullspace=Z_nullspace, near_nullspace=Z_near_nullspace)
38 surface_force_solver = BoundaryNormalStressSolver(stokes_solver, top_id) #solver for surface stress
39
40 #timeloop to solve the energy equations
41 for timestep in range(0, timesteps):
42     mu_field.interpolate(mu) # Interpolate the viscosity
43     stokes_solver.solve() #solving stokes
44     energy_solver.solve() #solving energy
45     surface_force = surface_force_solver.solve() #calculating the surface force
46     dtopo.interpolate((surface_force / deltarho_g)) #determine the dynamic topography
47
48 #save the states for inversion problem in checkpoint file
49 with CheckpointFile("Final_State.h5", "w") as final_checkpoint:
50     final_checkpoint.save_mesh(mesh)
51     final_checkpoint.save_function([T, name="Temperature"], [z, name="Stokes"], [u, name = "Observed Velocity"],
    ↳ [dtopo, name="Observed DT"], [mu_field, name="Observed Viscosity"] )

```

Listing 1: Synthetic data generation using a time-dependent mantle simulation.

boundary identifiers for the bottom and top surfaces are assigned in Line 5. Lines 7–11 set up the finite element function spaces which were discussed in Section 2.3, within which our solutions are defined. Specifically, a vector function space V is specified for the velocity field (Line 8), employing a continuous Galerkin Q_2 discretization. A scalar function space W is defined for the pressure field (Line 9), utilizing a continuous Galerkin Q_1 discretization. These two spaces are combined on Line 11 to form the mixed function space Z , which is used to solve the coupled Stokes system for velocity and pressure. A scalar function space Q for the temperature field is separately defined in Line 10, also using a Q_2 discretization. Subsequently, a mixed field z is initialized on the space Z , and the velocity and pressure components are

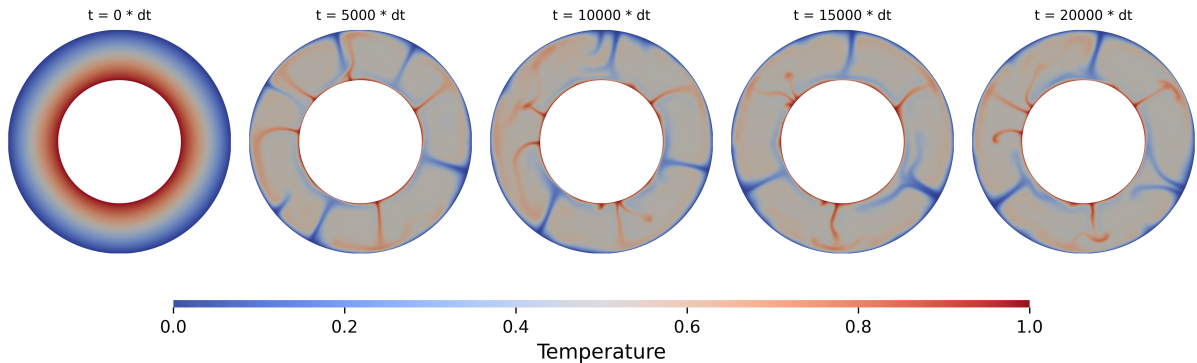


Figure 4.2: The reference twin for the temperature field is generated by evolving the system from an initial condition that triggers the development of four mantle plumes. At time $t = 20,000 \times \Delta t$, the simulation reaches a relatively steady state, indicating that it has run for a sufficiently long duration. This final state is considered representative of present-day mantle conditions and is subsequently used as T_{obs} in the adjoint-based inversion.

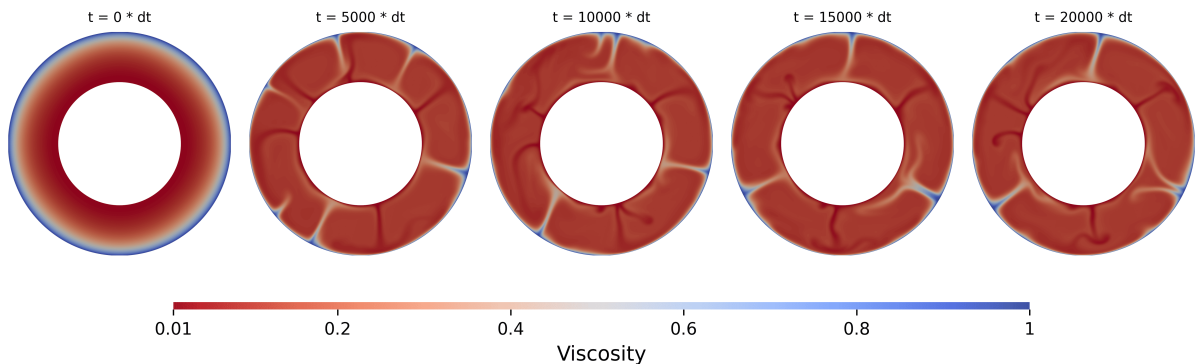


Figure 4.3: Steady-state viscosity field corresponding to Figure 4.2, with low-viscosity regions aligned with mantle plumes. This field is stored as μ_{obs} .

accessed via symbolic splitting in Line 14. In Lines 17–20, important physical constants are defined, including the Rayleigh number $Ra = 5 \times 10^4$ and the timestep size $\Delta t = 10^{-7}$. We have taken a lower Rayleigh number to reduce the computational cost. Flow is assumed to be incompressible under the Boussinesq approximation.

Lines 20–24 prescribe the initial temperature field. The spatial coordinates are defined and the radial distance r is calculated. The temperature field is initialized with a gaussian perturbation designed to trigger four plume upwellings (see Figure 4.2 at $t=0$), using the relation:

$$T_0(r, \theta) = r_{\max} - r + 0.02 \cos(4\theta) \sin(\pi(r - r_{\min})), \quad (4.2)$$

where θ is the azimuthal coordinate given by $\arctan\left(\frac{y}{x}\right)$ (Davies et al., 2022). The evolution

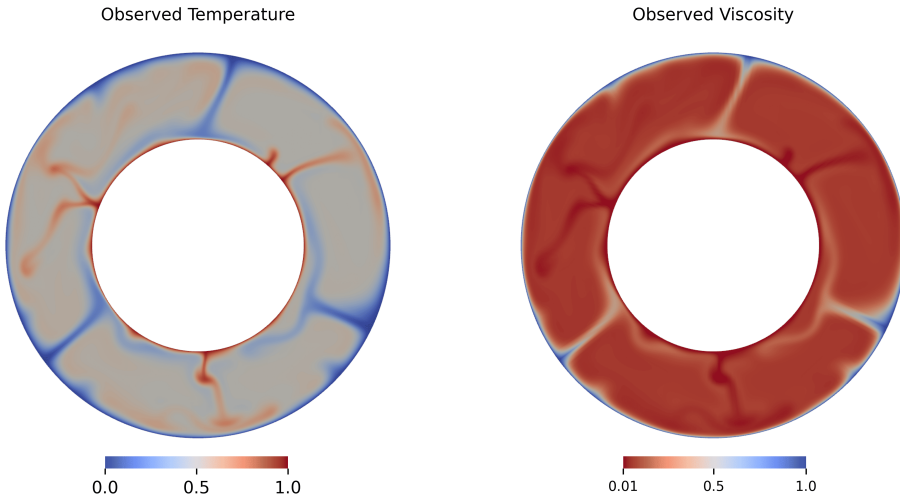


Figure 4.4: Steady-state temperature and viscosity fields used as observed data for the inversion.

of temperature and viscosity fields over the course of the simulation is shown in Figures 4.2 and 4.3, respectively. In Line 27, the viscosity is defined as a temperature-dependent field using the previously described simplified Arrhenius relation in Eq. (4.1), with activation energy $E_a = \ln(100)$ (Turcotte and Schubert, 2002). The nullspaces necessary for the Stokes system are defined in lines 30–31 to correctly handle the pressure indeterminacy and rotational modes. Free-slip boundary conditions for velocity (zero normal component) are imposed at the top and bottom in Line 34, while Dirichlet boundary conditions fixing the temperature at the top and bottom surfaces are specified in Line 35. The PDE solvers are initialized in Lines 36–38. The `EnergySolver` solves the energy (temperature) equation using the implicit midpoint scheme. The `StokesSolver` solves the momentum equations with the temperature-dependent viscosity. A `BoundaryNormalStressSolver` computes the surface normal stresses needed for dynamic topography calculation.

The time loop, implemented in Lines 40–46, advances the system over 20,000 timesteps. We assume that we reach a relatively steady state after such a long time. At each timestep, the viscosity field is updated based on the current temperature (Line 42), the Stokes system is solved (Line 43), the energy equation is solved (Line 44), the surface force is computed (Line 45), and the dynamic topography is updated by normalizing the surface force with a constant as described in Eq. (2.22) (Line 45). Finally, Lines 49–51 save the important fields: temperature, velocity, dynamic topography, and viscosity, in a checkpoint file. These final steady-state fields, shown in Figures 4.4 and 4.5 serve as the “observed data” for subsequent inversion stages, where the misfits between model predictions and these observed fields will be minimized.

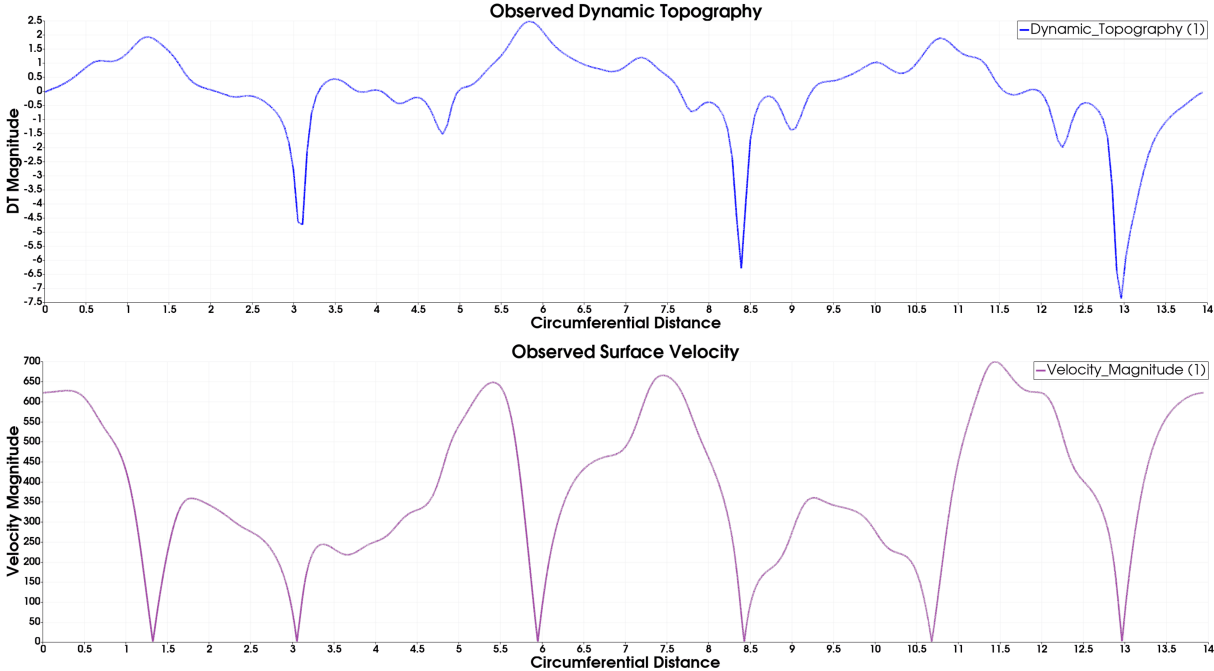


Figure 4.5: Final dynamic topography and surface velocity fields used for misfit evaluation, computed from the steady-state Stokes solution.

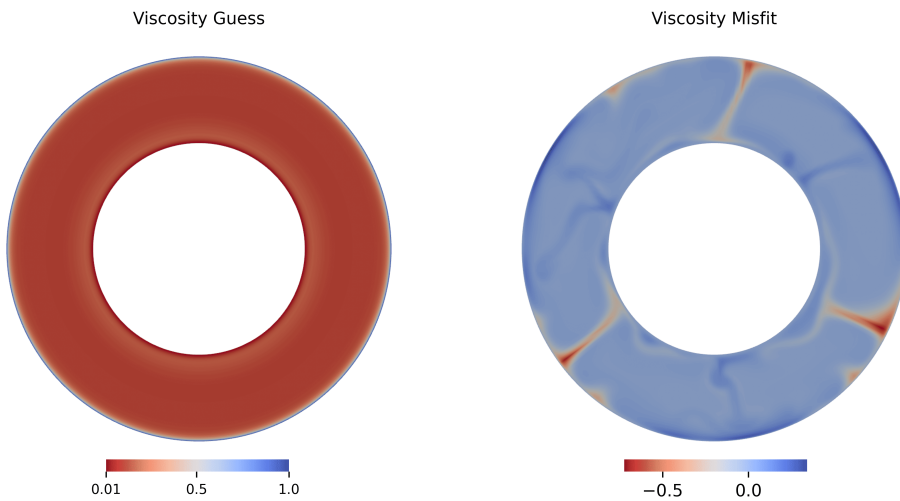


Figure 4.6: The initial guess for the viscosity field is used as the starting point for the inversion process and will be iteratively updated as the inversion progresses. The second figure shows the viscosity misfit, which represents the difference between the observed viscosity field and the initial guessed viscosity field.

4.2.2 Forward Model and Initial Misfit Calculation

To set up the inverse problem, we first load the mesh and previously computed fields from the checkpoint file generated during the forward problem (Listing 2, Lines 3–8). Specifically, we

```

1 from gadopt.inverse import *      #inverse library for adjoints and optimization
2 # Open the checkpoint file and subsequently load the mesh and the necessary fields from the forward problem
3 with CheckpointFile("../forward/Final_State.h5", "r") as forward_check:
4     mesh = forward_check.load_mesh("firedrake_default_extruded")
5     T = forward_check.load_function(mesh, "Temperature")
6     dtopo_obs = forward_check.load_function(mesh, "Observed DT")
7     mu_observed = forward_check.load_function(mesh, "Observed Viscosity")
8     u_obs = forward_check.load_function(mesh, "Observed Velocity")
9     .....
10    u, p = split(z) # Returns symbolic UFL expression for u and p (initial guess)
11
12    # For our inverse study we need to determine the viscosity, mu_control.
13    # We use layer average viscosity as our initial guess for inverse crime.
14    .....
15    mu_average = Function(Q1, name="Average_Viscosity").project(mu_av, bcs=mu_bcs)
16    mu_control = Function(Q1, name="Viscosity_Control").project(mu_average)
17    control = Control(mu_control) #control we give to the reduced functional
18    .....
19    # Now we will solve the Stokes system in order to calculate the guess dynamic topography and velocity from the
20    #→ guess viscosity field.
21    .....
22    # Free-slip boundary conditions for the stokes system
23    stokes_bcs = { bottom_id: {'un': 0}, top_id: {'un': 0} }
24    stokes_solver = StokesSolver(z, T, approximation, bcs=stokes_bcs, mu=mu_control,...nullspace=Z_nullspace) #solve
25    #→ stokes using guess viscosity
26    surface_force_solver = BoundaryNormalStressSolver(stokes_solver, top_id) #for
27    #→ dynamic topography calculation
28    stokes_solver.solve() # Solving the Stokes system
29    surface_force = surface_force_solver.solve() # Calculate the surface force
30    dtopo = Function(W, name="DT").interpolate(surface_force/deltarho_g) # Calculate the guess dynamic topography
31    .....
32    # Calculate the misfits; the difference between model and observation
33    dt_misfit = assemble ((dtopo - dtopo_obs) ** 2 * ds_t) # DT error
34    u_misfit = assemble(dot(u - u_obs, u - u_obs) * ds_t) # velocity error
35    # regularization terms
36    smoothing = assemble(dot(grad(mu0 - mu_average), grad(mu0 - mu_average)) * dx)
37    damping = assemble((mu0 - mu_average) ** 2 * dx)
38    # normalization terms
39    norm_dt = assemble(dtopo_obs**2 * ds_t)
40    norm_u = assemble(dot(u_obs, u_obs) * ds_t)
41    norm_damping = assemble(mu_average**2 * dx)
42    norm_smoothing = assemble(dot(grad(mu0 - mu_average), grad(mu0 - mu_average)) * dx)
43    # Define the component terms of the overall objective functional
44    topography_misfit = (dt_misfit / norm_dt) * norm_dt
45    velocity_misfit = (u_misfit / norm_u) * norm_dt
46    smoother = (smoothing / norm_smoothing) * norm_dt
47    damper = (damping / norm_damping) * norm_dt
48    # relative weights for the terms in the objective function
49    alpha_dt, alpha_u, alpha_s, alpha_d = 1.0, 1.0, 1e-2, 1e-2
50    # equation for the objective function
51    objective = alpha_dt * topography_misfit + alpha_u * velocity_misfit + alpha_s * smoother + alpha_d * damper
52    .....
53    # Using the definition of our objective function we define the reduced functional (Adjoint)
54    reduced_functional = ReducedFunctional(objective, control) # J(mu_control)
55    # Having the reduced functional one can easily compute the gradient sensitivity
56    grad_func = reduced_functional.derivative(options={"riesz_representation": "L2"})
57    VTKFile("gradient-visualisation.pvd").write(grad_func) # Visualising the gradients
58    .....
59    # verifying the gradients using the taylor test
60    Delta_mu.dat.data[:] = np.random.random(Delta_mu.dat.data.shape) * 0.1 #adding minute perturbations
61    minconv = taylor_test(reduced_functional, mu_control, Delta_mu) #perform taylor test

```

Listing 2: Setup of the inversion problem: loading observed fields, defining the initial guess, evaluating the initial forward misfit, defining the reduced functional used in adjoint problem and verifying the gradients.

recover the steady-state temperature field T , the observed dynamic topography $d_{\text{topo,obs}}$, the observed viscosity field μ_{obs} , and the observed surface velocity field u_{obs} (Figures 4.4, 4.5).

An inverse crime is introduced by initializing the inversion with an incorrect viscosity

field. Although the true viscosity structure μ_{obs} is known, we define an initial guess based on the layer-averaged value of the actual viscosity field as shown in Figure 4.6. In Lines 15–17, the average viscosity is projected onto the \mathbb{Q}_1 function space, which is used to define the initial control variable μ_{control} . The control variable for the inversion is then defined using `Control(mu_control)`. Using this initial guess, we solve the Stokes system again (Lines 21–25) by imposing free-slip boundary conditions on the top and bottom surfaces, as before. The `StokesSolver` computes the velocity and pressure fields corresponding to the guessed viscosity, while the `BoundaryNormalStressSolver` calculates the surface normal stresses to evaluate the guess dynamic topography. The model-predicted dynamic topography d_{topo} is computed by normalizing the surface force by the buoyancy contrast (Line 27). With the predicted velocity u and dynamic topography d_{topo} , we evaluate the misfit terms. Lines 29–34 compute the misfit components: the dynamic topography misfit, the surface velocity misfit, and the regularization terms (smoothing and damping). These are normalized appropriately using the observed field norms (Lines 35–44). The specific mathematical expressions for the misfit terms, normalization, and regularization were detailed previously in Section 3.1. The component terms are then combined to construct the overall objective functional in Lines 45–48. Relative weights for dynamic topography and velocity misfits are assigned, and smaller weights are given to the regularization terms. The formulation of the objective functional follows the definition provided in Eq. (3.5).

The resulting initial misfits in dynamic topography and surface velocity, based on the incorrect viscosity guess, are shown in Figure 4.7. These illustrate the starting point of the inversion process, emphasizing the misfit that the inversion seeks to minimize.

4.2.3 Calculation and Verification of Adjoint Gradients

Having defined the objective functional $J(\mu)$ as a weighted combination of the dynamic topography misfit, surface velocity misfit, and regularization terms (Listing 2, Line 48), we proceed to compute its gradient with respect to the control parameter μ_{control} . The reduced functional, described in Section 3.1.3, represents the objective as a function of viscosity, and is defined in Line 51 using `ReducedFunctional(objective, control)`. The adjoint-based gradient of the reduced functional is computed automatically in Line 53 via the `derivative()` functionality of `Gadopt`. This gradient represents the sensitivity of the objective functional to perturbations

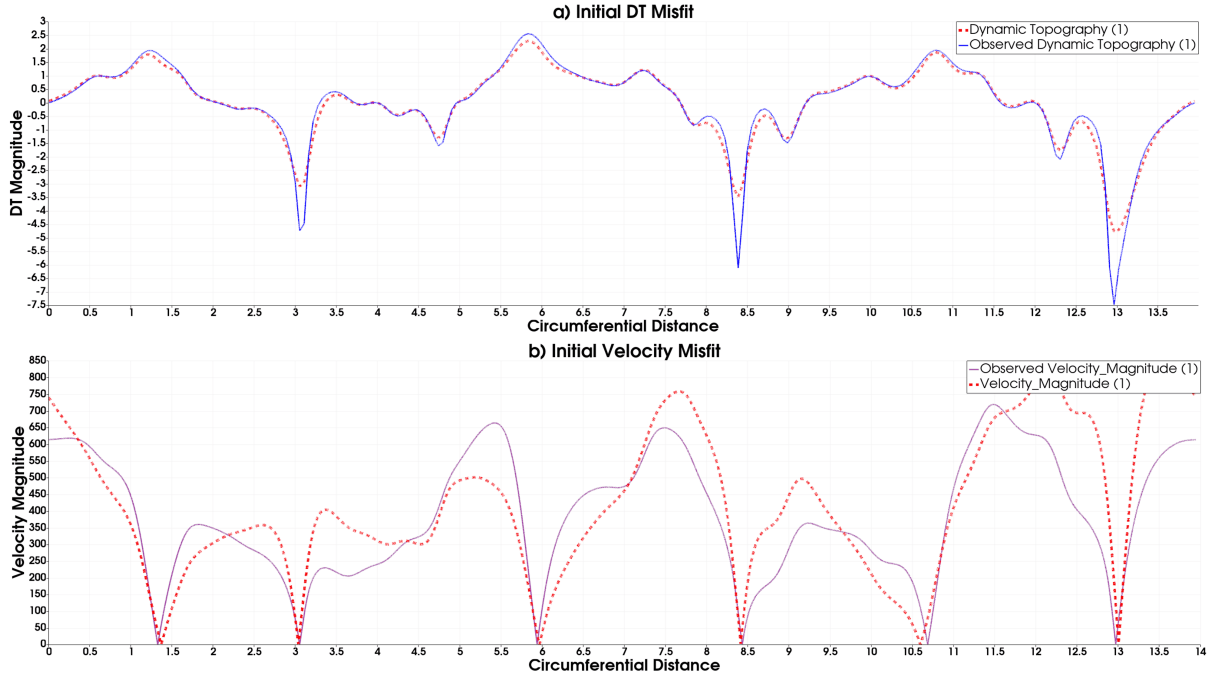


Figure 4.7: Initial misfit between model predictions and observations: (a) dynamic topography misfit. Notably, significant discrepancies are evident in regions of downwellings and upwellings, highlighting the areas where the initial guess deviates most from the observed data. (b) surface velocity misfit, calculated from the initial viscosity guess.

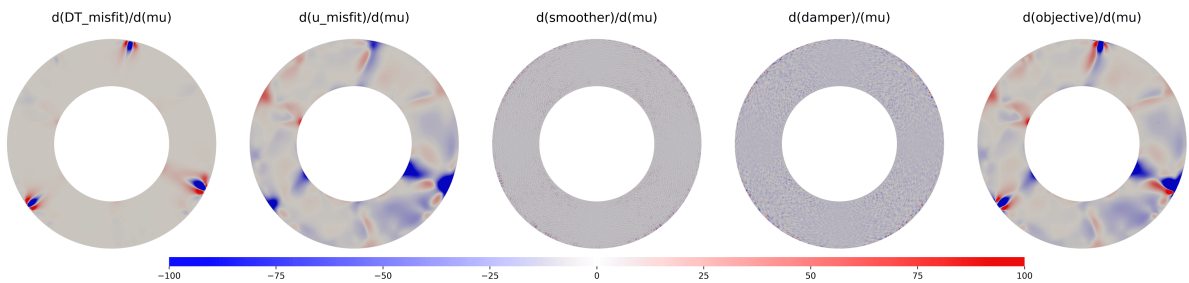


Figure 4.8: Gradients of the objective functional terms with respect to viscosity: (a) dynamic topography misfit gradient, (b) velocity misfit gradient, (c) smoothing regularization gradient, (d) damping regularization gradient, and (e) total objective functional gradient. Red indicates regions where increasing viscosity would reduce the objective, while blue indicates the opposite.

in the viscosity field. Following computation, the gradient field is exported for visualization in Line 54, as shown in Figure 4.8. When combining the individual misfit and regularization terms linearly in the objective functional, the superposition principle dictates that the gradient of the full objective is the cumulative sum of the gradients of its constituent terms (Ghelichkhan et al., 2024). Gradients play a critical role in adjoint-based optimization by providing precise infor-

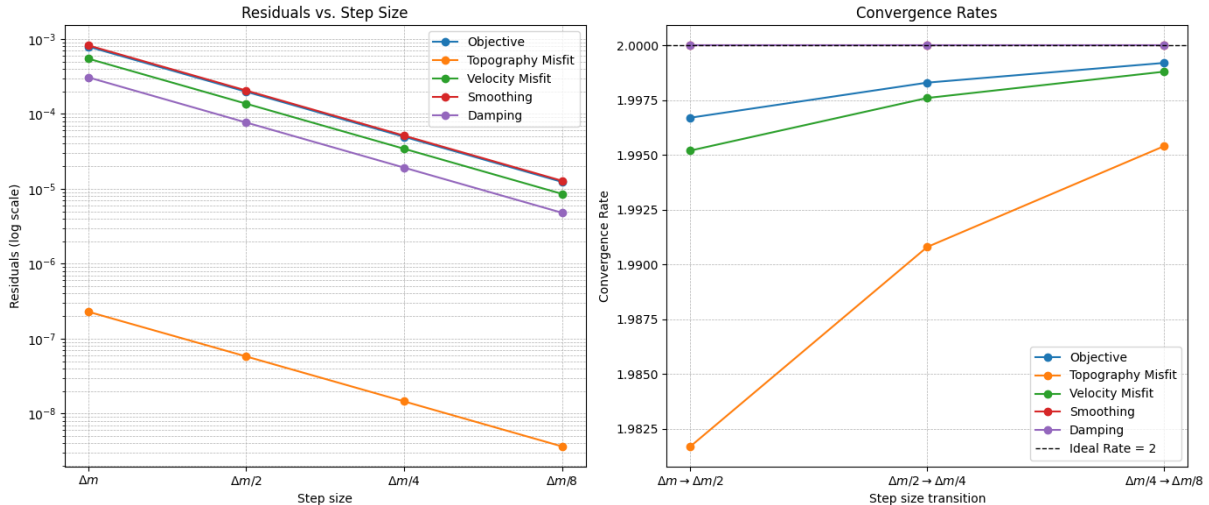


Figure 4.9: These figures illustrate the second-order Taylor’s test. The test is performed by computing the functional and the associated gradient when we randomly perturb the viscosity field and subsequently divide the perturbations by a factor of two at each level. The dashed line represents the theoretical convergence rate of $O(2.0)$.

mation on how the control parameter should be adjusted to minimize the objective function. Specifically, the gradient field indicates the sensitivity of the objective functional to changes in control viscosity: positive regions suggest areas where increasing viscosity would reduce the misfit, whereas negative regions indicate where decreasing viscosity would be beneficial. By analyzing these gradients, we not only determine the most efficient descent directions for the optimization but also gain physical insights into how different regions of the mantle structure influence surface observables such as dynamic topography and velocity. Figure 4.8 shows the computed gradients of each term in the objective functional with respect to the control parameter μ . The dynamic topography misfit gradient is concentrated near the surface, indicating that shallow features primarily influence the surface expression of topography. In contrast, the velocity misfit gradient spans a broader depth range and captures the overall flow structure, indicating that surface velocity is sensitive to deeper mantle dynamics. The gradients of the regularization terms: smoothing and damping, are spatially smoother and more uniformly distributed, as expected from their stabilizing role. The gradient of the total objective functional, shown in the final panel, results from the superposition of all these components, weighted as defined in the functional. Visually, it retains strong features from the velocity misfit while being modulated near the surface by the dynamic topography component. This analysis clearly shows that the two surface observables, dynamic topography and surface velocity, respond differently to changes in viscosity. While both play an important role in the inversion, the velocity mis-

fit is more sensitive to the underlying viscosity structure in this temperature-dependent case. Thus, surface velocity offers a stronger constraint on the viscosity field compared to dynamic topography alone.

To verify the correctness of the computed gradients, we perform a second-order Taylor remainder test (Lines 57–58). In this test, small random perturbations are applied to the viscosity field, and the Taylor remainder is computed for a sequence of decreasing perturbation amplitudes as discussed in Section 3.3. As shown in Figure 4.9, the test confirms a convergence rate of $\mathcal{O}(2.0)$, validating the correctness of the adjoint-derived gradients and ensuring the accuracy of subsequent optimization steps.

4.2.4 Optimization and Inversion

```

1 .....
2 # Performing bounded non-linear optimisation
3 mu_lb = Function(mu_control.function_space(), name="Lower_bound_mu").assign(1e-2)
4 mu_ub = Function(mu_control.function_space(), name="Upper_bound_mu").assign(1.0)
5
6 minimisation_problem = MinimizationProblem(reduced_functional, bounds=(mu_lb, mu_ub))
7
8 optimiser = LinMoreOptimiser( minimisation_problem, minimisation_parameters,) #lin-more optimiser
9 optimiser.run()
10 VTKFile("final_solution.pvd").write(optimiser.rol_solver.rolverator.dat[0])

```

Listing 3: Setup and execution of the bounded non-linear viscosity inversion using the Lin-More optimizer.

Having computed the adjoint-based gradient of the objective functional, we now proceed to the optimization phase to minimize the objective and infer the viscosity field. Using G-ADOPT, this process becomes straightforward once the reduced functional is defined, as many underlying complexities are handled automatically (Ghelichkhan et al., 2024). A bounded non-linear optimization is performed, with viscosity bounds set between 10^{-2} and 1.0 (Listing 3, Lines 3–4). These bounds ensure that the recovered viscosities remain within physically reasonable limits. The minimization problem is defined in Line 6 using the reduced functional and the specified bounds. Optimization parameters such as the trust region radius, step size, convergence tolerance, and maximum number of iterations are configured. The Lin-More algorithm (discussed in Section 3.4 from the Rapid Optimization Library (ROL) is employed (Line 8) to iteratively update the control variable μ_{control} , utilizing gradient information at each step. The optimization process terminates once the gradient norm falls below a prescribed threshold, the

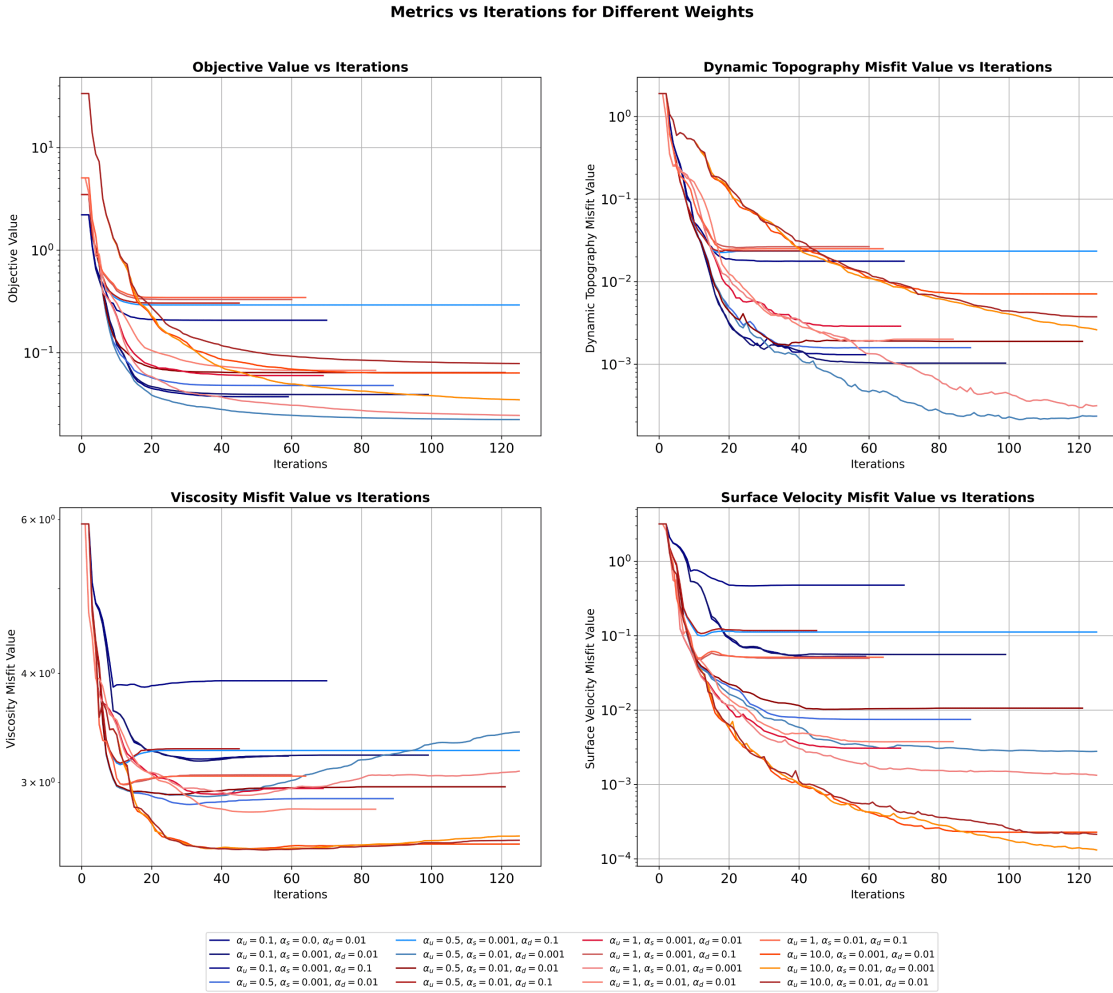


Figure 4.10: Evolution of the objective functional, dynamic topography misfit, surface velocity misfit, and viscosity misfit during optimization iterations.

objective reduction plateaus, or the iteration limit is reached. Upon completion, the optimized viscosity field is exported for visualization and analysis (Line 10).

4.2.5 Results

To systematically study the influence of regularization and misfit weightings, a suite of 125 inverse simulations was performed. The smoothing weight (α_s) and damping weight (α_d) were varied over the range [0, 0.5], while the velocity misfit weight (α_u) was varied over [0, 10]. The dynamic topography misfit weight (α_{dt}) was held fixed at 1.0. For each case, we evaluated the final objective value, dynamic topography misfit, surface velocity misfit, and viscosity misfit. The optimization results revealed that excessive smoothing ($\alpha_s = 0.1$ or 0.5) degraded the inversion by over-regularizing the solution, while optimal performance was consistently achieved

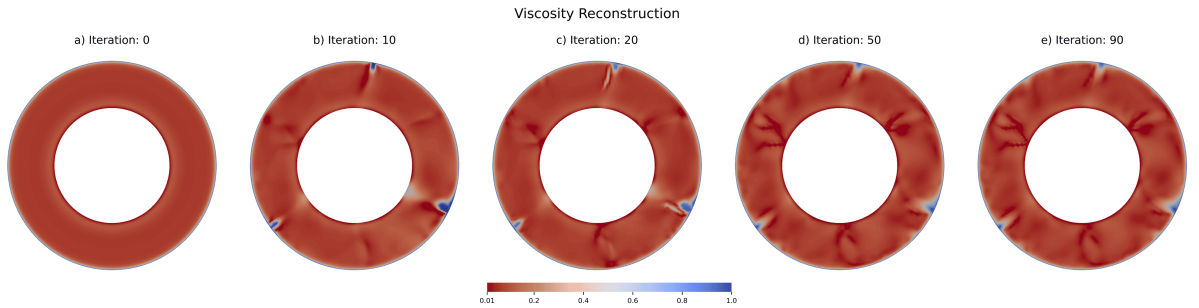


Figure 4.11: Viscosity reconstruction during optimization: initial guess and intermediate states at 10, 20, 50 iterations, compared to the final inverted viscosity and the observed viscosity.

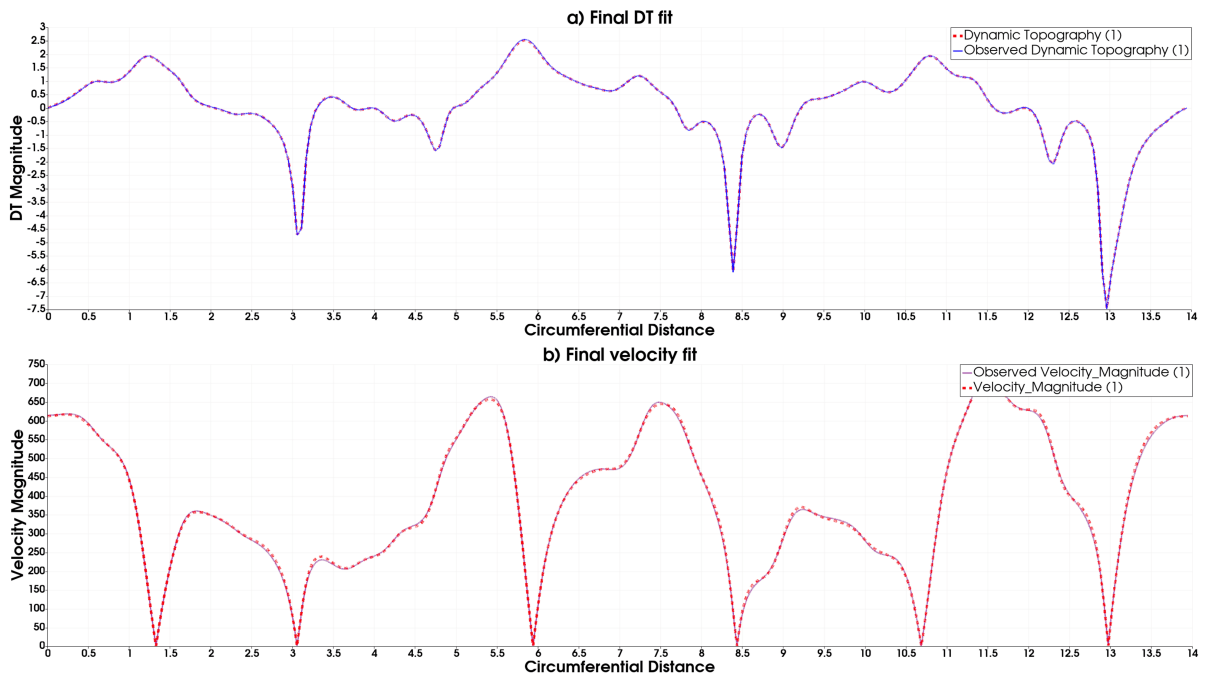


Figure 4.12: Final fit of dynamic topography and surface velocity fields after optimization for the best-performing case.

for $\alpha_s = 10^{-2}$ and $\alpha_d = 10^{-2}$ (see Fig. 4.10). Velocity misfit weighting played a critical role: higher weights ($\alpha_u \gtrsim 0.5$) consistently led to better reconstructions, emphasizing the importance of surface velocity information for constraining the viscosity field.

The best-performing case utilized $\alpha_u = 1.0$, $\alpha_s = 10^{-2}$, and $\alpha_d = 10^{-2}$. Figure 4.10 shows the convergence behavior of the objective functional and misfit metrics over iterations. Starting from a layer-averaged initial guess, the inversion reduced the objective function and misfits effectively by three orders of magnitude over approximately 90 iterations. Figure 4.11 illustrates the evolution of the viscosity reconstruction at intermediate stages (after 10, 20, and 50 iterations) and the final inverted viscosity field, compared to the observed viscosity. The inversion

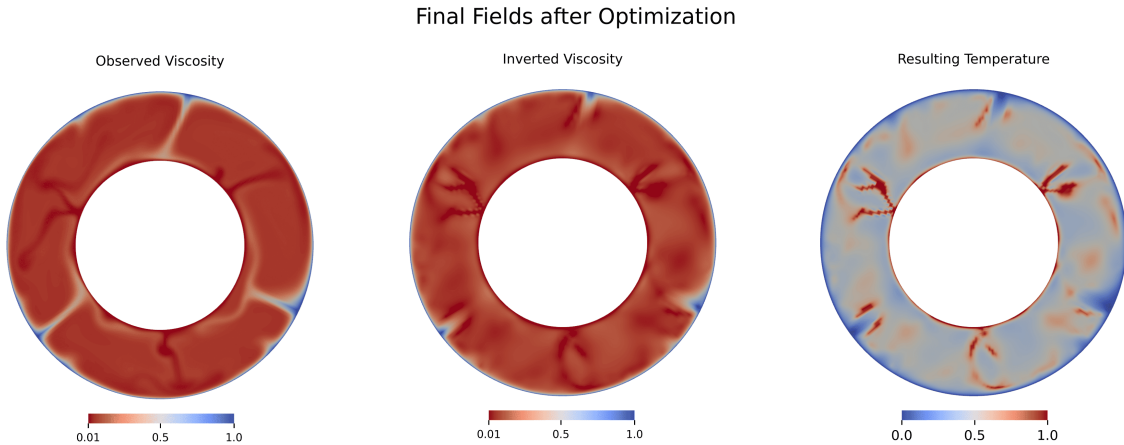


Figure 4.13: Final reconstructed viscosity field after inversion.

captures major mantle structures, such as regions of high and low viscosity, even though fine-scale details are not perfectly recovered (see Figure 4.13). The final fit to the observed dynamic topography and surface velocity fields is shown in Figure 4.12. This analysis highlights several important points:

- The objective functional and misfits were reduced effectively, confirming successful convergence (Figure 4.10).
- The inversion captured key mantle structures, including upwelling and downwelling regions.
- Surface velocity misfit sensitivity was more crucial than dynamic topography in guiding the inversion, particularly due to the linear temperature-dependent viscosity formulation.
- The non-uniqueness of the inversion is evident, as varying the regularization parameters resulted in different reconstructed viscosity fields (Figure 4.10).
- Regularization via smoothing and damping played an essential role in stabilizing the inversion, ensuring that the recovered fields exhibited physically plausible gradual transitions rather than abrupt variations.

Overall, while the misfits decreased substantially, the reconstructed viscosity field does not exactly replicate the observed field, highlighting limitations arising from data sparsity and numerical resolution. Future improvements could involve incorporating additional observational constraints (e.g., seismic tomography) or refining the computational mesh to better capture small-scale heterogeneities.

4.3 Model Configuration 2: Inversion Using Temperature as the Control Parameter

In a parallel inversion analyses to the one described in the previous section, we extended the inversion framework described in Section 2 by treating temperature as the control parameter, rather than viscosity. The goal is to assess whether the adjoint-based inversion process can recover the true temperature field that underlies the observed mantle dynamics. This approach relies on the assumption that viscosity is derived from temperature using a temperature-dependent Arrhenius rheology, as previously defined in Section 4.2.1.

4.3.1 Forward Model and Gradient Calculation

The forward model setup, mesh geometry, and solver configuration used in this setup are identical to those described in inversion setup 1 (Section 4.2). As before, synthetic observations are generated by evolving the forward model to a steady-state using the known true temperature field (see Listing 1). The resulting dynamic topography and surface velocity fields, along with the steady-state temperature and viscosity fields, are saved and treated as the observed data for inversion. To initialize the inversion, we define the control field, temperature, using a layer-averaged profile of the observed temperature field as shown in Figure 4.14. This provides a smooth, but incorrect initial guess, analogous to the initial guess used for viscosity in the previous inversion setup. On the basis of this temperature guess, the viscosity field is calculated using the Arrhenius law (Equation 4.1). Using these incorrect temperature and viscosity fields, we solve the Stokes equations to obtain the corresponding model-predicted dynamic topography and surface velocity fields. These are then compared against the observed fields to compute the misfit and construct the objective functional as shown in Figure 4.15.

The misfit terms and the objective function follow the same structure as in Section 3.1. The dynamic topography misfit and surface velocity misfit are both calculated at the top boundary, and normalization terms are computed with respect to the L^2 -norms of the observed fields. These are given by:

$$\text{smoothing} = \frac{N_{\text{dt}}}{N_s} \int_{\Omega} |\nabla(T - \bar{T})|^2 \, dx, \quad (4.3)$$

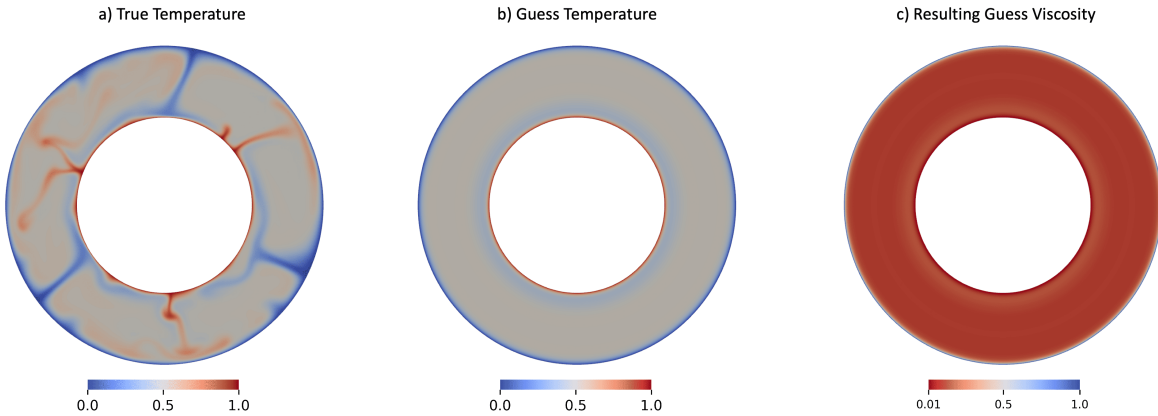


Figure 4.14: Initial guess fields used for inversion: (a) synthetically generated true temperature field, (b) layer-averaged temperature field used as the control parameter, (c) corresponding viscosity field computed via the Arrhenius relation.

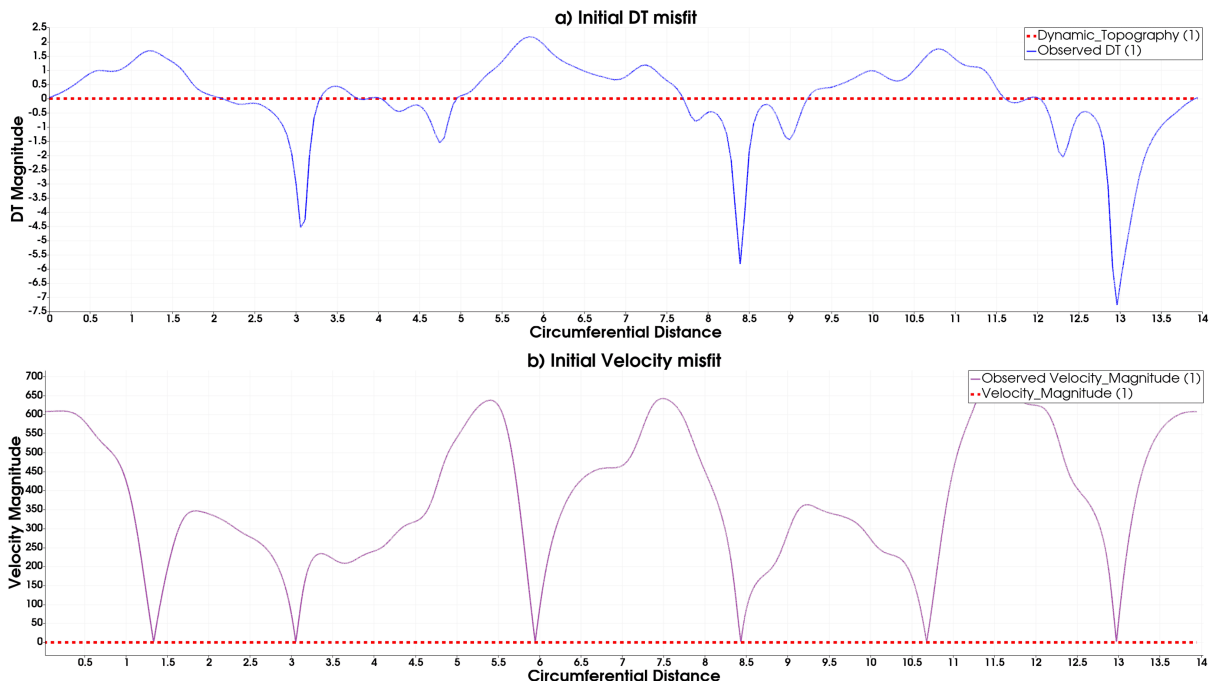


Figure 4.15: Initial misfit fields computed from the initial temperature and viscosity guess: (a) dynamic topography misfit, (b) surface velocity misfit. These quantify the discrepancy between model prediction and synthetic observations at the start of inversion.

$$\text{damping} = \frac{N_{dt}}{N_d} \int_{\Omega} (T - \bar{T})^2 \, dx, \quad (4.4)$$

where \bar{T} denotes the layer-averaged temperature, and N_{dt} , N_s , and N_d are the normalization factors defined earlier (Section 3.1). Following the construction of the objective functional, the reduced functional is defined using the control variable T_{control} , and its gradient is auto-

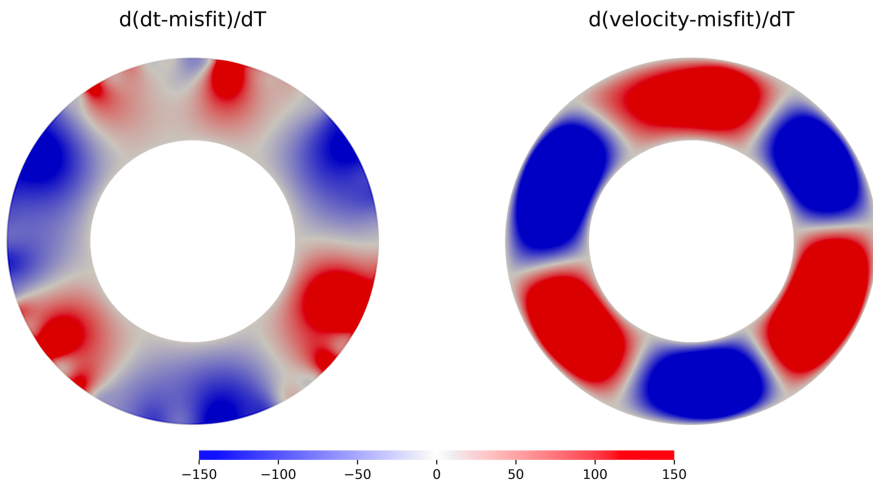


Figure 4.16: Gradients of the objective functional with respect to temperature: (left) sensitivity of the dynamic topography misfit, $\partial J_{dt}/\partial T$, and (right) sensitivity of the velocity misfit, $\partial J_u/\partial T$. These gradients guide the inversion by indicating how temperature should be updated to reduce the respective misfits.

matically computed using the adjoint capabilities of G-ADOPT (similar to Listing 2). These gradients provide directional information on how the temperature field should be modified to reduce the surface misfits. Gradient validation is performed using the second-order Taylor remainder test. Random perturbations are added to the temperature control field, and the Taylor error is computed for decreasing perturbation amplitudes. The observed convergence rate of $\mathcal{O}(2.0)$ confirms the accuracy of the computed gradient. The gradients of the objective functional with respect to the control parameter, temperature, are shown in Figure 4.16. We observe a general trend in both gradient fields, with clear large-scale structures aligned with the plume features. However, finer-scale details are less pronounced. In the next subsection, we analyze the optimization results and compare them to the known synthetic truth.

4.3.2 Optimization and Inversion

The inversion was performed using temperature as the control parameter, subject to bounds consistent with the Dirichlet boundary conditions of the normalized temperature field. As shown in Listing 4, Lines 3–4, the lower and upper bounds were set to 0.0 and 1.0, respectively. These bounds ensure that the optimizer does not explore non-physical values during the update process.

After defining the reduced functional and applying the bounds, we constructed a mini-

```
1 # Performing bounded non-linear optimisation
2 T_lb = Function(T_control.function_space(), name="Lower_bound_T").assign(0.0)
3 T_ub = Function(T_control.function_space(), name="Upper_bound_T").assign(1.0)
4
5 minimisation_problem = MinimizationProblem(reduced_functional, bounds=(T_lb, T_ub))
6
7 optimiser = LinMoreOptimiser(minimisation_problem, minimisation_parameters)
8 optimiser.run()
9
10 VTKFile("final_solution.pvd").write(optimiser.rol_solver.rolverator.dat[0])
```

Listing 4: Setup and execution of the bounded nonlinear optimization using temperature as the control variable.

mization problem and passed it to the Lin-More optimizer from the Rapid Optimization Library (ROL) (Lines 5–8). The optimization was run with a maximum of 100 iterations. For this test case, the regularization and misfit weights were chosen as $\alpha_u = 1.0$, $\alpha_s = 10^{-3}$, and $\alpha_d = 0.1$, based on prior experiments. The optimizer iteratively minimized the objective functional, incorporating both misfit and regularization components. The convergence of the objective functional, along with the dynamic topography misfit, velocity misfit, and temperature misfit, was monitored throughout the inversion as we can see in Figure 4.17. These metrics allowed us to evaluate the performance of the recovered model.

4.3.3 Results

Although the optimizer successfully minimized the objective functional and associated misfits which can be seen from Figure 4.17, the final inverted fields do not match the observed fields satisfactorily. Figure 4.19 shows the reconstructed temperature and the resulting viscosity field after optimization. While some shallow structures are vaguely captured, the deeper mantle structures are not recovered. This indicates that the inversion likely converged to a local minimum, rather than recovering the global solution. A central challenge in this inversion scenario lies in the choice of control parameter. Temperature, while physically meaningful, is less directly constrained by surface observables such as dynamic topography and surface velocity. These quantities are more sensitive to smoothed, integrated effects of temperature through their impact on viscosity, making the inversion for temperature inherently more ill-posed.

These limitations are also evident in the computed gradients (Figure 4.16). The gradient of the dynamic topography misfit is relatively diffuse and concentrated near the surface, suggesting it carries limited sensitivity to deeper thermal variations. The velocity misfit gradient

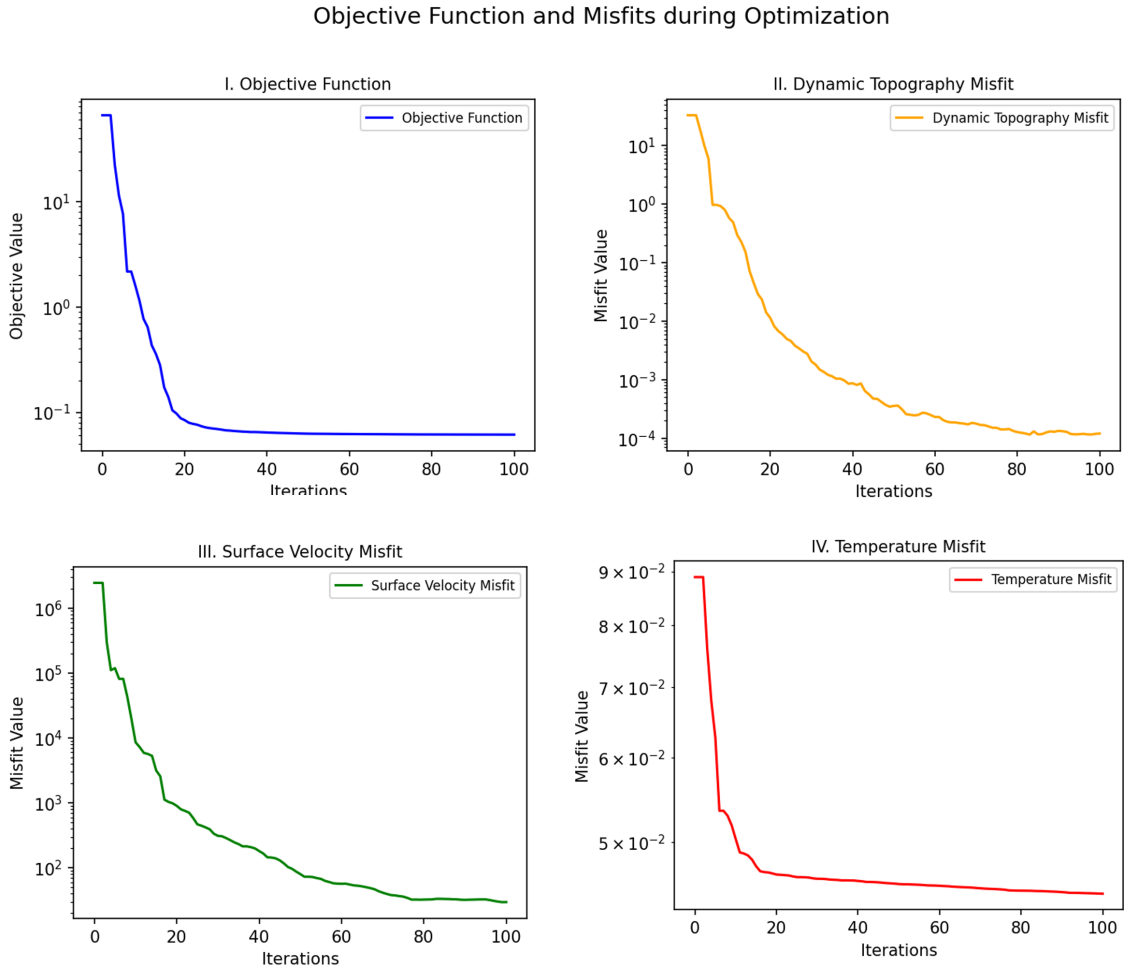


Figure 4.17: Convergence of the inversion using temperature as the control parameter. The evolution of the objective functional, dynamic topography misfit, surface velocity misfit, and temperature misfit is shown over 100 optimization iterations.

is more structured and extends deeper, but still lacks the fine-scale detail necessary to guide precise updates in the control field. Thus, we can say that the optimizer had limited directional information to improve the control field beyond the shallowest structures. This aligns with the final result, where only broad shallow structures are captured while deeper features are completely missed (Figure 4.19). Several contributing factors can explain this reconstruction:

- The inversion is fundamentally under-constrained: it attempts to recover a complex, high-dimensional temperature field using only surface observations, which provide limited information about the mantle. More observational constraints, such as seismic tomography, are required.
- Because viscosity depends non-linearly on temperature and acts as a smoothing operator,

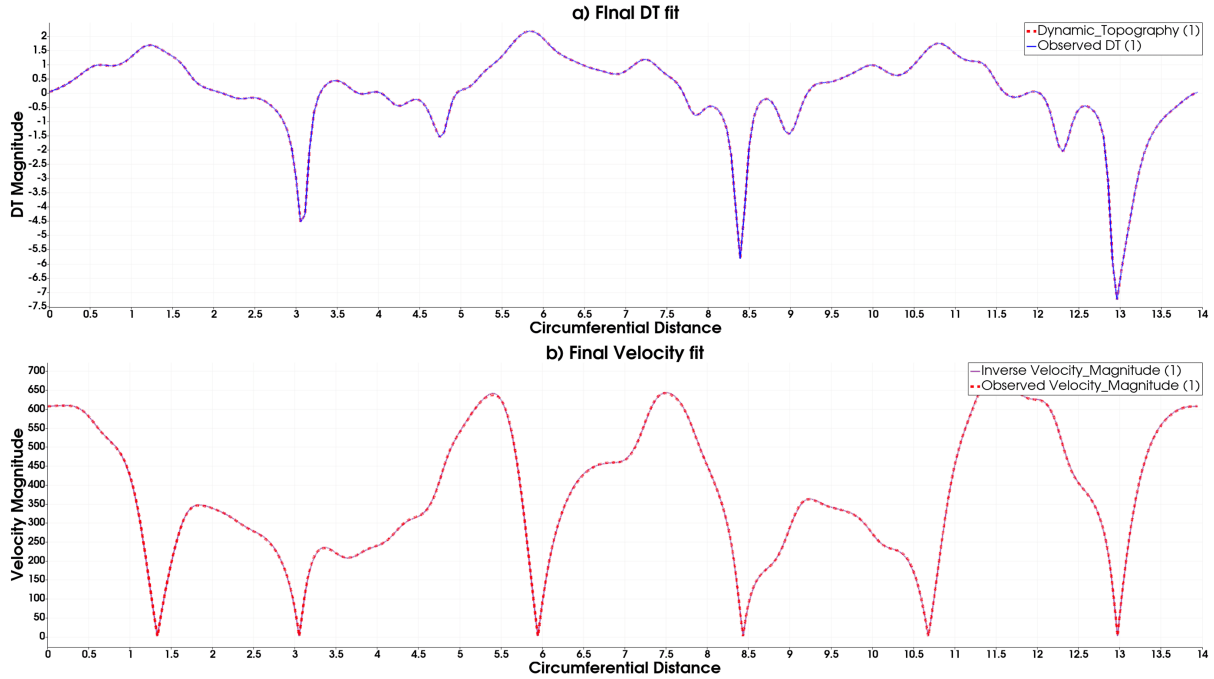


Figure 4.18: Final fit of surface observables for the best-performing temperature-controlled inversion: (a) dynamic topography misfit, (b) surface velocity misfit.

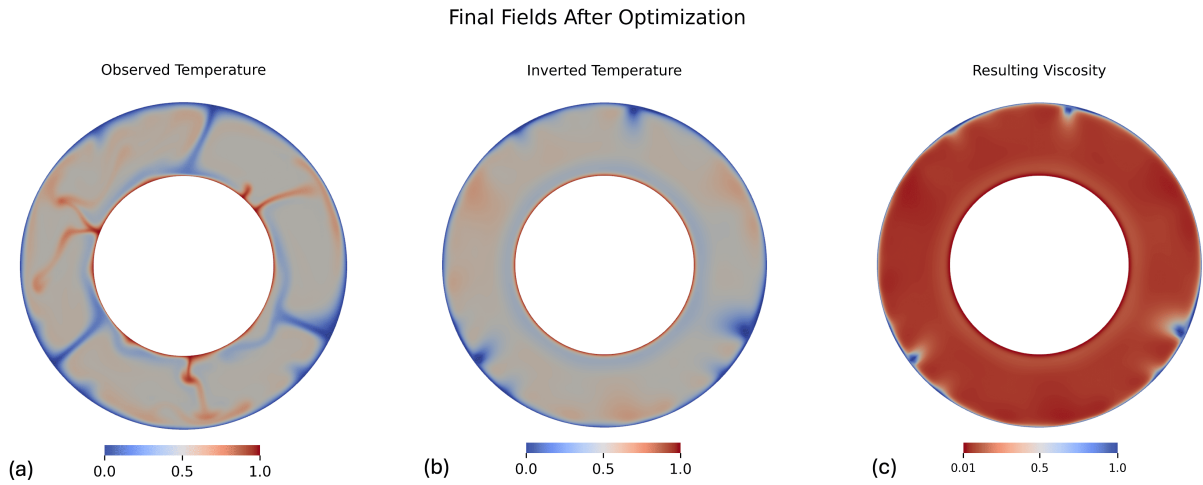


Figure 4.19: Final fields after inversion using temperature as the control variable: (a) observed temperature field, (b) reconstructed temperature field, (c) resulting viscosity field computed from the Arrhenius law. The inversion captures some shallow features but fails to reconstruct most of the mantle structures.

small-scale temperature variations have little impact on surface signals. This makes it difficult for the inversion to detect or correct finer details in the temperature field.

- Regularization, while essential to prevent instability, tends to suppress small-scale updates, especially in deeper regions where the data sensitivity is already weak.

- The optimization landscape is non-convex, i.e. there are multiple local minima. In this case, the optimizer appears to have settled into one such minimum, guided by shallow and incomplete gradient information (Figure 4.18).

Overall, while the objective and misfit values were significantly reduced, the reconstructed fields did not provide a physically meaningful match to the true model.

Chapter 5

Numerical Implementation and Results:

Inversion of Rheological Parameters

This chapter continues the inverse modeling efforts introduced in Chapter 4. The previous attempts to recover mantle properties using viscosity and temperature as control variables did not lead to reconstructions that were both accurate and physically consistent, especially under more complex rheological conditions. To address these limitations, we now consider activation energy E_a as the primary control parameter. Since E_a directly controls the temperature dependence of viscosity via the Arrhenius law (Equation 2.8), it offers a more targeted way to explore how mantle rheology influences surface signals. In these cases, we assume the temperature field is already known, based on constraints from tomography or other geological models. This allows us to reduce the number of unknowns and focus on the spatial structure of E_a . The chapter presents three configurations of increasing complexity: a single uniform value, a depth-dependent profile, and a fully spatially varying field within a nonlinear viscoplastic mantle model that more closely reflects realistic conditions.

5.1 Model Configuration 3: Inversion Using Activation Energy as the Control Parameter

This configuration represents the first in a series of tests focused on recovering activation energy E_a from surface observables. We assume a known temperature field and seek to infer a spatially uniform E_a value, which governs the temperature sensitivity of viscosity via the simplified Arrhenius formulation (Equation 4.1). With the temperature field fixed, the goal is to examine how well the inversion can reconstruct a scalar rheological control, and how the outcome is influenced by the relative weighting of different observables in the objective functional.

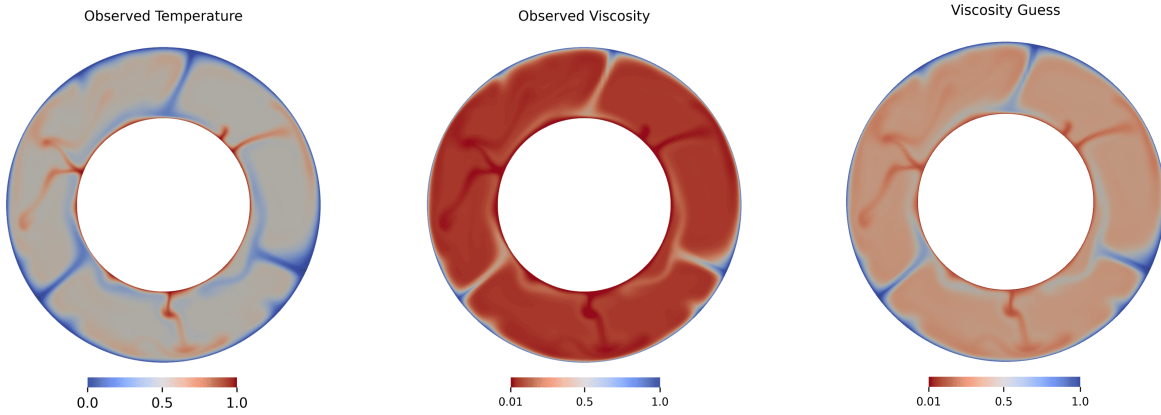


Figure 5.1: Comparison of observed and initial guessed fields: (a) observed temperature, (b) observed viscosity, (c) guessed viscosity from initial $E_a = 2.0$, (d) viscosity misfit. The initial guess fails to capture the strong spatial variability present in the observed viscosity.

5.1.1 Forward Model and Gradient Calculation

We consider a simplified case in which the activation energy is treated as a single constant parameter, defined over the real-valued function space \mathbb{R} (Line 11, Listing 5). In the forward model used to generate the synthetic observations (Section 4.2.1), the true activation energy was set to $E_a = \ln(100) \approx 4.605$ (Line 7). We used the same synthetic data set, including the temperature field, dynamic topography, and surface velocity, as input for the inversion. These steady-state fields were previously saved and now serve as the reference observations (Lines 5–6).

Figure 5.1 shows a comparison between the observed and guessed fields. The observed temperature and viscosity fields correspond to the synthetic model generated using the true activation energy $E_a \approx \ln(100) \approx 4.605$. The initial guess $E_a = 2.0$ produces a much weaker temperature dependence in viscosity, resulting in a relatively uniform viscosity field and substantial deviation from the observed structure. The resulting viscosity misfit confirms that the guessed model does not adequately represent the true physical behavior. Figure 5.2 displays the misfit fields computed from this incorrect initial guess. The dynamic topography and velocity misfits are both significant, as expected. The underestimated activation energy leads to a weaker viscosity contrast, producing dynamic responses inconsistent with the observed surface signals.

The inversion begins by assigning an incorrect initial value of $E_a = 2.0$ (Line 17), which is significantly different to the true value. This scalar parameter serves as the control vari-

```

1 from gadopt import *
2 from gadopt.inverse import *
3 rmin, rmax = 1.22, 2.22
4 with CheckpointFile("../forward/Final_State.h5", "r") as forward_check:
5     T = forward_check.load_function(mesh, "Temperature") #Assume that we have the temperature field
6     dtopo_obs = forward_check.load_function(mesh, "Observed DT")
7     Ea_obs = forward_check.load_function(mesh, "Observed Ea") #Obs Value of activation energy = ln(100) = 4.605
8
9 # Define the function spaces
10 ...
11 R = FunctionSpace(mesh, "R", 0) # Real function space (for constants)
12
13 Ra = Function(R, name="Rayleigh Number").assign(5e4) # Rayleigh number
14 approximation = BoussinesqApproximation(Ra)
15
16 # for the inverse problem, we define the control variable
17 Ea_control = Function(R, name="Activation_Control").assign(2.0) # incorrect initial guess
18 control = Control(Ea_control) # control we give to the reduced functional
19 # calculate resulting viscosity
20 mu = Function(Q1, name="viscosity").project(exp(-Ea_control * T), bcs=mu_bcs) #using simplified arrhenius law
21 ...
22 # define stokes equations and boundary conditions
23 ...
24 # solve the stokes equations
25 stokes_solver.solve()
26 surface_force = surface_force_solver.solve() #to calculate the dynamic topography
27 dtopo.interpolate((surface_force/deltarho_g)) #guess DT
28 ...
29 # misfit calculation
30 dt_misfit = assemble((dtopo - dtopo_obs)**2 * ds_t)
31 u_misfit = assemble(dot(u - u_obs, u - u_obs) * ds_t)
32 alpha_dt, alpha_u = 1.0, 0.1 # relative weights
33 ...
34 # objective function
35 objective = alpha_dt * dt_misfit + alpha_u * (norm_dt * (u_misfit/ norm_u_surface))
36 # reduced functional
37 reduced_functional = ReducedFunctional(objective, control)
38 grad_func = reduced_functional.derivative(options={"riesz_representation": "L2"}) # gradient calculation
39 log(f"Derivative: {der_func.dat.data}") # print the values of the gradient
40 ...
41 # taylor's test to check the gradient
42 delta_Ea.dat.data[:] = np.random.random(delta_Ea.dat.data.shape) * 0.1 #add pertubations
43 minconv = taylor_test(reduced_functional, Ea_control, delta_Ea) # taylor's test

```

Listing 5: Selected lines from the inversion setup using activation energy as the control parameter, showing initialization, forward solve, misfit computation, gradient verification, and nonlinear optimization.

able (Line 18). Using the known temperature field T , the viscosity field is recalculated as $\mu(T) = \exp(-E_a \cdot T)$ as shown in Line 20. The updated viscosity is then used to solve the Stokes equations (Line 25), and the resulting surface normal stress is used to calculate the dynamic topography prediction (Lines 26–27). We define misfits by comparing the modeled dynamic topography and velocity with their observed counterparts (Lines 30–31). The objective functional is constructed as a weighted sum of the dynamic topography and velocity misfit terms (Line 35), with weights α_{dt} and α_u . Since E_a is a single constant value, we do not include regularization terms like smoothing or damping, which are typically applied to spatially varying fields.

To better understand how the objective function responds to changes in the control vari-

Parameter	Value
Initial Guess E_a	2.0
Observed E_a	≈ 4.605
Gradient of DT misfit $\frac{d(J_{DT})}{dE_a}$	-0.0454
Gradient of velocity misfit $\frac{d(J_u)}{dE_a}$	-0.5699

Table 5.1: Initial and observed values of activation energy and corresponding gradient sensitivities of the objective function components.

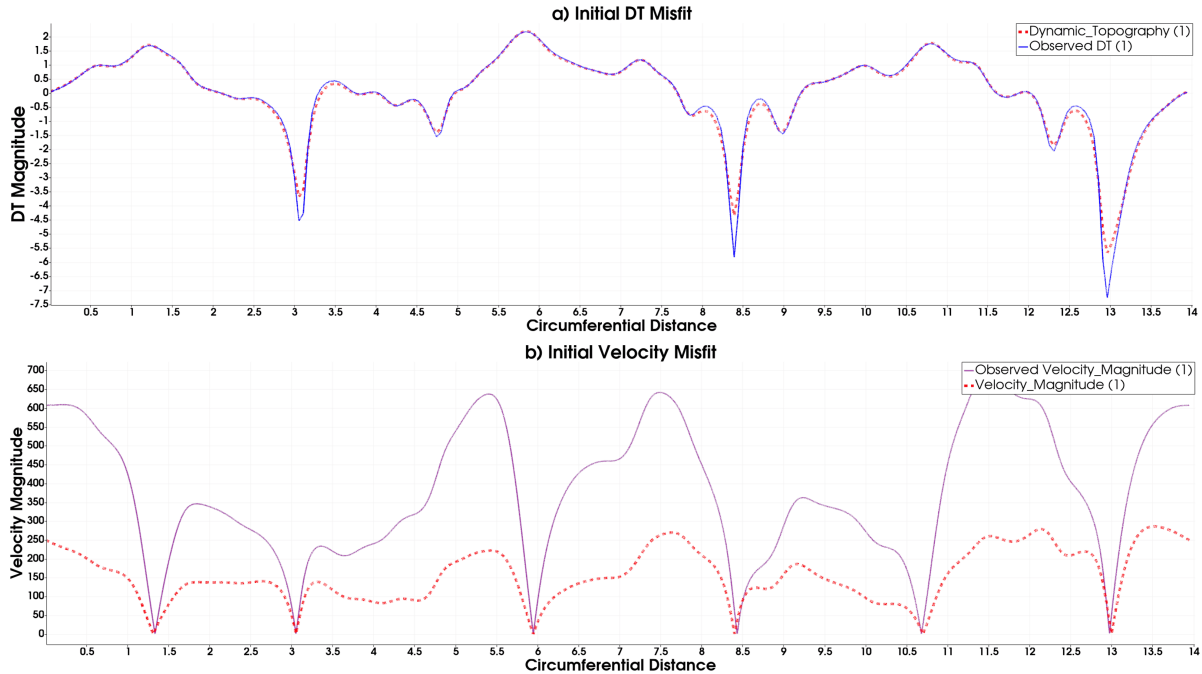


Figure 5.2: Initial misfit fields computed using the guessed activation energy: (a) dynamic topography misfit and (b) surface velocity misfit. Both fields show significant discrepancies, particularly near upwelling and downwelling regions, indicating where the initial model deviates from the observations.

able, Table 5.1 summarizes the initial guess and observed value of activation energy, along with the computed gradients of the component terms of the objective functional. These gradient values show that both components of the objective function decrease with increasing E_a , as indicated by the negative signs. Notably, the gradient associated with the velocity misfit is an order of magnitude larger, suggesting that surface velocity provides a much stronger constraint on the activation energy than dynamic topography in this configuration. This directional information will guide the optimizer to increase E_a during the inversion process.

The reduced functional is defined using the objective and the control parameter E_a (Line 37). The gradient of this functional is computed using G-ADOPT's adjoint framework (Line

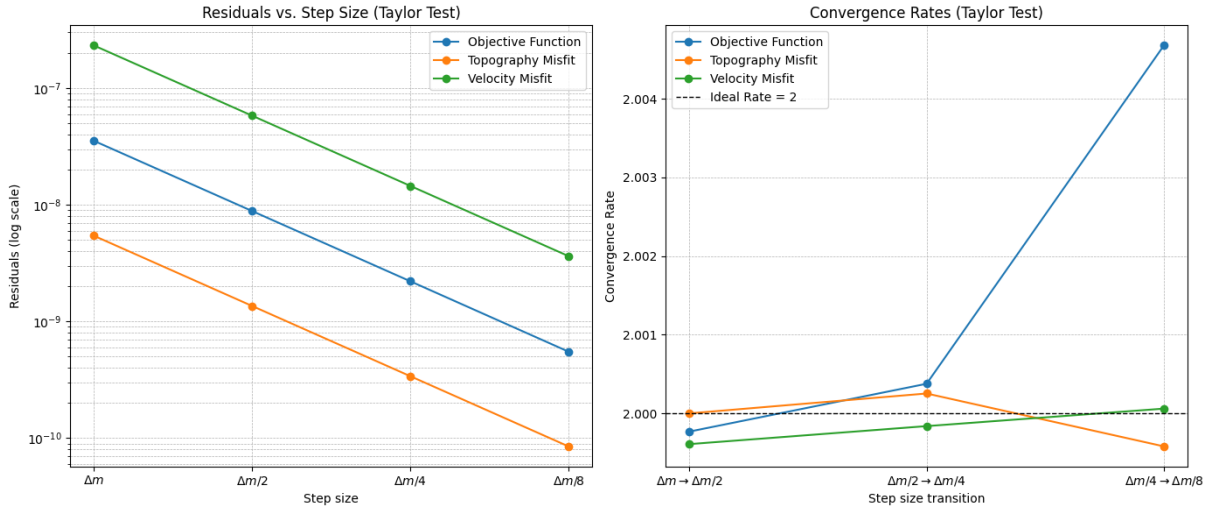


Figure 5.3: Second-order Taylor remainder test for the activation energy inversion. The plot shows convergence consistent with $\mathcal{O}(2.0)$, confirming the correctness of the computed gradient.

38), providing a sensitivity measure that guides the optimization. The gradient value is printed in Line 39 for inspection and analysis. As explained earlier, we verify the validity of the gradients by performing a second-order Taylor convergence test as shown in Lines 41-43. The results are shown in Figure 5.3, demonstrating that the gradients exhibit the expected $\mathcal{O}(2.0)$ convergence rate.

5.1.2 Optimization and Inversion

```

1 .....
2 -----inversion-----
3 # bounded non-linear inversion
4 Ea_lb = Function(Ea_control.function_space(), name="Lower_bound_Ea").assign(1.0)
5 Ea_ub = Function(Ea_control.function_space(), name="Upper_bound_Ea").assign(10.0)
6
7 minimisation_problem = MinimizationProblem(reduced_functional, bounds=(Ea_lb, Ea_ub))
8 ...
9 optimiser = LinMoreOptimiser( minimisation_problem, minimisation_parameters, )
10 optimiser.run()
11 # visualise the inversion results
12 Ea_inverted = Function(R, name="Activation Energy").project(optimiser.rol_solver.rolverator.dat[0])
13 mu_inverted = Function(Q1, name="Viscosity").project(exp(-Ea_inverted * T), bcs=mu_bcs)
14 VTKFile("final_solution.pvd").write(Ea_inverted, mu_inverted)

```

Listing 6: Setup and execution of the bounded nonlinear optimization using activation energy as the control variable.

The inversion was performed using activation energy E_a as the control parameter, defined as a scalar function over the real-valued function space \mathbb{R} . As shown in Listing 6, Lines 4–5, the bounds for E_a were set to 1.0 and 10.0, respectively, to ensure physically meaningful

updates during the optimization process. Following the construction of the reduced functional and the imposition of bounds, a minimization problem was formulated and solved using the Lin-More algorithm from the Rapid Optimization Library (ROL) (Lines 7–9). Since the control parameter is a single scalar value, the optimization converged relatively quickly, typically within 10 iterations and always before reaching the 25 iteration limit.

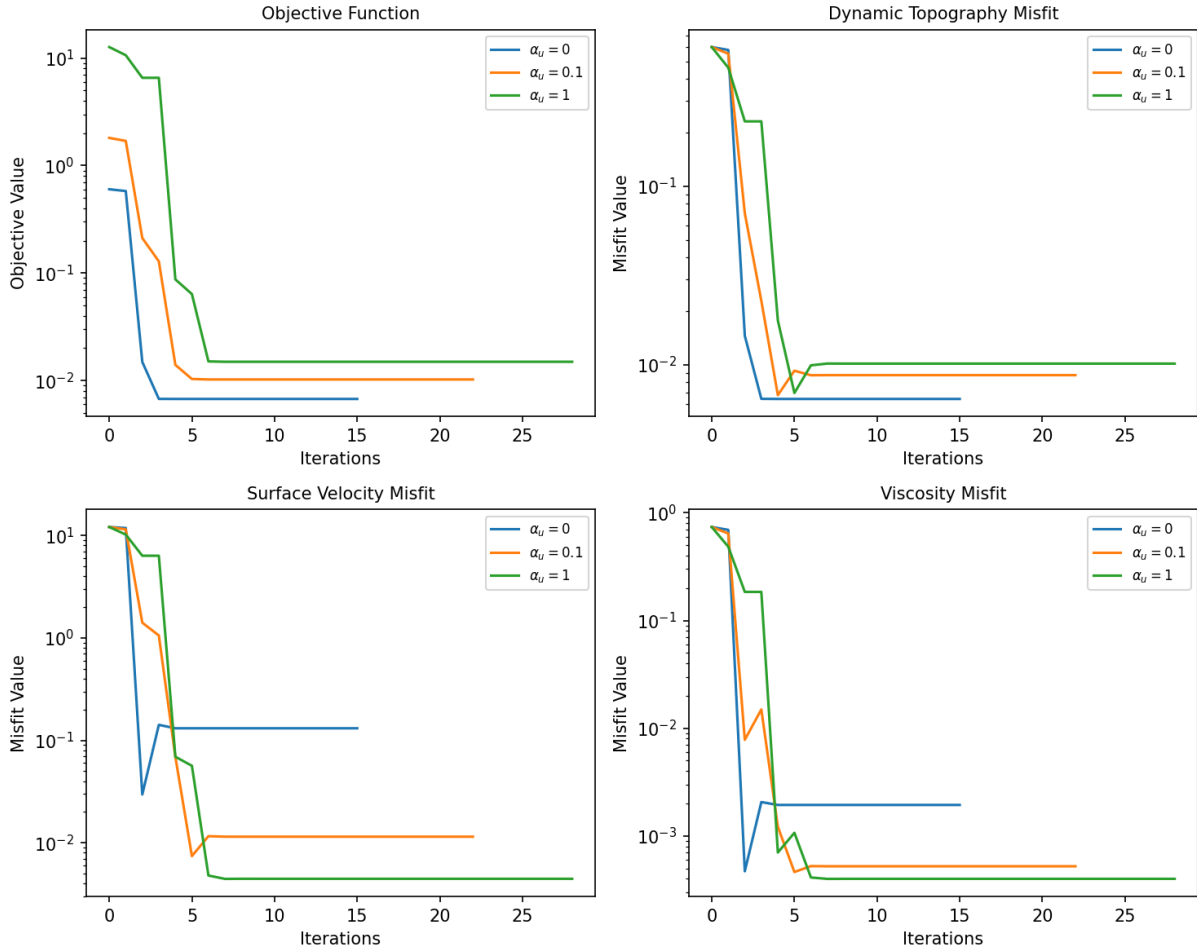


Figure 5.4: Convergence of the inversion for different values of α_u . Evolution of the objective functional and misfit terms (dynamic topography, velocity, and viscosity) across optimization iterations.

To evaluate the impact of the velocity misfit term on inversion performance, we conducted three optimization runs with different values of the weighting parameter $\alpha_u \in \{0, 0.1, 1.0\}$, while keeping the dynamic topography weight fixed at $\alpha_{dt} = 1.0$. For each case, we recorded the evolution of the objective functional, dynamic topography misfit, velocity misfit, and the inferred value of E_a across iterations.

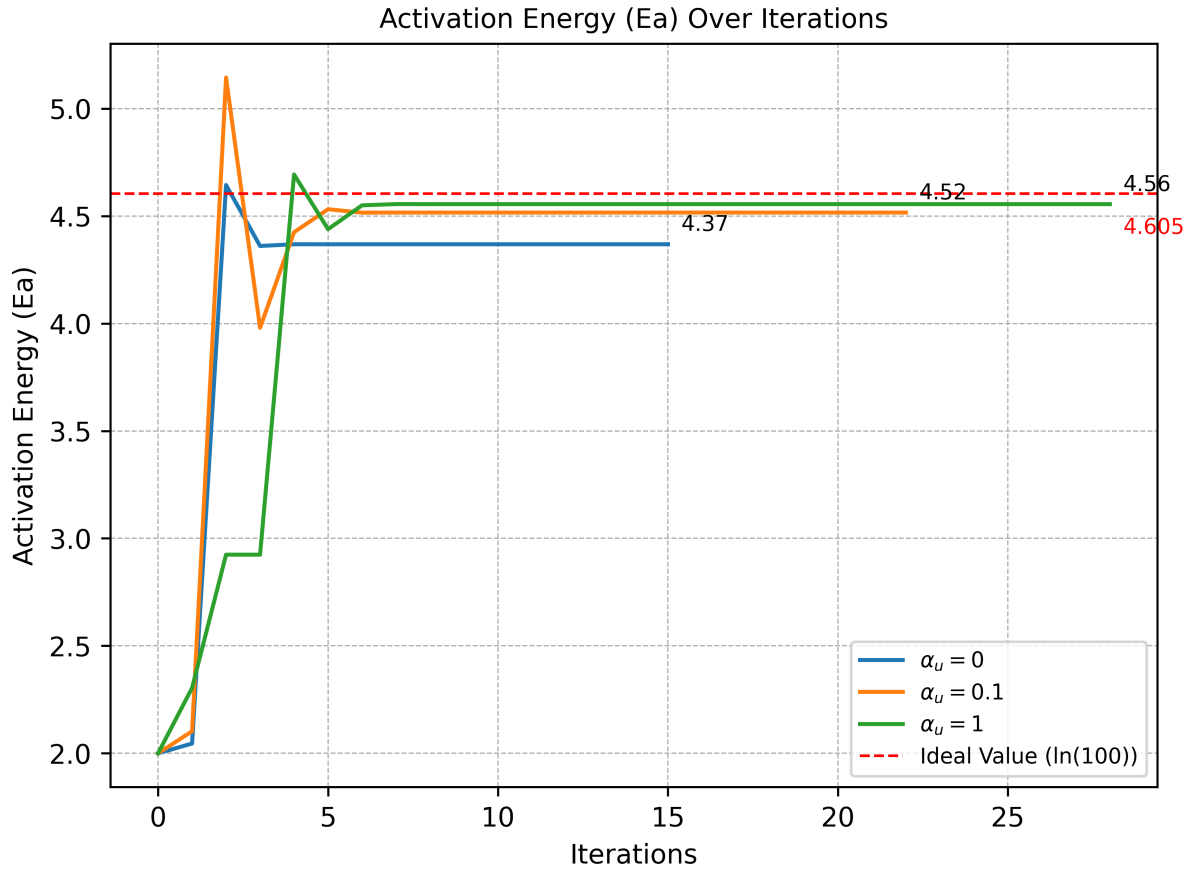


Figure 5.5: Reconstruction of the estimated activation energy across iterations for different values of α_u . Convergence is most accurate for $\alpha_u = 1.0$.

5.1.3 Results

The inversion yielded highly accurate results for this simplified case. All three inversion cases achieved low viscosity misfits and successfully minimized the objective function, with most converging within 10 iterations (Figure 5.4). The activation energy recovered by the optimizer was consistently close to the true value $E_a \approx \ln(100) \approx 4.605$, irrespective of the initial guess. Several key observations emerge from the optimization outcomes:

- The optimizer converged quickly in all cases due to the low-dimensional control space and well-posed nature of the problem.
- Increasing the weight α_u on the velocity misfit term improved both the convergence behavior and the quality of the final solution (Figures 5.4, 5.5).
- Models with higher α_u provided better fits to the observed velocity field and yielded viscosity fields that closely matched the reference (Figures 5.6, 5.7).

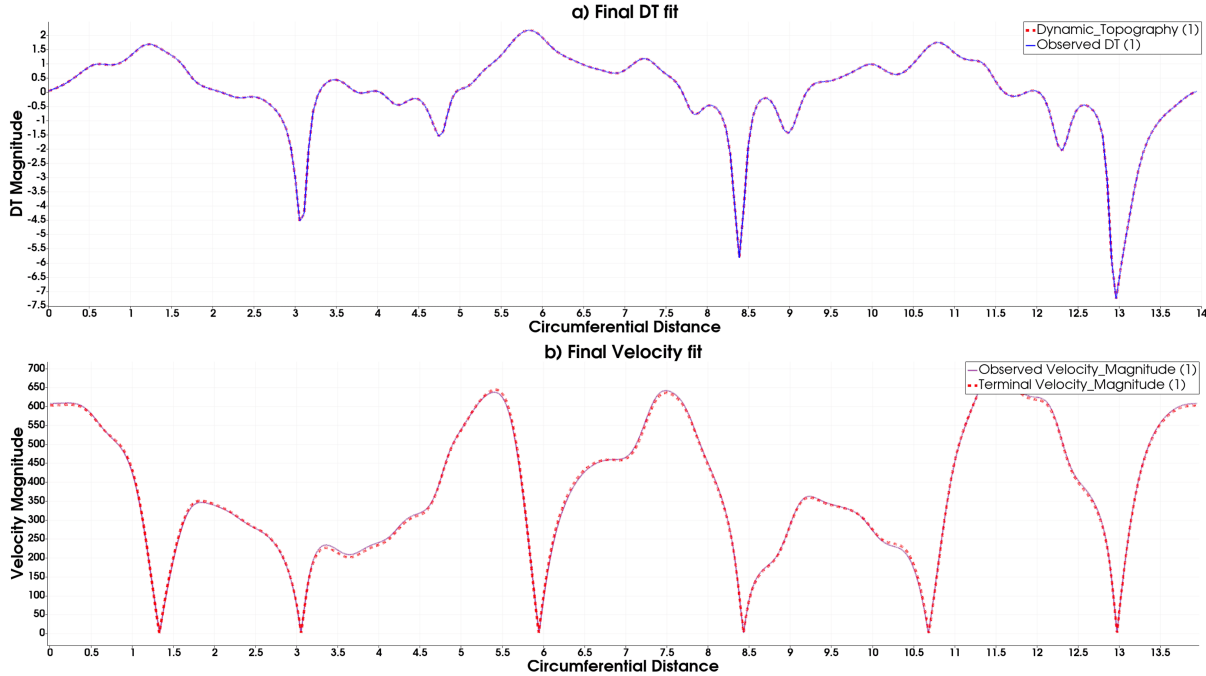


Figure 5.6: Final fit of surface observables: (a) dynamic topography and (b) surface velocity. The accuracy improves with increasing α_u , indicating the importance of velocity in constraining the inversion.

- The best-performing case ($\alpha_u = 1.0$) recovered the target viscosity structure with minimal misfit, demonstrating strong sensitivity of surface velocity to the activation energy parameter.
- This case remains idealized as it assumes uniform activation energy and an exact temperature field. However, it serves as an effective benchmark for evaluating more complex setups shown in subsequent inversion studies.

These results confirm that using activation energy as the control variable, combined with known temperature and surface data, can lead to a robust inversion. Surface velocity plays a particularly important role in constraining the solution when appropriately weighted. However, the strong performance here is partly due to the idealized nature of the setup, which assumes a uniform activation energy and perfect knowledge of the temperature field. In reality, mantle rheology is more complex, involving depth dependence, plasticity, and uncertainties in input data such as tomography.

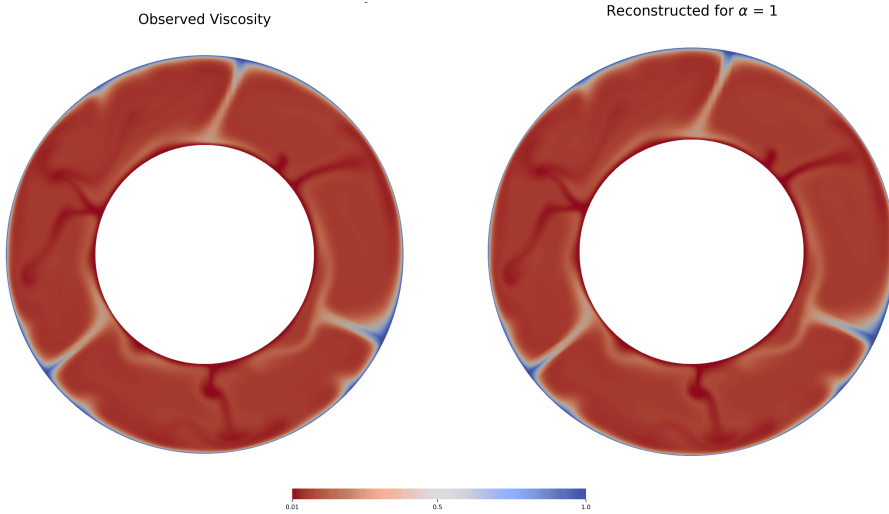


Figure 5.7: Reconstructed viscosity field for the best-performing case ($\alpha_u = 1.0$). The recovered viscosity matches the observed structure with high fidelity.

5.2 Model Configuration 4: Inversion Using Activation Energy with Depth-Dependent Rheology

To move closer to realistic Earth structure, we now introduce discontinuities in activation energy across depth, representing major mantle layers. This modification enhances the physical realism of the model while still maintaining a linear, temperature-dependent viscosity formulation. Unlike the previous case where activation energy was uniform, it now varies with depth, allowing us to better capture the layered nature of the mantle. The domain is divided into three distinct depth intervals corresponding to the major mantle regions (Turcotte and Schubert, 2002):

- E_{a1} : Activation energy for the lower mantle (from the core-mantle boundary up to 660 km),
- E_{a2} : Activation energy for the transition zone (660 km to 410 km),
- E_{a3} : Activation energy for the upper mantle (above 410 km).

Each region is assigned a distinct activation energy value, resulting in a piecewise-constant activation energy profile. The viscosity is then calculated using a depth-dependent Arrhenius-

type relationship (For detailed explanation see Section 2.2:

$$\mu(T, z) = \exp(-E_{aT} \cdot T + E_{az} \cdot z), \quad (5.1)$$

where E_{aT} represents the activation energy associated with temperature variations, and E_{az} controls the viscosity contrast due to depth. In this setup, E_{az} is assumed to be known and fixed, while E_{aT} varies with depth and is the parameter we aim to recover through inversion. We also assume that the temperature structure T is reasonably well known from seismic tomography or previous studies. Although this rheological model does not yet include non-linear behavior, it represents a step toward incorporating more realistic physical complexities. In this experiment, we test whether surface observations are sufficient to recover layered variations in activation energy when viscosity depends on both temperature and depth.

5.2.1 Synthetic Data Generation

To generate synthetic observations for this synthetic test, we build upon the forward model described in Section 4.2.1, but modify the viscosity formulation to include depth-dependent activation energy. The modified viscosity formulation and depth-dependent activation setup used to generate the synthetic observations are shown in Listing 7. The computational domain remains an annulus bounded between radii $r_{\min} = 1.22$ and $r_{\max} = 2.22$, defining a non-dimensional mantle thickness of 1 and an inner-to-outer radius ratio of 0.55. To introduce vertical rheological layering, we define depth markers corresponding to Earth's mantle structure: 410 km and 660 km, which translate to normalized radii r_{410} and r_{660} , respectively, based on Earth's geometry (Lines 4-10). As in previous setups, we initialize a temperature field as described in Equation 4.2 that triggers four plume upwellings (Line 28), and evolve it using the energy and Stokes equations over 20,000 timesteps to reach a steady state. We maintain fixed temperature boundary conditions at the top and bottom boundaries ($T_{\text{CMB}} = 1.0$, $T_{\text{surf}} = 0.0$), and use a Rayleigh number of 5×10^4 (Line 22) to drive convection. The key changes compared to Section 4.2.1 lie in how the activation energy is modeled. Instead of a single value, we define three distinct activation energy values:

- $E_{a1} = 7.5$ for the lower mantle (below 660 km),

```

1 from gadopt import *
2 import numpy as np
3 # set up the geometry and mesh
4 rmin, rmax, ncells, nlayers = 1.22, 2.22, 256, 64
5 rmax_earth = 6370 # Radius of Earth [km]
6 rmin_earth = rmax_earth - 2900 # Radius of CMB [km]
7 r_410_earth = rmax_earth - 410 # 410 radius [km]
8 r_660_earth = rmax_earth - 660 # 660 radius [km]
9 r_410 = rmax - (rmax_earth - r_410_earth) / (rmax_earth - rmin_earth)
10 r_660 = rmax - (rmax_earth - r_660_earth) / (rmax_earth - rmin_earth)
11 meshid = CircleManifoldMesh(ncells, radius=rmin, degree=2) # construct a circle mesh
12 mesh = ExtrudedMesh(meshid, layers=nlayers, extrusion_type='radial') # extrude into a cylinder
13 bottom_id, top_id = "bottom", "top"
14
15 # define the function spaces for storing and creating the fields (vector, scalar, mixed, etc)
16 .....
17 Q1 = FunctionSpace(mesh, "CG", 1) # scalar space for functions
18 R = FunctionSpace(mesh, "R", 0) # real number space
19 .....
20 u, p = split(z) # Returns symbolic UFL expression for u and p
21 # We next specify the important constants for this problem, and set up the approximation.
22 Ra = Function(R).assign(5e4) # Rayleigh number
23 approximation = BoussinesqApproximation(Ra)
24 delta_t = Constant(1e-7) # Initial time-step
25 timesteps = 20000 # Maximum number of timesteps
26
27 # We next set up the initial temperature field, which triggers four equidistant plumes in the domain
28 T = Function(Q, name="Temperature") interpolate(rmax - r + 0.02*cos(4*atan2(X[1], X[0])) * sin((r - rmin) * pi))
29
30 # define the linear components of the viscosity
31 def depth_activation_func(r, sharpness=60): #depth dependence (Eaz)
32     transition_660 = 0.5 * (1 + tanh((r - r_660) * sharpness)) #arctan function for smoother transitions
33     transition_410 = 0.5 * (1 + tanh((r - r_410) * sharpness))
34     return (5.0 * (rmax - r)) * (1-transition_660) + (1.0) * (transition_660 - transition_410) + (1.0) *
35     ↪ (transition_410) # piecewise constant activation profile
36 def temperature_activation_func(r, sharpness=60): #temperature dependence (EaT)
37     transition_660 = 0.5 * (1 + tanh((r - r_660) * sharpness))
38     transition_410 = 0.5 * (1 + tanh((r - r_410) * sharpness))
39     return (7.5)*(1-transition_660) + (5.5)*(transition_660 - transition_410) + (3.5)*(transition_410)
40     ↪ # piecewise constant activation profile
41 EaT = Function(Q1, name="Temperature Activation").project(temperature_activation_func(r, Ea1, Ea2, Ea3)) # EaT
42 mu = (exp(-EaT * T)) * depth_activation_func(r) # resulting viscosity field
43
44 # setup the nullspaces, bcs and solvers as in Listing 1
45 .....
46 for timestep in range(1, timesteps+1): #timestep loop
47     mu_field.interpolate(mu)
48     stokes_solver.solve() # Solve Stokes system
49     energy_solver.solve() # Temperature system
50     dtopo.interpolate(surface_force_solver.solve()/deltarho_g) #DT obs
51 .....
52 # save the states for inversion problem in checkpoint file
53 with CheckpointFile("Observed_State.h5", "w") as final_checkpoint:
54     final_checkpoint.write_mesh(mesh)
55     final_checkpoint.write_function([T, name="Temperature"], [z, name="Stokes"], [dtopo, name="Observed DT"], [u,
56     ↪ name="Observed Velocity"], [mu_field, name="Observed Viscosity"], [EaT, name="Observed T Activation"])]
```

Listing 7: Selected lines of Gadopt code. Synthetic data generation for depth-dependent rheology with layered activation energy.

- $E_{a2} = 5.5$ for the transition zone (410–660 km), and
- $E_{a3} = 3.5$ for the upper mantle (above 410 km).

The activation energy values are taken from Turcotte and Schubert (2002) and non-dimensionalized following the methods used in Ghelichkhan et al. (2024). They are smoothly incorporated into the model using hyperbolic tangent functions to avoid sharp discontinuities across mantle lay-

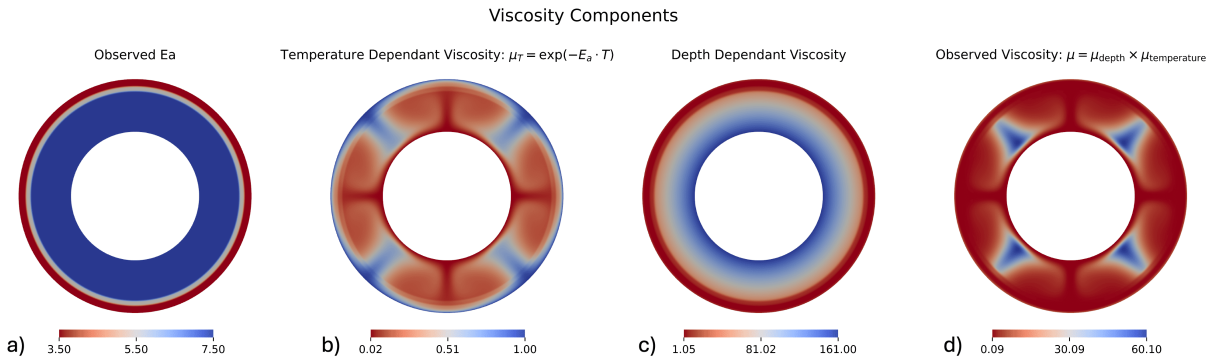


Figure 5.8: Components of the viscosity field: (a) temperature activation energy profile E_{aT} , (b) temperature-dependent viscosity, (c) depth-dependent viscosity, and (d) the resulting total viscosity $\mu(T, z)$.

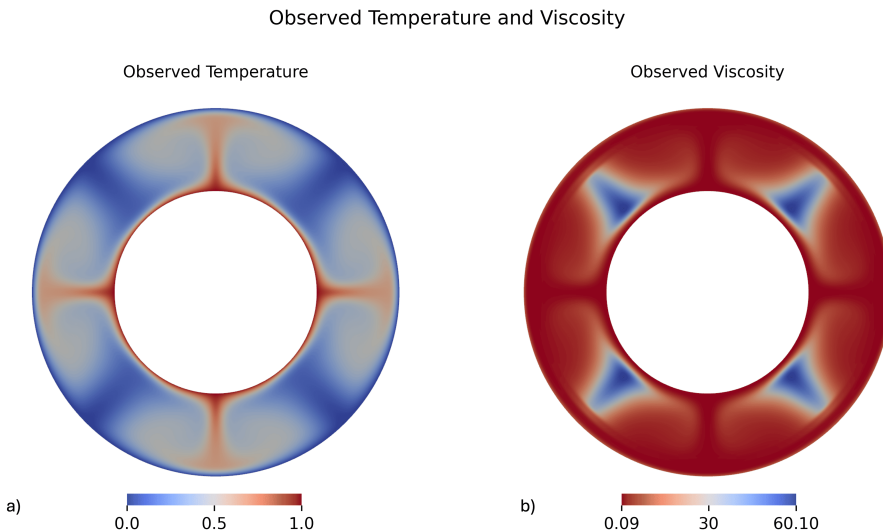


Figure 5.9: Final steady-state fields (observed) from the synthetic model: (a) temperature field and (b) total viscosity field.

ers (Lines 35–38). The total viscosity is thus computed as a combination of temperature and depth-dependent contributions:

$$\mu(T, r) = \exp(-E_{aT}(r) \cdot T) \cdot f_z(r), \quad (5.2)$$

where $E_{aT}(r)$ represents the piecewise activation energy profile across depth, and $f_z(r)$ is the depth-dependent factor controlled by E_{az} (Lines 30–34). The individual components of the viscosity field are shown in Figure 5.8. The governing equations are solved iteratively in a timestep loop (Lines 45–49), following the earlier methodology. At each step, viscosity is updated using the current temperature and depth, and the resulting surface stress yields dynamic

topography (DT_{obs}), while surface velocity (\mathbf{u}_{obs}) is extracted from the velocity field. Finally, the steady-state fields: temperature, velocity, dynamic topography, viscosity, and temperature activation energy are saved in a checkpoint file (Lines 52–54). These observed fields will serve as the reference data for the inversion in subsequent sections. The final steady-state temperature and total viscosity fields obtained from the synthetic run are shown in Figure 5.9.

5.2.2 Forward Model and Gradient Calculation

```

1 .....
2 def temperature_activation_func(r, Ea1, Ea2, Ea3, sharpness=75):           # activation field step function
3     transition_660 = 0.5 * (1 + tanh((r - r_660) * sharpness))
4     transition_410 = 0.5 * (1 + tanh((r - r_410) * sharpness))
5     return Ea1 * (1-transition_660) + Ea2 * (transition_660 - transition_410) + Ea3 * (transition_410)
6 # ----inverse crime----
7 # defining the controls
8 Ea1 = Function(R, name="Activation Energy 1").assign(4.0)
9 Ea2 = Function(R, name="Activation Energy 2").assign(3.0)
10 Ea3 = Function(R, name="Activation Energy 3").assign(2.0)
11
12 controls = [Control(Ea1), Control(Ea2), Control(Ea3)]    # defining the control for reduced functional
13 Ea = Function(Q1, name="Activation Energy").project(temperature_activation_func(r, Ea1, Ea2, Ea3))  # define the
   ↪ activation field
14 mu_temperature = Function(Q1, name="Temperature Dependant Viscosity").interpolate(exp(-Ea * T_obs)) # calculate
   ↪ temp viscosity
15 mu = mu_depth * mu_temperature
16 # calculate misfits and objective
17 .....

```

Listing 8: Selected lines from the updated Gadopt script showing the control setup and gradient computation for layered activation energy inversion, extending the framework from Listing 5.

In this synthetic test, we extend the inversion setup described in Section 5.1 to jointly recover three activation energy parameters corresponding to distinct mantle layers. The activation energy field is constructed as a piecewise profile (Lines 2–5) using a smooth transition function between the upper mantle, transition zone, and lower mantle. This field depends on three activation parameters $Ea1$, $Ea2$, and $Ea3$, which serve as the control parameters (Lines 7–10). The control variables are initialized with incorrect values: 4.0, 3.0, and 2.0, respectively (an inverse crime), and grouped into a control list (Line 12). The guess activation energy field is calculated (Line 13), and the temperature-dependent component of viscosity is computed using the known temperature field (Line 14). This component is then multiplied by the depth-dependent viscosity profile (see Figure 5.8) defined earlier in Listing 7 to obtain the total guess viscosity (Line 15). The forward Stokes equations are solved using this viscosity to compute predictions for dynamic topography and surface velocity, which are then compared to the synthetic obser-

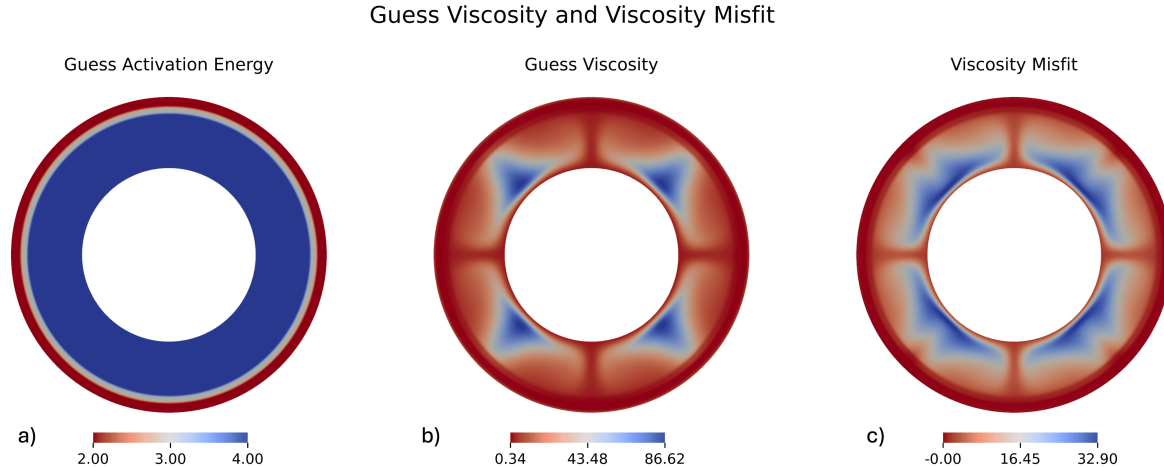


Figure 5.10: Initial guess fields based on incorrect activation energy values: (a) activation energy profile, (b) resulting viscosity field, and (c) viscosity misfit compared to the observed field. The misfit reveals significant deviations in both high and low viscosity regions, highlighting the need for correction through inversion.

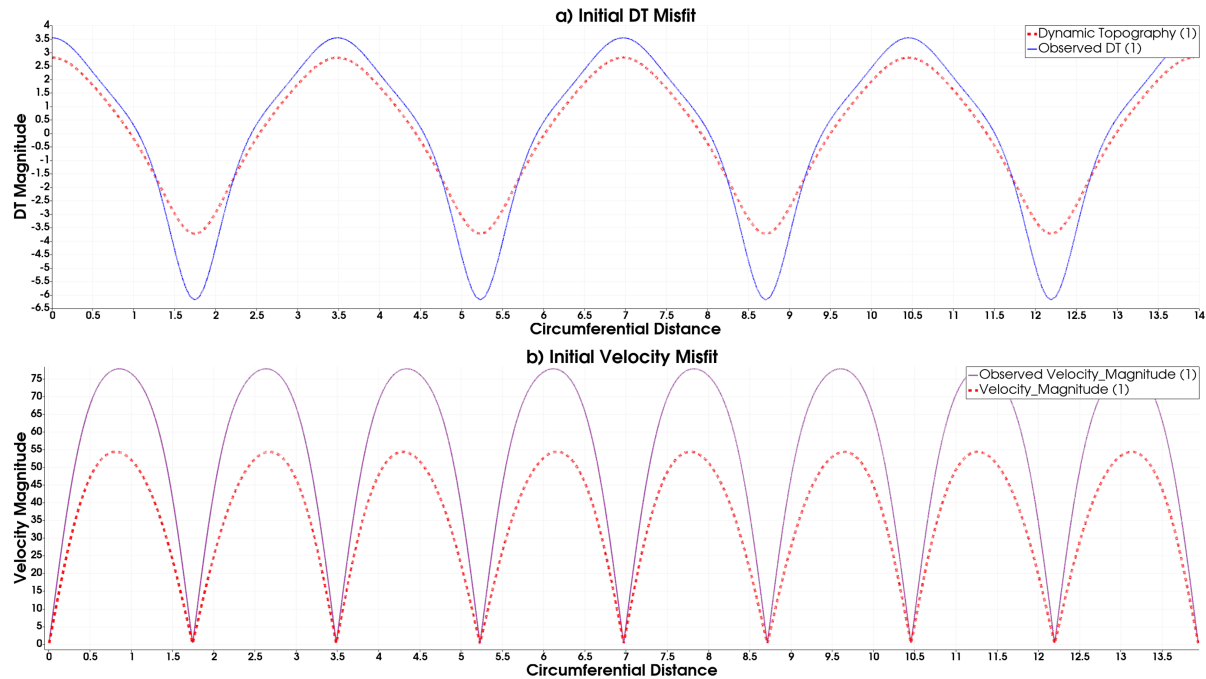


Figure 5.11: Initial misfit fields computed using the guessed activation energy profile: (a) dynamic topography misfit and (b) surface velocity misfit. The errors are particularly pronounced in regions with strong upwellings and downwellings, reflecting the impact of incorrect viscosity.

vations to evaluate the misfits, following the same procedure as in previous experiments. Since the inversion involves only three scalar parameters, no regularization terms are included, as in the earlier single-parameter case (Section 5.1).

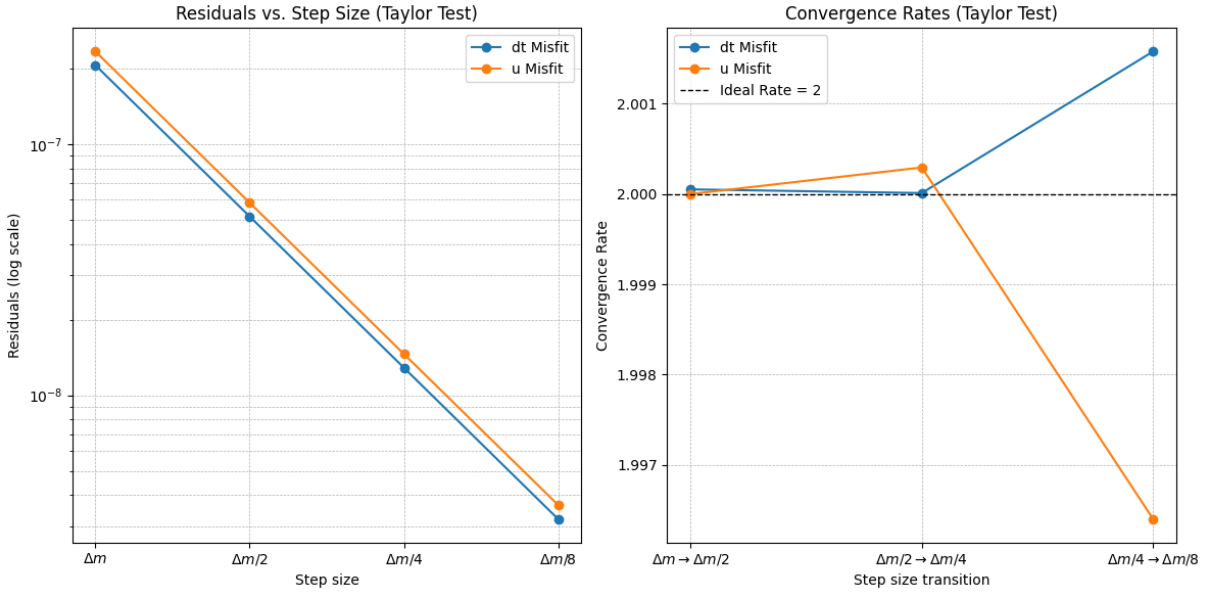


Figure 5.12: Second-order Taylor test confirming $\mathcal{O}(2.0)$ convergence of the gradient.

The objective functional is constructed as a weighted combination of the dynamic topography and surface velocity misfits:

$$J = \text{DT}_{\text{misfit}} + \alpha_u \cdot \mathbf{U}_{\text{misfit}}, \quad (5.3)$$

where α_u controls the relative influence of the velocity term. In this Inversion framework, α_u is set as a tunable parameter.

	Observed	Initial Guess	$\frac{d(J_{\text{DT}})}{dE_a}$	$\frac{d(J_{\text{U}})}{dE_a}$
Ea1	7.5	4.0	-0.1938	-0.6203
Ea2	5.5	3.0	0.0379	-0.0947
Ea3	3.5	2.0	0.0409	-0.3795

Table 5.2: Observed and initial guess values of activation energy, along with the initial gradients of the misfit terms with respect to each control parameter.

Initial guessed and observed values for the activation energy parameters, along with the computed gradients of each misfit term with respect to Ea1, Ea2, and Ea3, are summarized in Table 5.2. The gradient associated with the velocity misfit is significantly larger in magnitude compared to that of the dynamic topography, indicating that velocity provides a stronger constraint on the control parameters. This directional information informs the optimizer to increase

the activation energy values during inversion. These gradients are computed using the adjoint framework of Gadopt by defining a ReducedFunctional with respect to the three control parameters (Line 12). The computed gradient fields provide sensitivity information, indicating how each control activation energy parameter should be adjusted to minimize the misfits. To confirm the correctness of the computed gradients, we perform a second-order Taylor remainder test (Section 3.3). Figure 5.12 demonstrates that the convergence rate of the Taylor test is approximately $\mathcal{O}(2.0)$, as expected, validating the accuracy of the adjoint gradients.

5.2.3 Optimization and Inversion

```

1 # Define the bounds for the control
2 Ea_lb = Function(Ea1.function_space(), name="Lower_bound_Ea1").assign(1.0)
3 Ea_ub = Function(Ea1.function_space(), name="Upper_bound_Ea1").assign(10.0)
4
5 minimisation_problem = MinimizationProblem(reduced_functional, bounds=[[Ea_lb, Ea_ub],
6   [Ea_lb, Ea_ub], [Ea_lb, Ea_ub]])
7
8 optimiser = LinMoreOptimiser(minimisation_problem, minimisation_parameters, )
9 optimiser.run()

```

Listing 9: Setup and execution of the bounded nonlinear optimization for depth-dependent activation energy inversion, using three scalar control parameters corresponding to different mantle layers.

To minimize the objective functional, we employ the optimization framework using G-ADOPT. As in previous cases, we first define the reduced functional using the misfit terms and the three control parameters: E_{a1} , E_{a2} , and E_{a3} . The bounds for each control variable are set between 1.0 and 10.0 to prevent non-physical updates during the optimization. We then define a minimization problem using these bounds and pass it to the Lin-More optimizer from the Rapid Optimization Library (ROL), using standard settings for step length, trust region, and convergence tolerance. The relevant section of the optimization code is shown in Listing 9.

To assess how the relative weightings of dynamic topography and surface velocity influence inversion accuracy, we perform a parameter sweep over the velocity misfit weight $\alpha_u \in [0, 0.1, 1, 10, 100, 1000]$, while keeping $\alpha_{dt} = 1.0$ fixed in all cases. The convergence of the objective functional and the misfit terms is shown in Figure 5.13, and the corresponding activation energy evolution is shown in Figure 5.14.

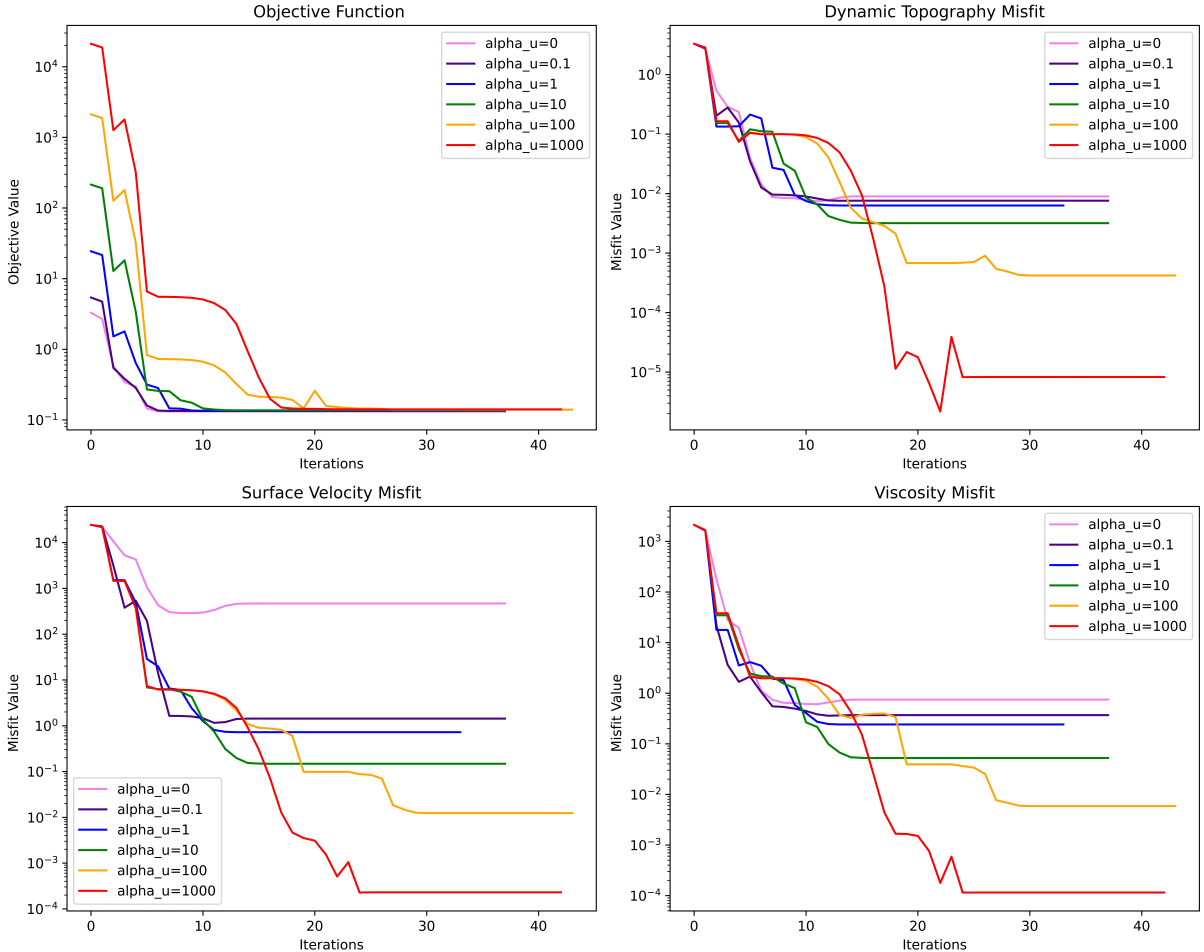


Figure 5.13: Convergence metrics for different values of α_u : (a) Objective functional, (b) Dynamic topography misfit, (c) Surface velocity misfit, and (d) Viscosity misfit.

5.2.4 Results

The results of this experiment show that the inversion successfully reconstructs the depth-dependent activation energy field, with some notable observations:

- **Effect of Velocity Misfit Weighting:** Increasing the weight on the surface velocity misfit (α_u) consistently improved the inversion performance. Among all cases tested, $\alpha_u = 1000$ yielded the most accurate reconstruction, achieving the lowest viscosity misfit (on the order of 10^{-4}) and best match with observed fields, as seen in Figures 5.13, 5.16.
- **Recovery of Layered Rheology:** The inversion successfully captured the distinct activation energy values for the three mantle layers. As shown in Figure 5.14, the lower mantle activation energy (E_{a1}) was accurately recovered in all cases, even when $\alpha_u = 0$, highlighting that dynamic topography alone is sensitive to deeper structures. However,

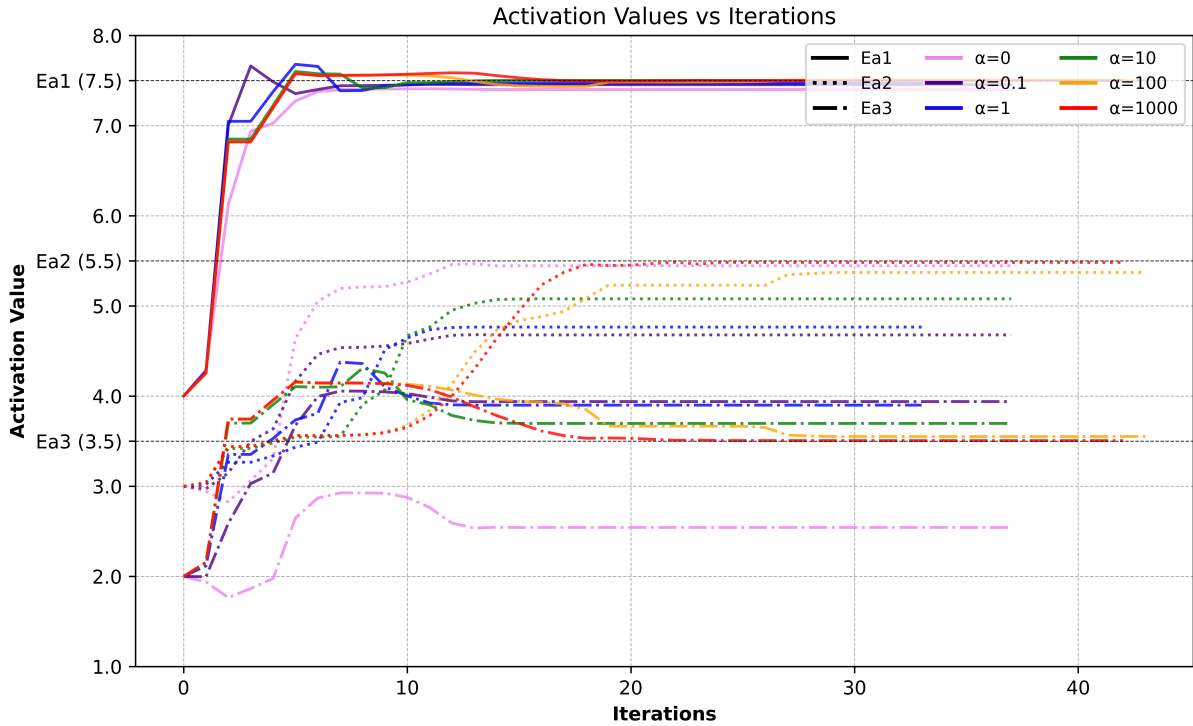


Figure 5.14: Evolution of activation energy values for the lower mantle (E_{a1}), transition zone (E_{a2}), and upper mantle (E_{a3}) across different α_u values. True values are shown as horizontal reference lines.

for the transition zone (E_{a2}) and upper mantle (E_{a3}), higher values of α_u were essential to achieve convergence towards the correct values.

- **Sensitivity to Observables:** These results confirm that surface velocity provides stronger constraints on shallow mantle rheology, while dynamic topography is more sensitive to deeper variations. This distinction likely arises from the longer-wavelength nature of dynamic topography, compared to the higher-frequency surface velocity signals.
- **Inversion Performance and Convergence:** The optimization was robust and converged effectively across all tested cases. Although $\alpha_u = 1000$ produced the best final result, the fastest initial convergence was observed for $\alpha_u = 0.1$. If the optimization were restricted to minimal steps, this case would yield a better result compared to the higher-weighted cases.
- **Fit to Observables:** Final dynamic topography and surface velocity predictions for the best-performing case ($\alpha_u = 1000$) are shown in Figure 5.15. The inversion captures the observed patterns accurately throughout the entire domain.
- **Reconstructed Viscosity Field:** The recovered viscosity structure (Figure 5.16) closely

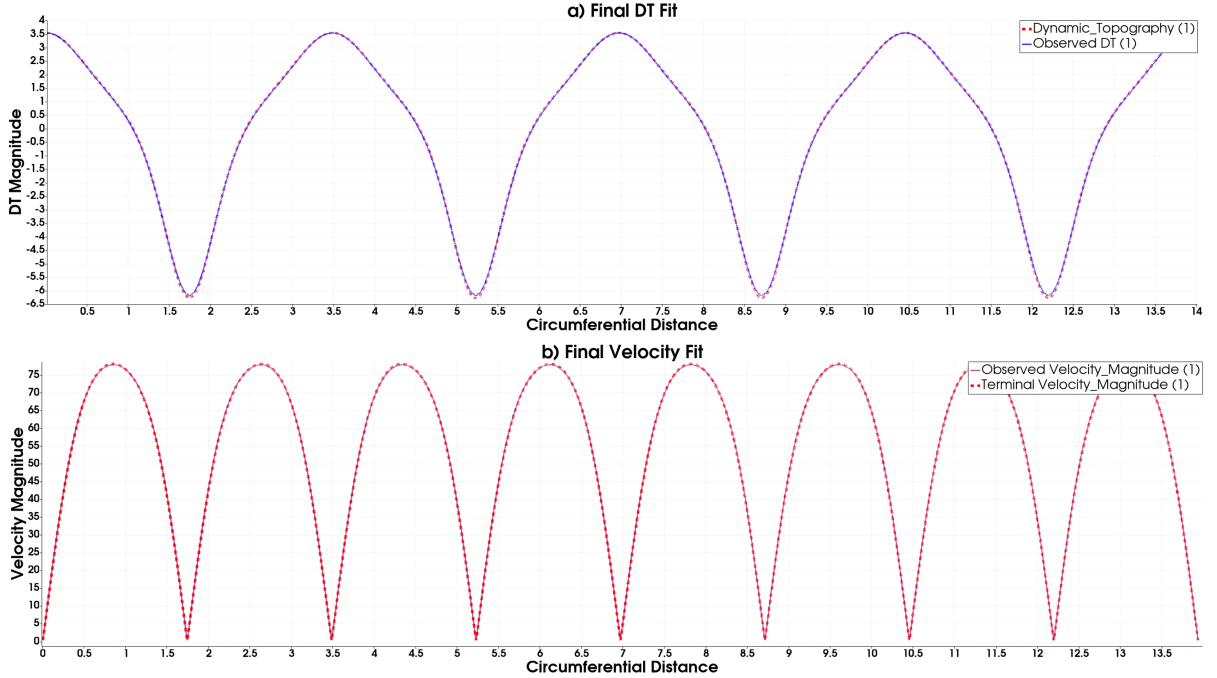


Figure 5.15: Final fit of surface observables for the best-performing inversion case ($\alpha_u = 1000$): (top) dynamic topography, (bottom) surface velocity. Observed and predicted fields are in close agreement.

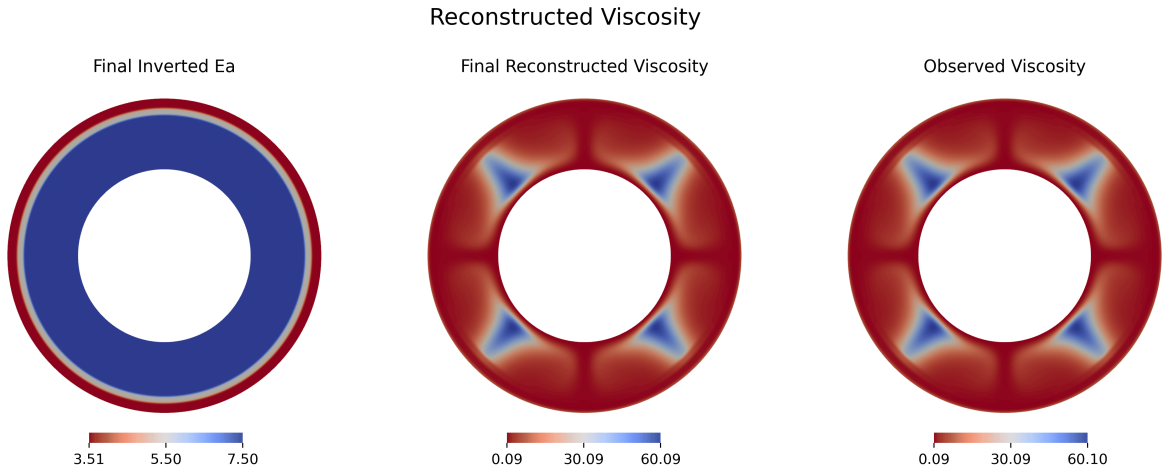


Figure 5.16: Reconstructed viscosity field for the best-performing case ($\alpha_u = 1000$). The match with the synthetic reference model confirms successful recovery of both deep and shallow mantle structures.

resembles the true synthetic model, capturing both high-viscosity and low-viscosity regions in appropriate mantle layers.

Overall, this test highlights the importance of including both surface velocity and dynamic topography when inverting for layered viscosity structure. While dynamic topography plays a key role in constraining deep mantle properties, surface velocity misfits are essential for recovering shallower structures, particularly in models with layered or discontinuous rheology. With

appropriate weighting, this joint inversion approach can accurately reconstruct complex mantle viscosity fields.

5.3 Model Configuration 5: Inversion Using Activation Energy with Fully Complex Mantle Rheology

In this inverse analyses, we aim to recover the full activation energy structure of the mantle by incorporating the full complex rheology (Tosi et al., 2015). Building upon the depth-dependent formulation from the previous case, we now introduce a plastic deformation component to the viscosity, making the problem significantly more complex and closer to physical reality.

The total viscosity in this setup is a combination of both linear and non-linear (plastic) components as described in Section 2.2:

$$\mu_{\text{lin}}(T, z) = \exp(-E_{aT} \cdot T + E_{az} \cdot z), \quad (5.4)$$

$$\mu_{\text{plast}}(\dot{\epsilon}) = \mu^* + \frac{\sigma_y}{\sqrt{\dot{\epsilon} : \dot{\epsilon}}}, \quad (5.5)$$

where $E_{aT} = \ln(\Delta\mu_T)$ and $E_{az} = \ln(\Delta\mu_z)$ represent the temperature and depth contributions to viscosity, respectively. The plastic term includes a yield stress σ_y and limits the effective viscosity under high strain-rate conditions. This relation ensures that the model captures both fluid-like behavior at low stress and plastic deformation at high stress. The domain is divided into three mantle layers, as described in the previous case (Section 5.2), with each layer assigned independent activation energy values for both temperature and depth dependence. In total, six scalar parameters are jointly inverted:

- $E_{aT,1}, E_{aT,2}, E_{aT,3}$: Temperature-dependent activation energy for the lower mantle, transition zone, and upper mantle.
- $E_{az,4}, E_{az,5}, E_{az,6}$: Depth-dependent activation energy for the same three regions.

This represents the most complex and geophysically realistic inversion setup considered so far,

```

1      .....
2  def temperature_activation_func(r, sharpness=60): # temperature dependence (EaT)
3      transition_660 = 0.5 * (1 + tanh((r - r_660) * sharpness))
4      transition_410 = 0.5 * (1 + tanh((r - r_410) * sharpness))
5      return (7.5)*(1-transition_660) + (5.5)*(transition_660 - transition_410) + (3.5)*(transition_410)
6
7  def depth_activation_func(r, sharpness=60): # depth dependence (EaZ)
8      transition_660 = 0.5 * (1 + tanh((r - r_660) * sharpness))
9      transition_410 = 0.5 * (1 + tanh((r - r_410) * sharpness))
10     return (5.0 * (rmax - r)) * (1-transition_660) + (1.0)*(transition_660 - transition_410) +
11         (1.0)*(transition_410)
12
13 # linear viscosity
14 mu_lin = (exp(-temperature_activation_func(r) * T)) * depth_activation_func(r)
15
16 # plastic viscosity component
17 eps = sym(grad(u))
18 epsii = sqrt(inner(eps, eps) + 1e-10)
19 sigma_y = 3.4e3 + 6.8e4 * (rmax - r) # yield stress with depth
20 mu_non_lin = 3.42 + (sigma_y / epsii) # mu_star = 3.42
21
22 # harmonic mean for final viscosity
23 mu = 2 / (1 / mu_lin + 1 / mu_non_lin)
24 .....

```

Listing 10: Selected implementation lines for computing the synthetic viscosity field with full rheology (Model Configuration 5).

aimed at testing whether the surface observables, dynamic topography and surface velocity, can meaningfully constrain both the thermal structure and compositional layering of the mantle.

5.3.1 Synthetic Data Generation

The synthetic setup for this case follows the same domain and convection model introduced in Sections 5.2.1 and 4.2.1. The annular domain extends from $r_{\min} = 1.22$ to $r_{\max} = 2.22$, corresponding to a non-dimensional mantle thickness of 1 and approximating Earth's surface-to-core-mantle-boundary geometry. Boundary conditions, initial plume-triggering temperature field (Equation 4.2), and Rayleigh number $\text{Ra} = 5 \times 10^4$ remain unchanged. The linear part captures temperature and depth dependence via six distinct activation energy values: three each for thermal and depth effects. The activation fields are implemented as smoothed step functions using hyperbolic tangent transitions to avoid numerical discontinuities. For example, the depth-dependent profile is constructed as:

$$E_{az}(r) = E_{az,1} \cdot (1 - \theta_{660}) + E_{az,2} \cdot (\theta_{660} - \theta_{410}) + E_{az,3} \cdot \theta_{410}, \quad (5.6)$$

where $\theta_{410} = \frac{1}{2}(1 + \tanh((r - r_{410}) \cdot s))$ represents the smooth transition centered at 410 km depth, and similarly θ_{660} is defined for the 660 km discontinuity. The parameter s controls

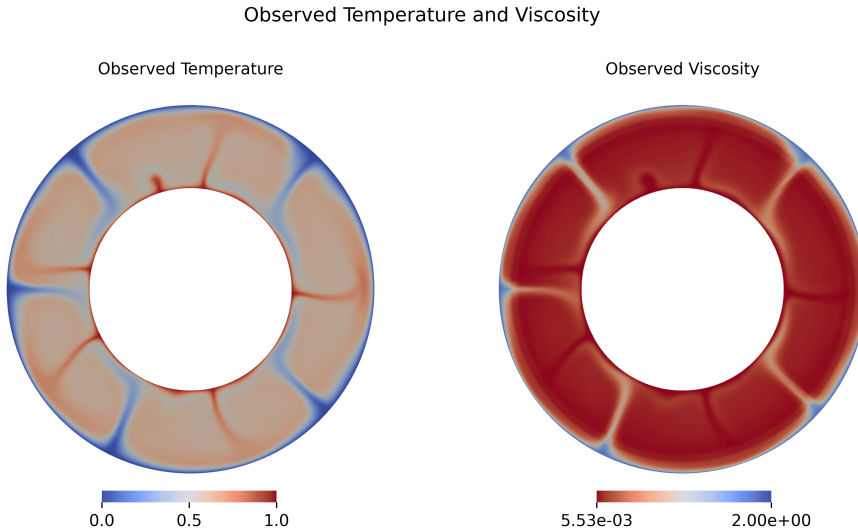


Figure 5.17: Synthetic reference fields generated using the fully complex mantle rheology model: (a) steady-state temperature field T_{obs} , and (b) total viscosity field μ_{obs} .

the sharpness of the transition. This formulation approximates the exponential depth-viscosity dependence $\mu(z) = \exp(E_{az} \cdot z)$ using layer-specific scaling that smoothly varies across mantle boundaries. We assume that the temperature field T is known and fixed, consistent with the approach taken in the previous two experiments. The plastic term accounts for non-linear strain-rate dependence using a depth-dependent yield stress and an effective viscosity floor, as described in Equations 2.9 and 2.10. The yield stress σ_y is assumed to scale with the cube root of the Rayleigh number, while the lower bound μ^* reflects its inverse dependence on strain rate. These scalings are consistent with the physical formulations discussed in Reuber et al. (2018), and the parameter values used here are based on those from Coltice et al. (2017). The implementation of these components is provided in Listing 10, and the resulting activation energy and viscosity fields are illustrated in Figure 5.18. The final viscosity field is defined as the harmonic mean of the linear and plastic terms. Once the model reaches a steady-state, we extract the surface observables: temperature T_{obs} , dynamic topography DT_{obs} , and surface velocity \mathbf{u}_{obs} , which together form the synthetic reference dataset for the inversion. The corresponding steady-state temperature and viscosity fields are shown in Figure 5.17.

5.3.2 Forward Model and Gradient Calculation

Similar to the previous tests, we perform a joint inversion in \mathbb{R} -space for the six activation energy parameters that control both temperature and depth dependence of viscosity (see Sec-

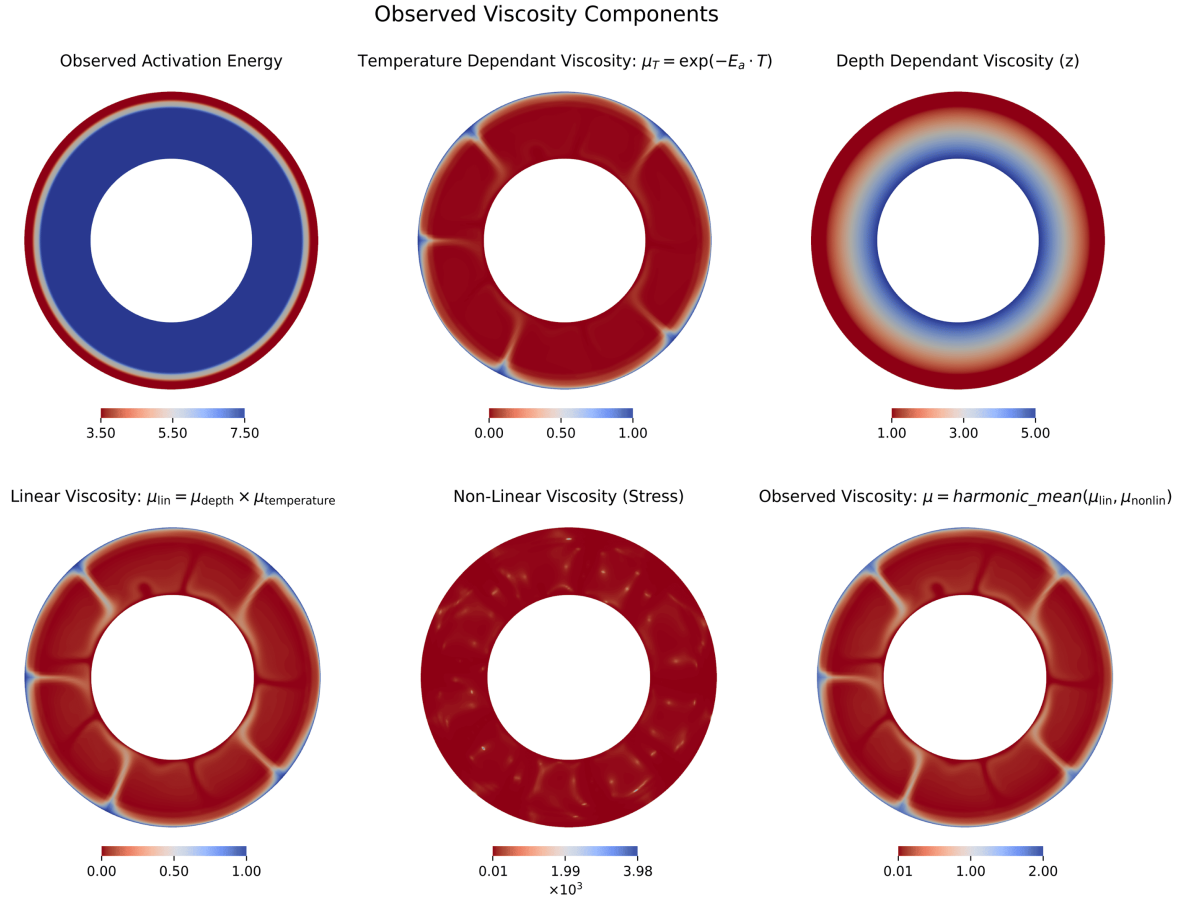


Figure 5.18: Components of the viscosity structure used in the fully complex model. (a) combined activation energy field, (b) temperature-dependent viscosity component, (c) depth-dependent viscosity component, (d) linear viscosity μ_{lin} , (e) non-linear plastic viscosity μ_{plast} , and (f) final effective viscosity μ obtained as the harmonic mean of the linear and plastic components.

```

1 .....
2 # guess activation energy values
3 Ea1 = Function(R, name="Activation Energy 1").assign(3.0)      #Temp activation guess(lower mantle)
4 Ea2 = Function(R, name="Activation Energy 2").assign(3.0)      #Temp activation guess(transition zone)
5 Ea3 = Function(R, name="Activation Energy 3").assign(3.0)      #Temp activation guess(upper mantle)
6 Ea4 = Function(R, name="Activation Energy 4").assign(3.0)      #Depth activation guess(lower mantle)
7 Ea5 = Function(R, name="Activation Energy 5").assign(3.0)      #Depth activation guess(transition zone)
8 Ea6 = Function(R, name="Activation Energy 6").assign(3.0)      #Depth activation guess(upper mantle)
9 # define the control for reduced functional
10 controls = [Control(Ea1), Control(Ea2), Control(Ea3), Control(Ea4), Control(Ea5), Control(Ea6)]
11 # calculate the temperature dependant viscosities
12 mu_temperature = Function(Q1, name="Temperature Dependant Viscosity").project(exp(temperature_activation_func(r,
13     ↪ Ea1, Ea2, Ea3) * T_obs))
14 mu_lin = Function(Q1, name="Linear Viscosity").project(mu_depth * mu_temperature)
15 # harmonic mean of the linear and non-linear components
16 mu = Function(Q1, name="Viscosity").interpolate(2 / (1 / mu_lin + 1 / mu_nonlin))
17 .....
18 # calculate misfits and objective

```

Listing 11: Selected lines from the updated Gadopt script showing the initial guess and control setup. In this case, we begin with incorrect initial guesses by assigning a value of 3.0 to each of the six activation energy parameters: E_{a1}, E_{a2}, E_{a3} (temperature-dependent) and E_{a4}, E_{a5}, E_{a6}

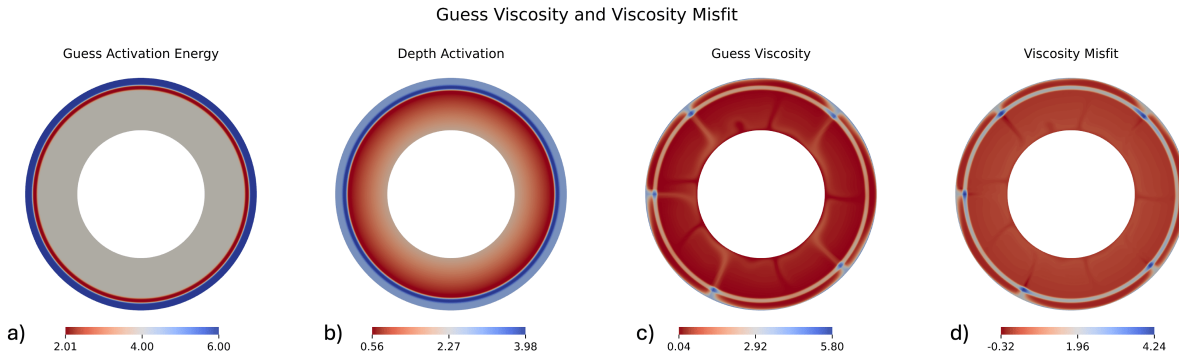


Figure 5.19: Viscosity field comparison for the initial guess in Model Configuration 5: (a) incorrect temperature activation energy field, (b) guessed depth activation energy field, (c) resulting viscosity field, and (d) resulting viscosity misfit. The largest discrepancies appear in shallow regions and across mantle interfaces.

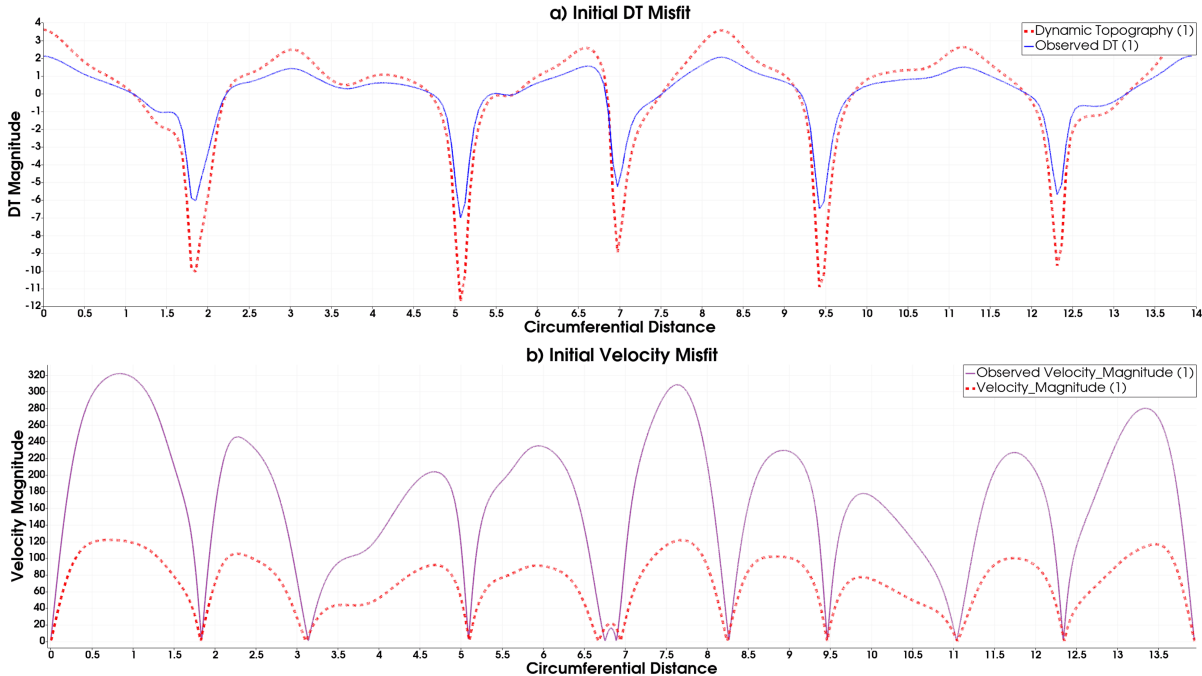


Figure 5.20: Initial misfit fields from incorrect viscosity: (a) dynamic topography misfit, (b) surface velocity misfit. High errors are observed near strong gradients, reflecting poor agreement with the reference solution.

(depth-dependent). Using these guessed values, we compute the initial viscosity field (see Figure 5.19) and solve the forward Stokes system to evaluate the corresponding surface observables. These predictions are then compared against the synthetic reference fields to compute the misfit in both dynamic topography and surface velocity as shown in Figure 5.20. To evaluate the direction and sensitivity of the inversion, we compute the initial gradients of the objective functional with respect to each control parameter. These gradients indicate how the objective

changes with increasing activation energy in each layer and guide the optimization process. The values are listed in Table 5.3.

Parameter	Observed	Initial Guess	$\frac{dJ_{DT}}{dE_a}$	$\frac{dJ_U}{dE_a}$
E_{a1}	7.5	3.0	-0.231	-0.612
E_{a2}	5.5	3.0	0.053	-0.125
E_{a3}	3.5	3.0	0.071	-0.314
E_{a4}	5.0	3.0	-0.268	-0.382
E_{a5}	1.0	3.0	0.044	-0.193
E_{a6}	1.0	3.0	0.019	-0.239

Table 5.3: Initial guesses, observed values, and gradients of the dynamic topography and surface velocity misfit terms with respect to each activation energy parameter.

As seen in the table, surface velocity misfit gradients are negative across all parameters, pointing in the correct descent direction, while the dynamic topography gradients are mixed. This behavior is consistent with earlier findings and reinforces the stronger sensitivity of velocity fields to upper mantle structures. To verify the correctness of the computed gradients, we perform a Taylor convergence test, which confirms the expected second-order accuracy, i.e., $\mathcal{O}(2.0)$ convergence.

5.3.3 Optimization and Inversion

```

1 # Define the bounds for the control
2 Ea_lb = Function(Ea1.function_space(), name="Lower_bound_Ea1").assign(1.0)
3 Ea_ub = Function(Ea1.function_space(), name="Upper_bound_Ea1").assign(10.0)
4
5 minimisation_problem = MinimizationProblem(reduced_functional, bounds=[[Ea_lb, Ea_ub],
6   [Ea_lb, Ea_ub], [Ea_lb, Ea_ub], [Ea_lb, Ea_ub], [Ea_lb, Ea_ub]])
7 optimiser = LinMoreOptimiser(minimisation_problem, minimisation_parameters,)
8 optimiser.run()

```

Listing 12: Selected lines from the optimization setup in Model Configuration 5, showing the definition of uniform bounds for the six activation energy parameters and the use of the `LinMoreOptimiser` from `Gadopt` to minimize the objective functional.

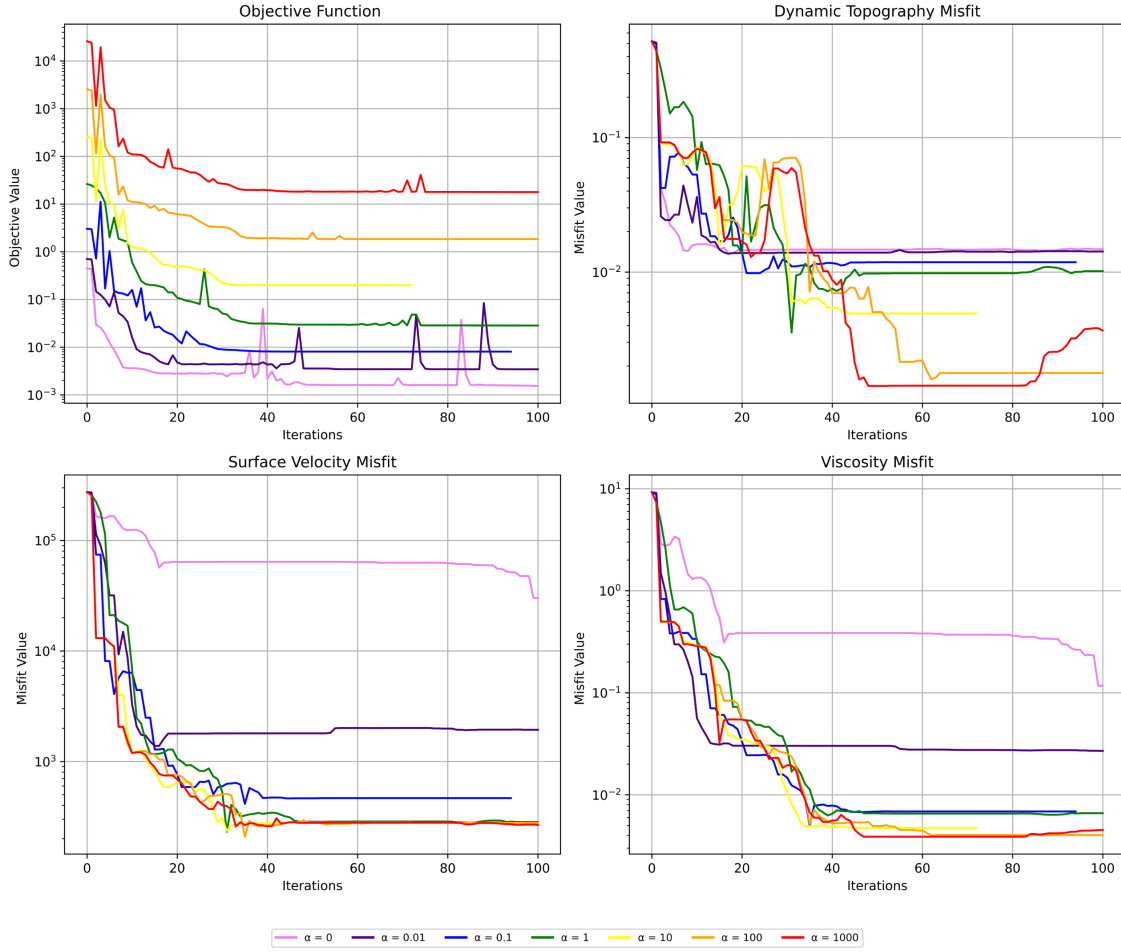


Figure 5.21: Summary of inversion performance across different values of the velocity misfit weight α_u . Plots show the evolution of the total objective functional, final dynamic topography misfit, surface velocity misfit, and viscosity misfit.

To recover all six activation energy parameters, we define a reduced functional based on the objective function and pass it to the G-ADOPT optimization framework (Listing 11). As in previous experiments, bounds are imposed on the control parameters to prevent non-physical values. The optimization is carried out using the Lin-More algorithm from the Rapid Optimization Library (ROL), with the required minimization parameters specified (see Listing 12). To assess the influence of the relative weighting of velocity and dynamic topography misfits, we perform a parameter sweep over the velocity misfit weight α_u , while fixing the dynamic topography weight to 1.0. Specifically, we test seven different values of $\alpha_u \in [0, 0.01, 0.1, 1, 10, 100, 1000]$, and run separate inversion simulations for each. This helps us identify the weighting that yields the best fit to the synthetic observations. The control parameters in each case are the six scalar activation energies.

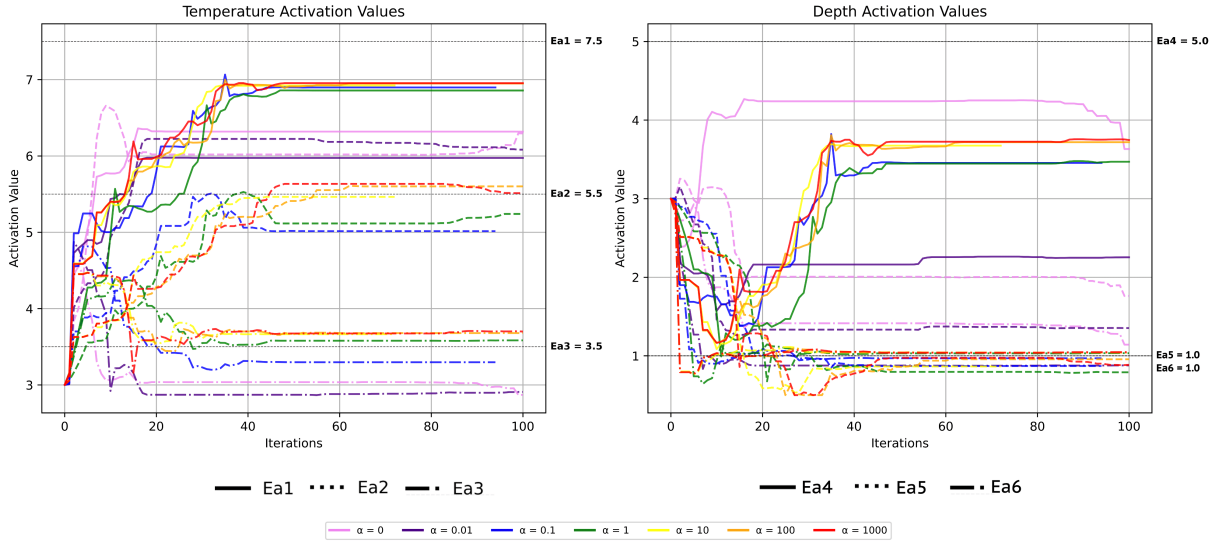


Figure 5.22: Inversion history of the six activation energy parameters across different values of α_u .

5.3.4 Results

This case study produced several notable results that differ from previous cases involving simpler rheologies. The inclusion of both depth-dependent and plastic components leads to a more geophysically realistic inversion scenario, which also modifies the sensitivity of surface observables to internal rheological structure. A detailed analysis of the inversion outcomes is provided below:

- **Misfit Sensitivity:** From Figure 5.21, we see that higher values of surface velocity weight ($\alpha_u = 10, 100, 1000$) lead to better minimization of the objective function and both misfits. This is different from the earlier case, where dynamic topography alone was often enough to constrain deep mantle structure (Section 5.2.4). In this setup, both observables are needed to get a good result.
- **Activation Energy Recovery:** The temperature-based parameters (E_{a1}, E_{a2}, E_{a3}) and the depth-based ones (E_{a4}, E_{a5}, E_{a6}) generally move toward their true values. The best match is obtained for $\alpha_u = 100$, especially in the upper mantle and transition zone. However, E_{a1} and E_{a4} , corresponding to the lower mantle, plateau below their targets. This could be due to reduced sensitivity of surface observables to deeper non-linear structures, the added difficulty of jointly recovering six control parameters, or conservative convergence thresholds in the optimizer that halt updates once the overall misfit is sufficiently minimized.

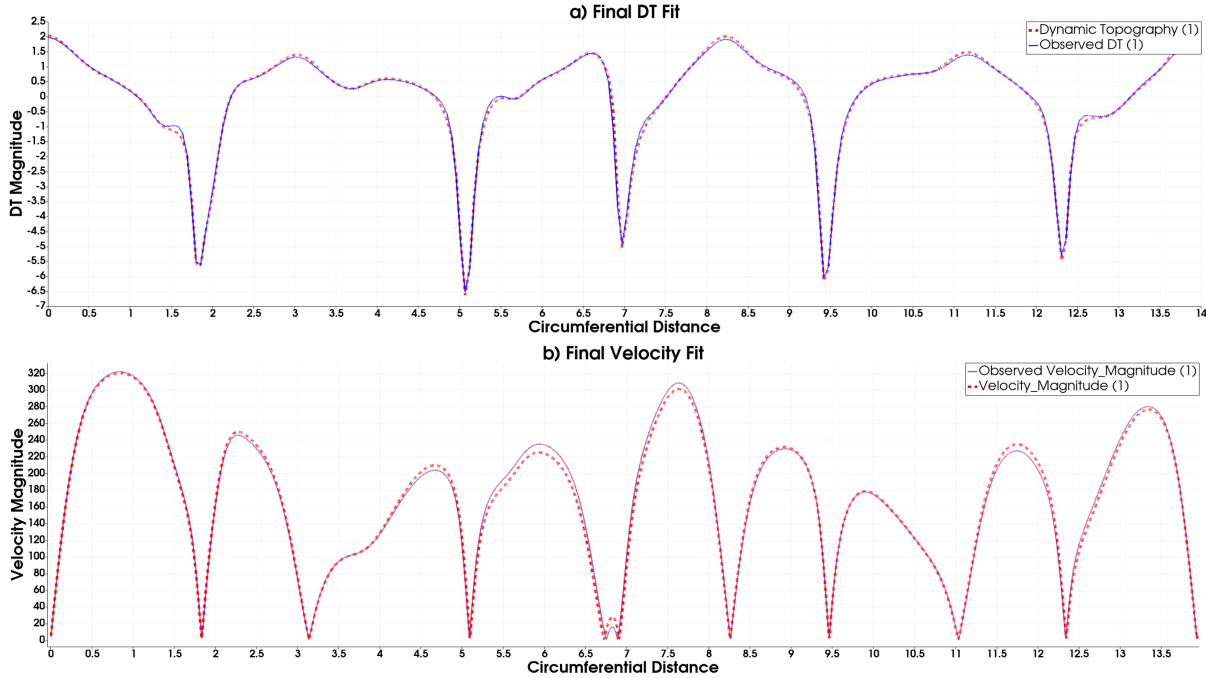


Figure 5.23: Final fits to observed surface fields in the best-performing inversion case ($\alpha_u = 1000$). (Top) dynamic topography and (bottom) surface velocity. Predicted and observed fields show near-perfect alignment.

- **Role of Dynamic Topography:** The inclusion of dynamic topography remains critical, particularly for constraining deeper mantle behavior. While surface velocity helps improve recovery in shallower layers, dynamic topography adds complementary sensitivity in regions dominated by plastic yielding. Its effectiveness is amplified when combined with surface velocity data.
- **Joint Contribution of Observables:** In contrast to simpler rheological cases, neither dynamic topography nor surface velocity alone can give good recovery of all parameters. The best results are only obtained when both observables are used together. For example, with $\alpha_u = 0$ (no velocity), the inversion struggles for all layers.
- **Misfit Trends:** Over 100 iterations, surface velocity and viscosity misfits reduce by over three orders of magnitude for most of the cases. This supports the effectiveness of the optimization strategy, especially when appropriate weights are assigned to the observables.
- **Final Fits and Reconstructed Viscosity:** The final predictions of dynamic topography and surface velocity for the best-performing case ($\alpha_u = 100$) are shown in Figure 5.23, and they match the observed data closely across the domain. The reconstructed viscosity field in Figure 5.24 shows that the inversion successfully captures the full mantle

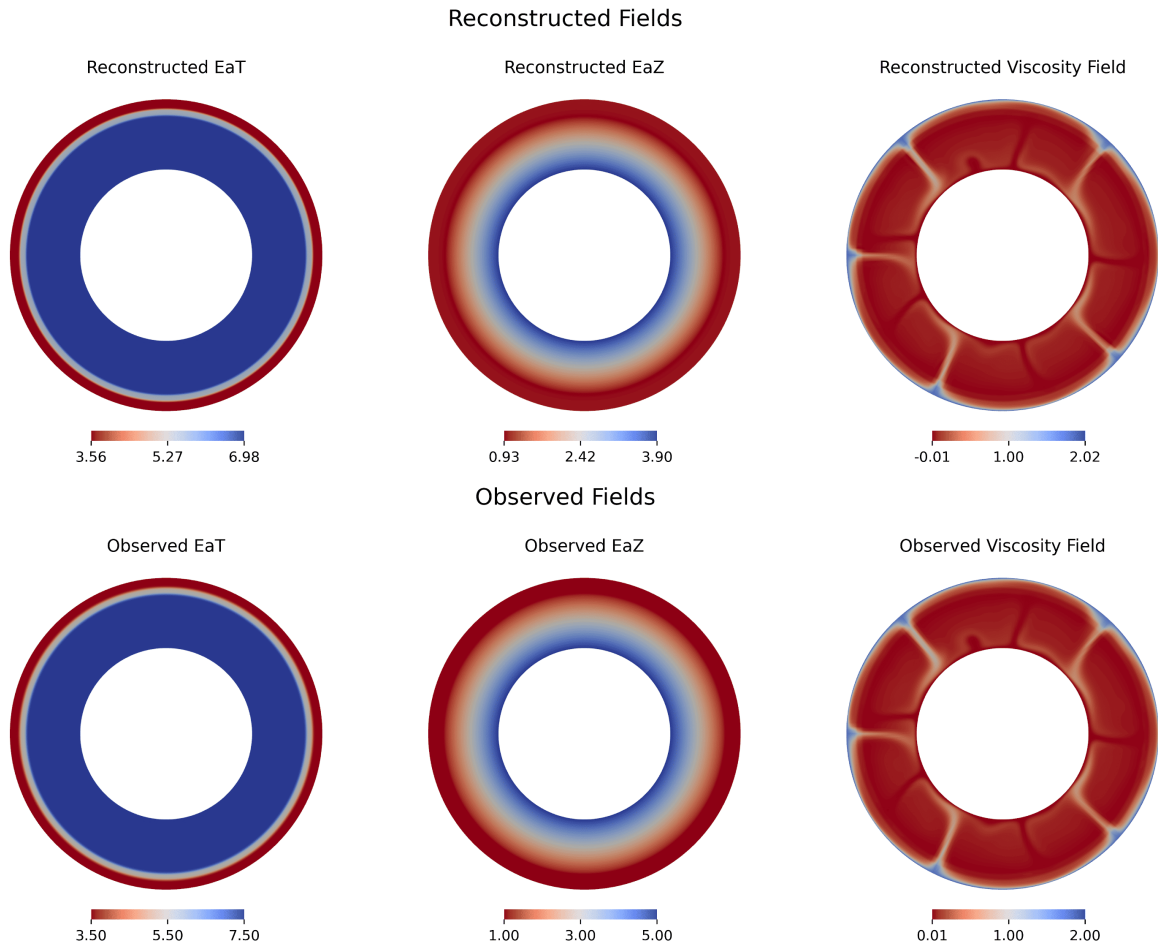


Figure 5.24: Reconstructed effective viscosity field for the best inversion case ($\alpha_u = 100$). The recovered viscosity shows excellent agreement with the synthetic reference model across the entire mantle.

structure, including both shallow and deep regions, even with the added complexity of non-linear rheology and sharp layer transitions.

This analysis shows that using both dynamic topography and surface velocity together is crucial for recovering complex mantle rheology. The inversion framework performs well even in the presence of strong non-linear behavior and discontinuities, though further improvements may require fine-tuning the optimizer and incorporating appropriate regularization.

Chapter 6

Conclusion and Future Work

6.1 Summary

This thesis develops and applies an adjoint-based geodynamic inversion framework to investigate the sensitivity of surface observables, primarily dynamic topography, to different components of mantle flow. The central motivation of this work is to better constrain mantle rheological properties, particularly viscosity variations, which control a wide range of geodynamic and surface processes such as glacial isostatic adjustment, basin subsidence, and long-term sea-level change (Mitrovica and Forte, 2004; Flament et al., 2013). Among surface observables, dynamic topography offers a valuable constraint on mantle structure and flow, particularly in regions where seismic tomography has limited resolution (Hoggard et al., 2016). To achieve this, we utilize the G-ADOPT framework (Ghelichkhan et al., 2024), which combines Firedrake (Rathgeber et al., 2016), Dolfin-Adjoint (Mitusch et al., 2019), and the Rapid Optimization Library (ROL) (Trilinos Team, 2024). This platform automates the derivation of discrete adjoints, enabling scalable, reproducible inversions of mantle properties. Our setup solves the incompressible Stokes and heat equations in a 2D annular domain, which is an idea trade-off between computational efficiency and the ability to resolve both radial and lateral variations in mantle structure. Inversions are performed in log-viscosity space for numerical stability and are regularized with both damping and smoothing terms to stabilize the optimization process (Chapter 4).

We conduct five synthetic tests with increasing model complexity (Chapters 4, 5). These include direct inversion of viscosity, temperature field recovery, and activation energy inversion under both depth- and temperature-dependent assumptions, culminating in a joint inversion under visco-plastic rheology. Our results are evaluated in terms of objective function reduction, misfit convergence, and recovery of physical fields (viscosity, temperature, and activation energy).

6.2 Contributions and Key Findings

This thesis introduces a robust adjoint based inversion framework to recover complex mantle rheologies using surface observables. The key novelty lies in using joint inversion of dynamic topography and surface velocity to analyse and exploit their sensitivity to different components of mantle flow, enabling constraints on both depth dependent and temperature dependent variations in activation energy under a fully non linear, visco plastic rheology. To our knowledge, this is one of the first studies to perform high-dimensional adjoint-based inversion accounting for both radial and lateral variations in mantle properties, using a 2D annular domain that approximates spherical shell geometry. While most prior work has focused on radially symmetric (1D) profiles and simplified Newtonian rheologies (Euen et al., 2023; Monnereau and Quéré, 2001), this study incorporates spatially variable, temperature- and stress-dependent viscosity, including depth-dependent yielding. The annular geometry facilitates sensitivity analysis across multiple directions, bridging the gap between idealized models and more realistic mantle convection scenarios. This geometry allows us to directly evaluate how dynamic topography responds to different wavelengths and rheological features of mantle flow, providing insight into its ability to resolve structures at various depths. We also show that dynamic topography inversions are inherently non-unique: different rheological models can yield equally good fits to observed surface signals, particularly when surface velocity data are excluded or when regularization exerts a dominant influence on the solution. This highlights the necessity of using joint constraints and appropriately tuning the objective functional. Furthermore, the systematic sensitivity analyses examine how variations in control parameters such as activation energy, temperature, and viscosity impact the resulting surface observables. These analyses demonstrate that dynamic topography is most responsive to long wavelength structures and deep mantle flow, whereas surface velocity offers sharper constraints on shallow, high frequency features.

The insights from our systematic suite of five experiments are summarized in Table 6.1. Major conclusions include:

- **Dynamic topography is highly sensitive to deep mantle structure**, especially when the forward model includes non-linear viscosity. However, its constraining power alone is not sufficient for recovering shallow features or multi-parameter fields. In contrast, **surface velocity provides complementary sensitivity to shallower layers** and is crucial

Model Configuration	Setup and Assumptions	Key Results
Config. 1	Inversion for viscosity field; temperature fixed. Layer-averaged initial guess.	Surface velocity misfit had stronger impact than dynamic topography. Regularization was critical. Major structures recovered, but small-scale details were missed.
Config. 2	Inversion for temperature field; viscosity computed from Arrhenius law.	Highly under-constrained. Misfit reduced, but reconstructed temperature field did not match the truth. Demonstrates limitations of dynamic topography inversion for complex fields.
Config. 3	Inversion for uniform activation energy; known temperature field.	Fast convergence across all values of α_u . Accurate recovery even from poor initial guesses. Velocity misfit weight improved performance.
Config. 4	Layered activation energy inversion (depth-dependent); 3 parameters.	Dynamic topography alone constrained lower mantle; velocity data essential for upper layers. Best results achieved with $\alpha_u = 1000$. Clear stratification captured.
Config. 5	Joint inversion for 6 parameters (depth and temperature dependent), with non-linear (plastic) rheology.	Best performance with $\alpha_u = 100$. Both observables needed together. Lower mantle recovery weaker due to sensitivity loss. Complex rheology successfully reconstructed.

Table 6.1: Summary of model configurations, assumptions, and main findings.

for accurate inversion of mantle properties.

- **The joint use of dynamic topography and surface velocity consistently yields the best inversion results across all tests.** Regardless of model complexity, combining both observables improves convergence and parameter recovery. The relative weight assigned to surface velocity (α_u) has a strong influence on the optimization outcome, with values

like $\alpha_u = 10, 100, 1000$ producing the most accurate reconstructions in multiple cases (Synthetic Tests 1, 3, 4, and 5).

- **Simple cases with low-dimensional controls (e.g., a single uniform activation energy)** converge rapidly and reliably, even from poor initial guesses (Model Configuration 3). These serve as useful benchmarks for testing inversion workflow and optimizer tuning.
- **Inversion in log space (E_a) simplified the optimization and improved numerical stability**, especially in cases involving large viscosity contrasts and non-linear rheology. Working in log space allowed smooth convergence and more accurate recovery across several orders of magnitude in viscosity.
- **Not all inversions are well-constrained.** Cases attempting to recover high-dimensional fields (e.g., temperature in Model Configuration 2) using only surface observables failed to produce physically meaningful results, even when misfits decreased. This highlights the non-uniqueness of the inverse problem and the necessity for richer data constraints in such scenarios.
- **Regularization plays a vital role** in stabilizing the inversion process, particularly in under-constrained problems. By penalizing sharp gradients and large deviations, regularization helps suppress non-physical oscillations and avoids overfitting to noisy or sparse data. This was clear in Model Configuration 1, where smoothing and damping helped avoid unrealistic fine-scale variations and ensured geologically plausible viscosity fields despite limited constraints.
- **The inversion remains robust under complex rheology.** Even in the most challenging case (Model Configuration 5), the framework successfully recovered essential features, albeit with reduced accuracy in the lower mantle due to weak sensitivity and multiple controls.
- **G-ADOPT, powered by Firedrake and dolfin-adjoint, proved highly effective for large-scale inversion problems.** The ease of defining variational problems, automatic adjoint generation, and seamless integration with optimization routines allowed for rapid experimentation and accurate sensitivity computation.

These findings confirm the potential of adjoint-based inversion for recovering Earth's internal structure and emphasize the importance of combining multiple observables and realistic rheologies.

6.3 Limitations of the Study

While this study demonstrates the effectiveness of adjoint-based inversion for recovering mantle rheology, several limitations should be noted:

- **Synthetic Setup and Inverse Crime:** All inversion experiments were conducted using synthetic datasets generated from known reference models. Although this allows systematic testing, using the same model setup for both forward and inverse problems may lead to inverse crime and overstate inversion accuracy.
- **Uncertainty in Input Fields:** The inversion assumes perfect knowledge of temperature when recovering activation energy fields. In reality, seismic tomography-derived temperatures carry significant uncertainties due to limited resolution and trade-offs between thermal and compositional signals.
- **Ambiguity in Viscosity Reconstructions:** Viscosity remains poorly constrained because it depends on several factors that are difficult to observe, such as grain size, water content, and strain rate. Even with joint inversion, multiple rheological models can match the surface data equally well.
- **Neglect of Time Dependence:** The model assumes instantaneous Stokes flow and thermal steady state. While suitable for first-order analyses, it does not account for time-dependent processes such as slab sinking or plume evolution.
- **Limited Observables:** Only surface dynamic topography and velocity are used. These provide valuable constraints but are limited in resolution as velocity is mostly sensitive to shallow features, while topography has better sensitivity at depth.
- **Simplified Geometry:** The 2D annular domain approximates spherical geometry but cannot represent full 3D mantle dynamics or plate boundaries.

- **Moderate Rayleigh Number:** The Rayleigh number used here is lower than realistic Earth values due to computational cost. Simulating higher convective vigor would require finer meshes and significantly more resources.
- **High-Dimensional Optimization:** As the number of control parameters increases, optimization becomes more sensitive to initial conditions and regularization. Multiple local minima may yield different, but equally plausible, solutions, highlighting the need for uncertainty quantification.

6.4 Future Directions

While this work presents a solid foundation for adjoint-based mantle rheology inversion, there are several promising directions that could improve its applicability. One major assumption in our experiments is that present-day temperature (or tomography-derived temperature) is known. In practice, however, seismic tomography carries significant uncertainties, especially in amplitude and depth sensitivity (Rawlinson et al., 2014; Fichtner et al., 2024). A natural next step would be to explore how such uncertainties in temperature fields affect inversion outcomes by introducing noise or perturbations to the initial thermal structure and propagating that uncertainty through the inversion (Alekseev and and, 2003). This could help assess how robust the recovered viscosity is and whether certain parts of the mantle are more reliably constrained than others.

Another direction is to link this numerical approach with analytical sensitivity studies that have been done previously. These studies have shown, for example, that dynamic topography is most sensitive to long-wavelength structures and deep mantle flow (Hoggard et al., 2016; Hager and Richards, 1989). Comparing numerical sensitivity patterns from our framework with these analytical results would provide useful benchmarks and support more informed interpretation of the inversion outcomes. We also see potential in extending the current model to include other surface constraints such as gravity anomalies, geoid height, or even time-dependent signals like post-glacial rebound. These could offer complementary sensitivity and help reduce the non-uniqueness in inversion. From a computational perspective, moving from 2D annular geometry to full 3D spherical shells would be an important but challenging step. It would allow us to test more realistic Earth scenarios, including plate boundaries, phase transitions, and lateral

compositional heterogeneity, all of which are known to influence mantle flow and viscosity structure but were beyond the scope of this thesis.

Code Availability

The software used to conduct the adjoint-based inversions described in this thesis is openly available. The numerical methods, simulations, and inversion workflows were implemented using the **Firedrake** and **G-ADOPT (Geoscientific ADjoint Optimisation PlaTform)** frameworks. All scripts, notebooks, and relevant configurations can be accessed through the GitHub repository:

- <https://github.com/prahlad-mittal/Dynamic-Topography-Adjoints>

Further information on Firedrake and G-ADOPT is available at:

- **Firedrake:** <https://www.firedrakeproject.org>
- **G-ADOPT:** <https://gadopt.org/>

For additional details, questions, or assistance regarding the code and methodology presented, please contact the author directly at prahlada_vm@es.iitr.ac.in.

References

- Al-Attar, D., Tromp, J., 10 2013. Sensitivity kernels for viscoelastic loading based on adjoint methods. *Geophysical Journal International* 196 (1), 34–77. URL <https://doi.org/10.1093/gji/ggt395>
- Alekseev, A., and, I. N., 2003. Calculation of uncertainty propagation using adjoint equations. *International Journal of Computational Fluid Dynamics* 17 (4), 283–288. URL <https://doi.org/10.1080/1061856031000113644>
- Alnæs, M. S., Logg, A., Ølgaard, K. B., Rognes, M. E., Wells, G. N., Mar. 2014. Unified form language: A domain-specific language for weak formulations of partial differential equations. *ACM Trans. Math. Softw.* 40 (2). URL <https://doi.org/10.1145/2566630>
- Austermann, J., Mitrovica, J. X., Huybers, P., Rovere, A., 2017. Detection of a dynamic topography signal in last interglacial sea-level records. *Science Advances* 3 (7), e1700457. URL <https://www.science.org/doi/abs/10.1126/sciadv.1700457>
- Ayachit, U., 2015. The ParaView Guide: A Parallel Visualization Application. Kitware, Inc., Clifton Park, NY, USA. URL <https://dl.acm.org/doi/abs/10.5555/2789330>
- Balay, S., Abhyankar, S., Adams, M. F., Benson, S., Brown, J., Brune, P., Buschelman, K., Constantinescu, E. M., Dalcin, L., Dener, A., Eijkhout, V., Faibussowitsch, J., Gropp, W. D., Hapla, V., Isaac, T., Jolivet, P., Karpeev, D., Kaushik, D., Knepley, M. G., Kong, F., Kruger, S., May, D. A., McInnes, L. C., Mills, R. T., Mitchell, L., Munson, T., Roman, J. E., Rupp, K., Sanan, P., Sarich, J., Smith, B. F., Zampini, S., Zhang, H., Zhang, H., Zhang, J., 2025. PETSc Web page. <https://petsc.org/>. URL <https://petsc.org/>
- Bastos, L., Bos, M., Fernandes, R. M., 2010. Deformation and tectonics: Contribution of gps measurements to plate tectonics – overview and recent developments. In: Xu, G. (Ed.), Sciences of Geodesy - I: Advances and Future Directions. Springer Berlin Heidelberg, Berlin, Heidelberg, pp. 155–184. URL https://doi.org/10.1007/978-3-642-11741-1_5

References

- Bodur, O. F., Rey, P. F., 2019. The impact of rheological uncertainty on dynamic topography predictions. *Solid Earth* 10 (6), 2167–2178. URL <https://se.copernicus.org/articles/10/2167/2019/>
- Bunge, H.-P., Hagelberg, C. R., Travis, B. J., 02 2003. Mantle circulation models with variational data assimilation: inferring past mantle flow and structure from plate motion histories and seismic tomography. *Geophysical Journal International* 152 (2), 280–301. URL <https://doi.org/10.1046/j.1365-246X.2003.01823.x>
- Calvelage, C. M., Wu, J., Colli, L., Lin, Y.-A., Zheng, Y., 2024. Linking deep-time subduction history to modern day expressions of dynamic topography. *Proceedings of the Royal Society A: Mathematical, Physical and Engineering Sciences* 480 (2301), 20240254. URL <https://royalsocietypublishing.org/doi/abs/10.1098/rspa.2024.0254>
- Carrassi, A., Bocquet, M., Bertino, L., Evensen, G., 2018. Data assimilation in the geosciences: An overview of methods, issues, and perspectives. *WIREs Climate Change* 9 (5), e535. URL <https://wires.onlinelibrary.wiley.com/doi/abs/10.1002/wcc.535>
- Cathles, L. M., 2015. Viscosity of the Earth's Mantle. Princeton university press.
- Chu, R., Schmandt, B., Helmberger, D. V., 2012. Juan de fuca subduction zone from a mixture of tomography and waveform modeling. *Journal of Geophysical Research: Solid Earth* 117, B03310, first published: 09 March 2012. URL <https://doi.org/10.1029/2012JB009146>
- Colli, L., Bunge, H.-P., Schuberth, B. S. A., 2015. On retrodictions of global mantle flow with assimilated surface velocities. *Geophysical Research Letters* 42 (20), 8341–8348. URL <https://doi.org/10.1002/2015GL066001>
- Colli, L., Ghelichkhan, S., Bunge, H.-P., 2016. On the ratio of dynamic topography and gravity anomalies in a dynamic earth. *Geophysical Research Letters* 43 (6), 2510–2516. URL <https://doi.org/10.1002/2016GL067929>
- Colli, L., Ghelichkhan, S., Bunge, H.-P., Oeser, J., 2018. Retrodictions of mid paleogene mantle flow and dynamic topography in the atlantic region from compressible high resolution adjoint mantle convection models: Sensitivity to deep mantle viscosity and tomographic input model. *Gondwana Research* 53, 252–272, rifting to Passive Margins. URL <https://www.sciencedirect.com/science/article/pii/S1342937X17302125>

- Coltice, N., Gérault, M., Ulvrová, M., 2017. A mantle convection perspective on global tectonics. *Earth-Science Reviews* 165, 120–150. URL <https://www.sciencedirect.com/science/article/pii/S0012825216304354>
- Conn, A. R., Gould, N. I., Toint, P. L., 2000. Trust region methods. SIAM.
- Conrad, C. P., Husson, L., 04 2009. Influence of dynamic topography on sea level and its rate of change. *Lithosphere* 1 (2), 110–120. URL <https://doi.org/10.1130/L32.1>
- Crawford, O., Al-Attar, D., Tromp, J., Mitrovica, J. X., Austermann, J., Lau, H. C. P., 05 2018. Quantifying the sensitivity of post-glacial sea level change to laterally varying viscosity. *Geophysical Journal International* 214 (2), 1324–1363. URL <https://doi.org/10.1093/gji/ggy184>
- Czarnota, K., Hoggard, M., White, N., Winterbourne, J., 2013. Spatial and temporal patterns of cenozoic dynamic topography around australia. *Geochemistry, Geophysics, Geosystems* 14 (3), 634–658.
- Czarnota, K., Roberts, G., White, N., Fishwick, S., 2014. Spatial and temporal patterns of australian dynamic topography from river profile modeling. *Journal of Geophysical Research: Solid Earth* 119 (2), 1384–1424.
- Davies, D., Davies, J., 2009. Thermally-driven mantle plumes reconcile multiple hot-spot observations. *Earth and Planetary Science Letters* 278 (1), 50–54. URL <https://www.sciencedirect.com/science/article/pii/S0012821X08007383>
- Davies, D., Ghelichkhan, S., Hoggard, M., Valentine, A., Richards, F., 2023. Observations and models of dynamic topography: Current status and future directions. In: Duarte, J. C. (Ed.), *Dynamics of Plate Tectonics and Mantle Convection*. Elsevier, pp. 223–269. URL <https://doi.org/10.1016/B978-0-323-85733-8.00017-2>
- Davies, D. R., Kramer, S. C., Ghelichkhan, S., Gibson, A., 2022. Towards automatic finite-element methods for geodynamics via firedrake. *Geoscientific Model Development* 15 (13), 5127–5166. URL <https://gmd.copernicus.org/articles/15/5127/2022/>
- Davies, D. R., Valentine, A. P., Kramer, S. C., Rawlinson, N., Hoggard, M. J., Eakin, C. M., Wilson, C. R., 2019. Earth's multi-scale topographic response to global mantle flow. *Nature Geoscience* 12 (10), 845–850. URL <https://doi.org/10.1038/s41561-019-0441-4>

References

- Davies, G. F., Richards, M. A., 1992. Mantle convection. *The Journal of Geology* 100 (2), 151–206. URL <https://doi.org/10.1086/629582>
- DiCaprio, L., Gurnis, M., Müller, R. D., 2009. Long-wavelength tilting of the australian continent since the late cretaceous. *Earth and Planetary Science Letters* 278 (3), 175–185. URL <https://www.sciencedirect.com/science/article/pii/S0012821X08007450>
- Dixon, L. C. W., Price, R. C., 1989. Truncated newton method for sparse unconstrained optimization using automatic differentiation. *Journal of Optimization Theory and Applications* 60 (2), 261–275. URL <https://doi.org/10.1007/BF00940007>
- Elman, H. C., Silvester, D. J., Wathen, A. J., 2014. Finite elements and fast iterative solvers: with applications in incompressible fluid dynamics. Oxford university press.
- Euen, G. T., Liu, S., Gassmöller, R., Heister, T., King, S. D., 2023. A comparison of 3-d spherical shell thermal convection results at low to moderate rayleigh number using aspect (version 2.2.0) and citcoms (version 3.3.1). *Geoscientific Model Development* 16 (11), 3221–3239. URL <https://gmd.copernicus.org/articles/16/3221/2023/>
- Farrell, P. E., Ham, D. A., Funke, S. W., Rognes, M. E., 2013. Automated derivation of the adjoint of high-level transient finite element programs. *SIAM Journal on Scientific Computing* 35 (4), C369–C393. URL <https://doi.org/10.1137/120873558>
- Fichtner, A., 2010. Full seismic waveform modelling and inversion. Springer Science & Business Media.
- Fichtner, A., Kennett, B. L. N., Tsai, V. C., Thurber, C. H., Rodgers, A. J., Tape, C., Rawlinson, N., Borcherdt, R. D., Lebedev, S., Priestley, K., Morency, C., Bozdağ, E., Tromp, J., Ritsema, J., Romanowicz, B., Liu, Q., Golos, E., Lin, F., 05 2024. Seismic tomography 2024. *Bulletin of the Seismological Society of America* 114 (3), 1185–1213. URL <https://doi.org/10.1785/0120230229>
- Flament, N., Gurnis, M., Müller, R. D., 04 2013. A review of observations and models of dynamic topography. *Lithosphere* 5 (2), 189–210. URL <https://doi.org/10.1130/L245>.

- Forte, A. M., Rowley, D. B., 2022. Earth's isostatic and dynamic topography—a critical perspective. *Geochemistry, Geophysics, Geosystems* 23 (9), e2021GC009740. URL <https://agupubs.onlinelibrary.wiley.com/doi/abs/10.1029/2021GC009740>
- Gallagher, K., Brown, R., 1997. The onshore record of passive margin evolution. *Journal of the Geological Society* 154 (3), 451–457. URL <https://www.lyellcollection.org/doi/abs/10.1144/gsjgs.154.3.0451>
- Gerya, T., 2019. Introduction to numerical geodynamic modelling. Cambridge University Press.
- Ghelichkhan, S., Bunge, H.-P., 2016. The compressible adjoint equations in geodynamics: derivation and numerical assessment. *GEM - International Journal on Geomathematics* 7 (1), 1–30. URL <https://doi.org/10.1007/s13137-016-0080-5>
- Ghelichkhan, S., Bunge, H.-P., Oeser, J., 03 2021. Global mantle flow retrodictions for the early cenozoic using an adjoint method: evolving dynamic topographies, deep mantle structures, flow trajectories and sublithospheric stresses. *Geophysical Journal International* 226 (2), 1432–1460. URL <https://doi.org/10.1093/gji/ggab108>
- Ghelichkhan, S., Gibson, A., Davies, D. R., Kramer, S. C., Ham, D. A., 2024. Automatic adjoint-based inversion schemes for geodynamics: reconstructing the evolution of earth's mantle in space and time. *Geoscientific Model Development* 17 (13), 5057–5086. URL <https://gmd.copernicus.org/articles/17/5057/2024/>
- Gibson, A., Davies, R., Kramer, S., Ghelichkhan, S., Turner, R., Duvernay, T., Scott, W., Jun. 2024. G-ADOPT. URL <https://github.com/g-adopt/g-adopt>
- Gibson, T. H., McRae, A. T., Cotter, C. J., Mitchell, L., Ham, D. A., 2019. Compatible Finite Element Methods for Geophysical Flows: Automation and Implementation Using Firedrake. Springer Nature.
- Giering, R., Kaminski, T., Dec. 1998. Recipes for adjoint code construction. *ACM Trans. Math. Softw.* 24 (4), 437–474. URL <https://doi.org/10.1145/293686.293695>
- Giles, M. B., Pierce, N. A., 2000. An introduction to the adjoint approach to design. *Flow, Turbulence and Combustion* 65 (3), 393–415. URL <https://doi.org/10.1023/A:1011430410075>

References

- Guerri, M., Cammarano, F., Tackley, P., 2016. Modelling earth's surface topography: Decomposition of the static and dynamic components. *Physics of the Earth and Planetary Interiors* 261, 172–186. URL <https://www.sciencedirect.com/science/article/pii/S0031920116301364>
- Gunzburger, M., 2000. Adjoint equation-based methods for control problems in incompressible, viscous flows. *Flow, Turbulence and Combustion* 65 (3), 249–272. URL <https://doi.org/10.1023/A:1011455900396>
- Gunzburger, M. D., 2002. Perspectives in Flow Control and Optimization. Society for Industrial and Applied Mathematics. URL <https://pubs.siam.org/doi/abs/10.1137/1.9780898718720>
- Gurnis, M., 1993. Phanerozoic marine inundation of continents driven by dynamic topography above subducting slabs. *Nature* 364 (6438), 589–593. URL <https://doi.org/10.1038/364589a0>
- Gurnis, M., Mitrovica, J. X., Ritsema, J., van Heijst, H.-J., 2000. Constraining mantle density structure using geological evidence of surface uplift rates: The case of the african superplume. *Geochemistry, Geophysics, Geosystems* 1 (7).
- Hager, B. H., Richards, M. A., 1989. Long-wavelength variations in earth's geoid: physical models and dynamical implications. *Philosophical Transactions of the Royal Society of London. Series A, Mathematical and Physical Sciences* 328 (1599), 309–327. URL <https://doi.org/10.1098/rsta.1989.0038>
- Haines, A. J., Dimitrova, L. L., Wallace, L. M., Williams, C. A., 2015. Enhanced surface imaging of crustal deformation: Obtaining tectonic force fields using GPS data. Springer.
- Ham, D. A., Kelly, P. H. J., Mitchell, L., Cotter, C. J., Kirby, R. C., Sagiyama, K., Bouziani, N., Vorderwuelbecke, S., Gregory, T. J., Betteridge, J., Shapero, D. R., Nixon-Hill, R. W., Ward, C. J., Farrell, P. E., Brubeck, P. D., Marsden, I., Gibson, T. H., Homolya, M., Sun, T., McRae, A. T. T., Luporini, F., Gregory, A., Lange, M., Funke, S. W., Rathgeber, F., Bercea, G.-T., Markall, G. R., 5 2023. Firedrake User Manual. Imperial College London and University of Oxford and Baylor University and University of Washington, first edition Edition.

- Hansen, P. C., 1992. Analysis of discrete ill-posed problems by means of the l-curve. *SIAM Review* 34 (4), 561–580. URL <https://doi.org/10.1137/1034115>
- Hinze, M., Pinna, R., Ulbrich, M., Ulbrich, S., 2008. Optimization with PDE constraints. Vol. 23. Springer Science & Business Media.
- Hoggard, M., Austermann, J., Randel, C., Stephenson, S., 2021. Observational Estimates of Dynamic Topography Through Space and Time. American Geophysical Union (AGU), Ch. 15, pp. 371–411. URL <https://agupubs.onlinelibrary.wiley.com/doi/abs/10.1002/9781119528609.ch15>
- Hoggard, M. J., White, N., Al-Attar, D., 2016. Global dynamic topography observations reveal limited influence of large-scale mantle flow. *Nature Geoscience* 9 (6), 456–463. URL <https://doi.org/10.1038/ngeo2709>
- Hoggard, M. J., Winterbourne, J., Czarnota, K., White, N., 2017. Oceanic residual depth measurements, the plate cooling model, and global dynamic topography. *Journal of Geophysical Research: Solid Earth* 122 (3), 2328–2372. URL <https://agupubs.onlinelibrary.wiley.com/doi/abs/10.1002/2016JB013457>
- Horbach, A., Bunge, H.-P., Oeser, J., 2014. The adjoint method in geodynamics: derivation from a general operator formulation and application to the initial condition problem in a high resolution mantle circulation model. *GEM - International Journal on Geomathematics* 5 (2), 163–194. URL <https://doi.org/10.1007/s13137-014-0061-5>
- Husson, L., Conrad, C. P., 2006. Tectonic velocities, dynamic topography, and relative sea level. *Geophysical Research Letters* 33 (18). URL <https://agupubs.onlinelibrary.wiley.com/doi/abs/10.1029/2006GL026834>
- Ismail-Zadeh, A., Schubert, G., Tsepelev, I., Korotkii, A., 2004. Inverse problem of thermal convection: numerical approach and application to mantle plume restoration. *Physics of the Earth and Planetary Interiors* 145 (1), 99–114. URL <https://www.sciencedirect.com/science/article/pii/S0031920104001384>
- Jarvis, G. T., Peltier, W. R., 02 1982. Mantle convection as a boundary layer phenomenon. *Geophysical Journal International* 68 (2), 389–427. URL <https://doi.org/10.1111/j.1365-246X.1982.tb04907.x>

References

- Kaban, M. K., Schwintzer, P., Artemieva, I. M., Mooney, W. D., 2003. Density of the continental roots: compositional and thermal contributions. *Earth and Planetary Science Letters* 209 (1), 53–69. URL <https://www.sciencedirect.com/science/article/pii/S0012821X03000724>
- Kaufmann, G., Lambeck, K., 2002. Glacial isostatic adjustment and the radial viscosity profile from inverse modeling. *Journal of Geophysical Research: Solid Earth* 107 (B11), ETG 5–1–ETG 5–11. URL <https://doi.org/10.1029/2001JB000941>
- Kirby, R. C., Mitchell, L., Dec. 2019. Code generation for generally mapped finite elements. *ACM Trans. Math. Softw.* 45 (4). URL <https://doi.org/10.1145/3361745>
- Kramer, S. C., Wilson, C. R., Davies, D. R., 2012. An implicit free surface algorithm for geodynamical simulations. *Physics of the Earth and Planetary Interiors* 194–195, 25–37. URL <https://doi.org/10.1016/j.pepi.2012.01.001>
- Lau, H. C. P., Austermann, J., Mitrovica, J. X., Crawford, O., Al-Attar, D., Latychev, K., 2018. Inferences of mantle viscosity based on ice age data sets: The bias in radial viscosity profiles due to the neglect of laterally heterogeneous viscosity structure. *Journal of Geophysical Research: Solid Earth* 123 (9), 7237–7252. URL <https://agupubs.onlinelibrary.wiley.com/doi/abs/10.1029/2018JB015740>
- Li, D., Gurnis, M., Stadler, G., 01 2017. Towards adjoint-based inversion of time-dependent mantle convection with nonlinear viscosity. *Geophysical Journal International* 209 (1), 86–105. URL <https://doi.org/10.1093/gji/ggw493>
- Lieb, V., Schmidt, M., Dettmering, D., Börger, K., 2016. Combination of various observation techniques for regional modeling of the gravity field. *Journal of Geophysical Research: Solid Earth* 121 (5), 3825–3845. URL <https://agupubs.onlinelibrary.wiley.com/doi/abs/10.1002/2015JB012586>
- Lin, C.-J., Moré, J. J., 1999. Newton’s method for large bound-constrained optimization problems. *SIAM Journal on Optimization* 9 (4), 1100–1127. URL <https://doi.org/10.1137/S1052623498345075>
- Lithgow-Bertelloni, C., Silver, P. G., 1998. Dynamic topography, plate driving forces and the african superswell. *Nature* 395 (6699), 269–272. URL <https://doi.org/10.1038/26212>

- Liu, L., Gurnis, M., 2008. Simultaneous inversion of mantle properties and initial conditions using an adjoint of mantle convection. *Journal of Geophysical Research: Solid Earth* 113 (B8). URL <https://agupubs.onlinelibrary.wiley.com/doi/abs/10.1029/2008JB005594>
- Liu, L., Spasojević, S., Gurnis, M., 2008. Reconstructing farallon plate subduction beneath north america back to the late cretaceous. *Science* 322 (5903), 934–938. URL <https://www.science.org/doi/abs/10.1126/science.1162921>
- Liu, Q., Gu, Y., 2012. Seismic imaging: From classical to adjoint tomography. *Tectonophysics* 566-567, 31–66. URL <https://www.sciencedirect.com/science/article/pii/S004019511200409X>
- Mao, W., Zhong, S., 2021. Constraints on mantle viscosity from intermediate-wavelength geoid anomalies in mantle convection models with plate motion history. *Journal of Geophysical Research: Solid Earth* 126 (4), e2020JB021561, e2020JB021561 2020JB021561. URL <https://agupubs.onlinelibrary.wiley.com/doi/abs/10.1029/2020JB021561>
- Marchuk, G. I., 1995. Inverse Problems and Adjoint Equations. Springer Netherlands, Dordrecht, pp. 163–205. URL https://doi.org/10.1007/978-94-017-0621-6_5
- Martinec, Z., Sasgen, I., Velímský, J., 2014. The forward sensitivity and adjoint-state methods of glacial isostatic adjustment. *Geophysical Journal International* 200 (1), 77–105. URL <https://doi.org/10.1093/gji/ggu378>
- May, D., Schellart, W., Moresi, L., 2013. Overview of adaptive finite element analysis in computational geodynamics. *Journal of Geodynamics* 70, 1–20. URL <https://www.sciencedirect.com/science/article/pii/S0264370713000616>
- May, D. A., Moresi, L., 2008. Preconditioned iterative methods for stokes flow problems arising in computational geodynamics. *Physics of the Earth and Planetary Interiors* 171 (1), 33–47, recent Advances in Computational Geodynamics: Theory, Numerics and Applications. URL <https://www.sciencedirect.com/science/article/pii/S003192010800191X>
- McKenzie, D., Roberts, J., Weiss, N., 1973. Numerical models of convection in the earth's mantle. *Tectonophysics* 19 (2), 89–103, mechanisms of plate tectonics. URL <https://www.sciencedirect.com/science/article/pii/0040195173900346>

References

- Mitrovica, J., Beaumont, C., Jarvis, G., 1989. Tilting of continental interiors by the dynamical effects of subduction. *Tectonics* 8 (5), 1079–1094.
- Mitrovica, J., Forte, A., 2004. A new inference of mantle viscosity based upon joint inversion of convection and glacial isostatic adjustment data. *Earth and Planetary Science Letters* 225 (1), 177–189. URL <https://www.sciencedirect.com/science/article/pii/S0012821X04003747>
- Mitrovica, J., Pysklywec, R., Beaumont, C., Rutty, A., 1996. The devonian to permian sedimentation of the russian platform: An example of subduction-controlled long-wavelength tilting of continents. *Journal of Geodynamics* 22 (1), 79–96. URL <https://www.sciencedirect.com/science/article/pii/0264370796000087>
- Mitrovica, J. X., Austermann, J., Coulson, S., Creveling, J. R., Hoggard, M. J., Jarvis, G. T., Richards, F. D., 2020. Dynamic topography and ice age paleoclimate. *Annual Review of Earth and Planetary Sciences* 48, 585–621. URL <https://www.annualreviews.org/content/journals/10.1146/annurev-earth-082517-010225>
- Mitusch, S. K., Funke, S. W., Dokken, J. S., 2019. dolfin-adjoint 2018.1: automated adjoints for fenics and firedrake. *Journal of Open Source Software* 4 (38), 1292. URL <https://doi.org/10.21105/joss.01292>
- Molnar, P., England, P. C., Jones, C. H., 2015. Mantle dynamics, isostasy, and the support of high terrain. *Journal of Geophysical Research: Solid Earth* 120 (3), 1932–1957. URL <https://agupubs.onlinelibrary.wiley.com/doi/abs/10.1002/2014JB011724>
- Monnereau, M., Quéré, S., 2001. Spherical shell models of mantle convection with tectonic plates. *Earth and Planetary Science Letters* 184 (3), 575–587. URL <https://www.sciencedirect.com/science/article/pii/S0012821X00003344>
- Moucha, R., Forte, A. M., Mitrovica, J. X., Rowley, D. B., Quéré, S., Simmons, N. A., Grand, S. P., 2008. Dynamic topography and long-term sea-level variations: There is no such thing as a stable continental platform. *Earth and Planetary Science Letters* 271 (1), 101–108. URL <https://www.sciencedirect.com/science/article/pii/S0012821X08002227>
- Moucha, R., Forte, A. M., Rowley, D. B., Mitrovica, J. X., Simmons, N. A., Grand, S. P., 2009.

- Deep mantle forces and the uplift of the colorado plateau. *Geophysical Research Letters* 36 (19).
- Müller, R., Hassan, R., Gurnis, M., Flament, N., Williams, S., 2018. Dynamic topography of passive continental margins and their hinterlands since the cretaceous. *Gondwana Research* 53, 225–251, rifting to Passive Margins. URL <https://www.sciencedirect.com/science/article/pii/S1342937X17302162>
- Nocedal, J., Wright, S. J., 1999. Numerical optimization. Springer.
- Nocedal, J., Wright, S. J., 2006. Conjugate gradient methods. *Numerical optimization*, 101–134.
- Osei Tutu, A., Steinberger, B., Sobolev, S. V., Rogozhina, I., Popov, A. A., 2018. Effects of upper mantle heterogeneities on the lithospheric stress field and dynamic topography. *Solid Earth* 9 (3), 649–668. URL <https://se.copernicus.org/articles/9/649/2018/>
- Peltier, W. R., Jiang, X., 1997. Mantle viscosity, glacial isostatic adjustment and the eustatic level of the sea. *Surveys in Geophysics* 18 (2), 239–277. URL <https://doi.org/10.1023/A:1006592111018>
- Pirajno, F., 2004. Hotspots and mantle plumes: global intraplate tectonics, magmatism and ore deposits. *Mineralogy and Petrology* 82 (3), 183–216. URL <https://doi.org/10.1007/s00710-004-0046-4>
- Plessix, R.-E., 2006. A review of the adjoint-state method for computing the gradient of a functional with geophysical applications. *Geophysical Journal International* 167 (2), 495–503. URL <https://doi.org/10.1111/j.1365-246X.2006.02978.x>
- Pysklywec, R. N., Mitrovica, J. X., 1999. The role of subduction-induced subsidence in the evolution of the karoo basin. *The Journal of Geology* 107 (2), 155–164.
- Rathgeber, F., Ham, D. A., Mitchell, L., Lange, M., Luporini, F., Mcrae, A. T. T., Bercea, G.-T., Markall, G. R., Kelly, P. H. J., Dec. 2016. Firedrake: Automating the finite element method by composing abstractions. *ACM Trans. Math. Softw.* 43 (3). URL <https://doi.org/10.1145/2998441>

References

- Rawlinson, N., Fichtner, A., Sambridge, M., Young, M. K., 2014. Chapter one - seismic tomography and the assessment of uncertainty. In: DMOWSKA, R. (Ed.), *Advances in Geophysics*. Vol. 55. Elsevier, pp. 1–76. URL <https://www.sciencedirect.com/science/article/pii/S0065268714000028>
- Reuber, G. S., Holbach, L., Popov, A. A., Hanke, M., Kaus, B. J. P., 07 2020. Inferring rheology and geometry of subsurface structures by adjoint-based inversion of principal stress directions. *Geophysical Journal International* 223 (2), 851–861. URL <https://doi.org/10.1093/gji/ggaa344>
- Reuber, G. S., Popov, A. A., Kaus, B. J., 2018. Deriving scaling laws in geodynamics using adjoint gradients. *Tectonophysics* 746, 352–363, understanding geological processes through modelling - A Memorial Volume honouring Evgenii Burov. URL <https://www.sciencedirect.com/science/article/pii/S0040195117303001>
- Ricard, Y., 2007. Physics of mantle convection. *Treatise on geophysics* 7, 31–87.
- Ricard, Y., Richards, M., Lithgow-Bertelloni, C., Le Stunff, Y., 1993. A geodynamic model of mantle density heterogeneity. *Journal of Geophysical Research: Solid Earth* 98 (B12), 21895–21909. URL <https://agupubs.onlinelibrary.wiley.com/doi/abs/10.1029/93JB02216>
- Robb, L., 2020. *Introduction to ore-forming processes*. John Wiley & Sons.
- Romanowicz, B., 2008. Using seismic waves to image earth's internal structure. *Nature* 451 (7176), 266–268. URL <https://doi.org/10.1038/nature06583>
- Rovere, A., Raymo, M., Mitrovica, J., Hearty, P., O'Leary, M., Inglis, J., 2014. The mid-pliocene sea-level conundrum: Glacial isostasy, eustasy and dynamic topography. *Earth and Planetary Science Letters* 387, 27–33. URL <https://www.sciencedirect.com/science/article/pii/S0012821X13006006>
- Schwertes, T., Ham, D. A., Funke, S. W., Piggott, M. D., 2017. Mesh dependence in pde-constrained optimisation. In: *Mesh Dependence in PDE-Constrained Optimisation: An Application in Tidal Turbine Array Layouts*. Springer International Publishing, Cham, pp. 53–78. URL https://doi.org/10.1007/978-3-319-59483-5_2

- Shephard, G. E., Müller, R. D., Liu, L., Gurnis, M., 2010. Miocene drainage reversal of the amazon river driven by plate–mantle interaction. *Nature Geoscience* 3 (12), 870–875. URL <https://doi.org/10.1038/ngeo1017>
- Spasojevic, S., Liu, L., Gurnis, M., 2009. Adjoint models of mantle convection with seismic, plate motion, and stratigraphic constraints: North america since the late cretaceous. *Geochemistry, Geophysics, Geosystems* 10 (5). URL <https://agupubs.onlinelibrary.wiley.com/doi/abs/10.1029/2008GC002345>
- Stadler, G., Gurnis, M., Burstedde, C., Wilcox, L. C., Alisic, L., Ghattas, O., 2010. The dynamics of plate tectonics and mantle flow: From local to global scales. *Science* 329 (5995), 1033–1038. URL <https://www.science.org/doi/abs/10.1126/science.1191223>
- Steffen, H., Kaufmann, G., 11 2005. Glacial isostatic adjustment of scandinavia and north-western europe and the radial viscosity structure of the earth’s mantle. *Geophysical Journal International* 163 (2), 801–812. URL <https://doi.org/10.1111/j.1365-246X.2005.02740.x>
- Steinberger, B., Werner, S. C., Torsvik, T. H., 2010. Deep versus shallow origin of gravity anomalies, topography and volcanism on earth, venus and mars. *Icarus* 207 (2), 564–577. URL <https://www.sciencedirect.com/science/article/pii/S0019103509005168>
- Sullivan, C. B., Kaszynski, A., may 2019. PyVista: 3d plotting and mesh analysis through a streamlined interface for the visualization toolkit (VTK). *Journal of Open Source Software* 4 (37), 1450. URL <https://doi.org/10.21105/joss.01450>
- Thieulot, C., Bangerth, W., 2022. On the choice of finite element for applications in geodynamics. *Solid Earth* 13 (1), 229–249. URL <https://se.copernicus.org/articles/13/229/2022/>
- Tijskens, E., Roose, D., Ramon, H., Baerdemaeker, J. D., 2002. Automatic differentiation for solving nonlinear partial differential equations: An efficient operator overloading approach. *Numerical Algorithms* 30 (3), 259–301. URL <https://doi.org/10.1023/A:1020103610525>

References

- Tikhonov, A. N., 1963. Solution of incorrectly formulated problems and the regularization method. Sov Dok 4, 1035–1038. URL <https://cir.nii.ac.jp/crid/1572824499302346368>
- Tosi, N., Stein, C., Noack, L., Hüttig, C., Maierová, P., Samuel, H., Davies, D. R., Wilson, C. R., Kramer, S. C., Thieulot, C., Glerum, A., Fraters, M., Spakman, W., Rozel, A., Tackley, P. J., 2015. A community benchmark for viscoplastic thermal convection in a 2-d square box. *Geochemistry, Geophysics, Geosystems* 16 (7), 2175–2196. URL <https://doi.org/10.1002/2015GC005807>
- Trilinos Team, 2024. Rapid optimization library (rol): A package for large-scale optimization. <https://docs.trilinos.org/dev/packages/rol/doc/html/index.html>, accessed: 2024-04-24.
- Turcotte, D. L., Schubert, G., 2002. *Geodynamics*. Cambridge university press.
- Valentine, A. P., Davies, D. R., 2020. Global models from sparse data: A robust estimate of earth’s residual topography spectrum. *Geochemistry, Geophysics, Geosystems* 21 (8), e2020GC009240.
- Worthen, J., Stadler, G., Petra, N., Gurnis, M., Ghattas, O., 2014. Towards adjoint-based inversion for rheological parameters in nonlinear viscous mantle flow. *Physics of the Earth and Planetary Interiors* 234, 23–34. URL <https://www.sciencedirect.com/science/article/pii/S0031920114001514>
- Yang, T., Gurnis, M., 09 2016. Dynamic topography, gravity and the role of lateral viscosity variations from inversion of global mantle flow. *Geophysical Journal International* 207 (2), 1186–1202. URL <https://doi.org/10.1093/gji/ggw335>
- Zhang, N., Zhong, S., Flowers, R. M., 2012. Predicting and testing continental vertical motion histories since the paleozoic. *Earth and Planetary Science Letters* 317-318, 426–435. URL <https://www.sciencedirect.com/science/article/pii/S0012821X1100639X>

Similarity Report



Page 1 of 118 - Cover Page

Submission ID trn:oid::1:3244809347

Prahlada Mittal

CONSTRAINING MANTLE PROPERTIES BY INVERTING FOR OBSERVATIONS OF DYNAMIC TOPOGRAPHY

Dissertation

Papers

Indian Institute of Technology, Roorkee

Document Details

Submission ID

trn:oid::1:3244809347

111 Pages

Submission Date

May 9, 2025, 6:50 PM GMT+5:30

27,807 Words

Download Date

May 9, 2025, 6:54 PM GMT+5:30

159,574 Characters

File Name

MTech_thesis_Prahlad-check.pdf

File Size

17.9 MB



Page 1 of 118 - Cover Page

Submission ID trn:oid::1:3244809347

8% Overall Similarity

The combined total of all matches, including overlapping sources, for each database.

Filtered from the Report

- › Bibliography
- › Quoted Text

Match Groups

- 169** Not Cited or Quoted 6%
Matches with neither in-text citation nor quotation marks
- 48** Missing Quotations 2%
Matches that are still very similar to source material
- 0** Missing Citation 0%
Matches that have quotation marks, but no in-text citation
- 0** Cited and Quoted 0%
Matches with in-text citation present, but no quotation marks

Top Sources

- 5% Internet sources
- 6% Publications
- 0% Submitted works (Student Papers)

Integrity Flags

0 Integrity Flags for Review

No suspicious text manipulations found.

Our system's algorithms look deeply at a document for any inconsistencies that would set it apart from a normal submission. If we notice something strange, we flag it for you to review.

A Flag is not necessarily an indicator of a problem. However, we'd recommend you focus your attention there for further review.

Prof. Pitambar Pati
Supervisor

Prahilada Varada Mittal